Component Design For InGaAsP-on-insulator Integrated Photonics

Garen Simpson

Thesis submitted to the University of Ottawa in partial fulfillment of the requirements for the degree of Master of Science, Physics

Department of Physics
Faculty of Science
University of Ottawa

Supervisor: Dr. Ksenia Dolgaleva

"It makes such a difference, to have someone who believes in you."

— *Winnie-the-Pooh*

Abstract

The growing demand for high-bandwidth data transmission, expanding communication networks, and capable sensing technologies is driven by the increasing number of internet-connected devices and the scaling of data-intensive tasks, such as artificial intelligence and high-performance computing. This has highlighted the need for technologies capable of efficient and high-speed optical signal processing. To address this need, photonic integration offers advantages over electronic technologies by more efficient power consumption, higher data bandwidth, and compact form factors for data and communication systems.

Among photonic integration platforms, group III-V semiconductors offer unique advantages by integrating light generation, optical modulation, detection, and low-loss signal routing on a single material platform. In this thesis, work carried out in collaboration with Optiwave Systems Inc. and the National Research Council of Canada (NRC) is presented. This work focuses on the development of a novel material platform, based on a III-V semiconductor, Indium Gallium Arsenide Phosphide (InGaAsP)-on-insulator, chosen for its multi-functionality as a telecommunication range light source, fast electro-optic modulation, and photo-detection, not seen in other platforms such as silicon or lithium niobate. Here, integrated components developed for the telecommunication O and C bands are incorporated into a library, which can later be used in a process design kit.

The component library presented includes embedded oxide strip waveguides, 90° circular waveguide bends, linear waveguide tapers, waveguide splitters for near-ideal 50/50 power splitting, and compact waveguide X-crossings. In addition, a subwavelength grating waveguide and broadband subwavelength grating edge coupler for efficient fibre-to-chip coupling are presented. Finally, second-harmonic generation waveguides are designed and analytically evaluated for the conversion of infrared wavelengths of 3.1 μm and 2.62 μm to telecommunication wavelengths of 1.55 μm and 1.31 μm, respectively.

This work provides an essential toolkit for creating application-specific photonic integrated circuits not previously seen for the InGaAsP platform, as well as a streamlined design-to-fabrication pathway compatible with Canadian fabrication infrastructure such as the Canadian Photonics Fabrication Centre (CPFC). The results presented in this thesis will support the development of scalable photonic devices for optical communications, all-optical signal processing, and sensing applications, contributing toward Canada's semiconductor and photonics ecosystem.

Acknowledgements

For the opportunity to contribute to this evolving research in the nonlinear photonics group, I would like to thank my supervisor, Dr. Ksenia Dolgaleva, for her steady support and guidance in this project throughout my time at the University of Ottawa. I have enjoyed working on such an amazing project that has provided me with not only creative freedom in designing photonic components but also the opportunity to engage in a sense of scientific curiosity that motivates me to explore new ideas. I would also like to thank our collaborators at Optiwave Systems Inc. and the National Research Council of Canada (NRC). At Optiwave Systems Inc., Cem Bonfil and Dr. Scott Newman, for their assistance and guidance in the design and simulation of photonic components using the Optimode and OptiFDTD software, and at NRC, Dr. Pavel Cheben and Dr. Jens Schmid, for their feedback and guidance on the design of subwavelength components.

In our nonlinear photonics group, I would like to thank Ozan Oner, Dr. Lais Fujii Dos Santos, and Dr. Gabriel Flizikowski for their help with learning the tools used in the design and simulation of components, including GDSFactory, Lumerical, and KLayout. When I first joined the nonlinear photonics group, Ozan and Gabriel were some of the first to welcome me to the group and make me feel invited. I would also like to acknowledge and thank the many friends and colleagues I have made during my time at the University of Ottawa, over lunchtime discussions and as part of student groups such as the SPIE-Optica student chapter and the Energy Futures Forum.

I am grateful to my friend Bennett for his meaningful support over the past eight years, ever since starting university. I would like to thank him especially for his supportive presence as I moved to Ottawa, and for helping me realize the value of keeping a good attitude through both academic and personal challenges. I would also like to acknowledge Dr. Billau for their meaningful part in helping me realize the value of honesty and patience in working through challenges during my time in Ottawa. Lastly, I would like to thank my family, my parents, and my two older brothers for their continued support of my goals as I pursue my studies. This journey would not have been possible without them.

Contents

List of Figures

List of Tables

1

Chapter 1: Introduction

Integrated photonics is an advancing field that uses the properties of photons for information transmission, processing, communication, and optical sensing in compact integrated circuits. In recent years, advances in machine learning and artificial intelligence have further highlighted the growing demand for integrated photonics, to accommodate increasing data traffic as well as efficiently scaling data centres to meet the growing demands of artificial intelligence (AI) from applications such as Open AI's ChatGPT, Anthropic's Claude, and Google Gemini [1–3]. This comes from reports that the demand for data centres worldwide between 2023 and 2030 could rise by 19-22 percent annually and reach an energy demand of 171-219 gigawatts (GW), growing from a current demand of approximately 60 GW [4]. This demand for data centres is dependent on the growing number of data-centred workloads, with a significant percentage being related to AI [4]. Innovations from integrated photonics have the opportunity to improve power efficiency to meet this growing demand, already seen by technologies such as co-packaged optics from Nvidia. Their technology supplies optical network switches to route large amounts of data between computers in data centres at high speeds, reducing the number of electrical links between systems and thus the power consumption needed by data centres [5]. The innovations that allow integrated photonics to be well-suited for applications in high-bandwidth data transfer stem from advances in optical communications and integrated electrical circuits.

The recent technologies for high-bandwidth data transfer, such as co-packaged optics, demonstrate the potential of integrated photonics, analogous to the historical evolution of integrated electrical circuits, which advanced computation and telecommunications through dense electrical circuits. The beginnings of integrated electrical circuits trace back

to the core innovations of William B. Shockley, John Bardeen, and Walter H. Brattain, the 1956 Nobel laureates for the invention of the transistor, as well as Jack Kilby and Robert Noyce, the inventors of the integrated circuit [6]. Soon after, the development of integrated photonic technologies began from the developments in integrated optics in 1969 by Stewart E. Miller [7].

In the decades following, advances in integrated optics and III-V semiconductors for lasers, amplifiers, modulators, and detectors greatly enhanced long-distance optical communications and data transfer [8–13]. One of the key technologies that advanced optical communications in both passive optical networks and active signal modulation is multiplexing and demultiplexing systems, where optical signals are spaced into different channels based on their frequency, polarization, or mode category, encoding optical signals used in data transmission and greatly improving transmission capacity [14, 15]. In commercial devices, dense wavelength division multiplexing (DWDM) is common, where up to 80 channels with 50 GHz spacing are enabled by integrated optical components combined with optical fibre communications, operating with the same principles for integrated optics demonstrated by Miller in 1969 [7, 16]. These systems, when combined with sophisticated non-linear optical processes, can improve data transmission in optical fibre networks, allowing for incredible improvements in internet speed as demonstrated by A. A. Jørgensen et al. in 2022 [17].

The advantages of integrated photonics become especially apparent for all-optical signal processing, where signal routing, wavelength conversion, logic operations, and more are performed in the optical domain [18]. For integrated photonic circuits, there is less

need for optical to electrical to optical (OEO) signal conversion. In addition, the benefit of photonic integrated circuits is that photons do not interact with each other, allowing for signals to propagate in parallel without interfering with each other, enabling high data transmission rates. This property of photonic circuits has been explored for applications using optical interconnects, where information is passed to different links between systems using light [19]. As well as for data and computational tasks, optical transceivers improve efficiency for processors where data is stored and sent out through electrical wires before being coupled to optical transceivers. Nvidia's co-packaged optics makes use of this advantage by integrating the optical fibres directly to the processor, creating a single package, with a main drawback being that lasers cannot be incorporated in the same package [5]. When combined with complementary metal oxide semiconductor (CMOS) fabrication processes, photonic chips enable extremely compact footprints with high-bandwidth capability [20, 21]. The developments in these areas have largely been with silicon; however, III-V integrated photonics is especially favourable in this area, owing to the incorporation of semiconductor lasers, electro-optic signal modulation, and nonlinear optical performance applicable to wavelength conversion [22–25].

A wide range of material platforms for integrated photonics have been explored, including silicon [26], silicon nitride [27], and lithium niobate [28, 29]. Silicon photonics has seen an immense number of developments for data-communication and sensing applications due to the ease of fabrication and CMOS compatibility, with many foundries offering silicon wafers up to 300 mm [30, 31]. However, silicon is a material that is not capable of second-order nonlinear processes, offers slower and less efficient electro-optic switching

than other semiconductors, and suffers from two-photon absorption, making free-carrier absorption a significant concern for higher optical powers. Silicon nitride is also a popular choice for nonlinear photonic applications, providing high Q-factor ring resonators capable of frequency comb generation [32]; however, it cannot perform second-order nonlinear optical interactions, and has a lower index contrast with silica and therefore has larger device footprints. Lithium niobate is also used for integrated photonics due to its high electro-optic coefficient, high-performance optical modulation, and compatible mode sizes for coupling to optical fibres. Lithium niobate also exhibits high values for second-order nonlinear susceptibility [29]. However, it cannot easily be combined with lasers on the same chip, is less flexible for tuning material refractive index and wavelength ranges, and has natural birefringence, making polarization-insensitive devices difficult to design. Among these materials, III-V semiconductors provide the unique advantage of incorporating lasers, high-performance modulators, amplifiers, and detectors grown from the same material. In addition, they are capable of a wide range of second and third-order nonlinear processes for wavelength conversion and signal modulation. Finally, their material compositions can be adjusted to allow for wider wavelength operation regimes. In particular, InGaAsP represents the best III-V semiconductor for creating lasers at telecom wavelengths, passive waveguides, signal modulation, and efficient detectors, all grown from Indium Phosphide (InP). In this thesis, we present passive integrated components designs for a high-index-contrast InGaAsP-on-insulator material platform. We also further develop passive InGaAsP-on-insulator nonlinear devices for second-harmonic generation, converting near-infrared to telecom wavelength. These designs constitute the first demonstration

of linear and nonlinear photonic components on the InGaAsP-on-insulator platform.

The integration of III-V semiconductors into photonic integrated circuits has found many applications as active devices in telecommunications [33] and sensing [34–36]. Semiconductors such as InGaAsP/InP, InGaAs/GaAs, and AlGaAs/GaAs have been used as light sources at telecom wavelengths for high-performance transceivers (transmitter and receiver), essential components in many data centres [5, 12, 37–39]. However, the prevalence of high-index contrast III-V materials for integrated photonics has been largely limited to including III-V semiconductor lasers bonded to silicon-on-insulator materials. Other applications of III-V on insulator platforms have been for photonic crystal laser cavities on an SiO_2/Si materials [40], photodetectors incorporated into Si/SiO_2 materials [41], and bonding techniques for InP-based III-Vs [42]. There is currently a research gap for application-specific photonic circuits using high-contrast III-V materials. This limitation prevents integration of a simplified materials scheme for a broader range of photonic circuits, with lasers, modulators, amplifiers, and detectors built on the same material platform. This is often due to the complex fabrication process for InGaAsP/SiO_2 materials, where few foundries offer design kits for III-V semiconductors.

The growing need for capable photonic integrated circuits with III-Vs has applications for sectors that rely on high precision sensing and efficient information processing, such as telecommunications, healthcare, and automotive sectors. Increased bandwidth and efficiency for information processing are useful for autonomous systems, data centres, and medical diagnostics [20, 43–45]. Integrated photonic transceivers are a prime example of a photonic technology that uses III-V semiconductors to combine light sources, multiplex-

ing operations, and high-speed detection for increased efficiency of data transmission [46]. Lidar (light detection and ranging) systems use III-V materials for coherent light sources incorporated into devices using gratings for beam steering and detection in different environments [45]. The different applications of III-V materials in these areas demonstrate the increasing demand for high-speed, efficient devices across a range of applications.

III–V integrated photonics offers unique advantages of active device integration, including lasers, amplifiers, modulators, and detectors on a single chip. However, there is currently no high-index contrast III-V photonic platform developed for Canadian fabrication infrastructure, and there is not currently a component library made for passive devices using Indium Gallium Arsenide Phosphide (InGaAsP) in integrated photonics. This thesis contributes to addressing these gaps by developing streamlined designs for a component library using InGaAsP-on-Insulator materials, made with a 220 nm thick guiding layer of InGaAsP, surrounded by silicon dioxide (SiO_2). Furthermore, this thesis also addresses the need for efficient nonlinear optical processes by providing waveguide geometries, phase-matched for second harmonic generation from infrared to telecom wavelength conversion. The work discussed in this thesis is intended for telecom-band compatible photonic integrated components, providing strong optical confinement, dispersion control, and access to second-order nonlinear phenomena. It should also be noted that the work presented throughout this thesis was developed in collaboration with Optiwave Systems Inc. for conventional photonic components in Chapter 2, as well as with Dr. Pavel Cheben and Dr. Jens Schmid at the National Research Council Canada (NRC) for subwavelength photonic components in Chapter 3.

1.1 Optical Properties of Semiconductors

The optical properties of semiconductor alloys, specifically, crystal structure and band gap energy, as well as their relation to light emission and absorption, make them ideal materials for photonic integration. In this section, we will cover topics such as how the elemental fractions in the alloys affect crystal lattice parameters and band gap energy, as well as how these relate to active devices such as electro-optic modulators. These topics are presented with particular attention to ternary and quaternary semiconductors such as indium gallium arsenide phosphide (InGaAsP) and aluminum gallium arsenide (AlGaAs) because of their prevalence in optical communications and integration with photonic circuits. Finally, we draw specific attention to an $In_{1-x}Ga_xAs_{1-y}P_y$ on SiO_2 (InGaAsP-on-insulator) photonics platform, to provide improvements in passive device performance, which can be coupled together with active devices for monolithic material integration.

1.1.1 Lattice parameters of semiconductors

III-V semiconductors are materials found in groups III and V of the periodic table, with unique optical and electronic properties suitable for light emission, high-frequency modulation, and efficient absorption. This group of materials is unique for integrated photonics because of the versatility and tunability of different alloy compositions. Binary, ternary, and quaternary alloys can be found in various applications from visible to mid-infrared wavelengths. Within the visible spectrum (λ = 380 nm - 750 nm), binary semiconductors such as gallium nitride (GaN) [47] and aluminum nitride (AlN) [48] are commonly used for light emission. It should also be noted that many ternary and quaternary semiconductors, such as InGaN and AlGaInP, are also used for emission at visible wavelengths. Furthermore, within the near infrared wavelength range (780 nm - 2500 nm), ternary semiconductor alloys such as aluminum gallium arsenide ($Al_xGa_{1-x}As$) [25], and indium gallium arsenide, ($In_{1-x}Ga_xAs$) [49, 50] are commonly used for light-emission and detection. In addition, quaternary semiconductors such as indium gallium arsenide phosphide ($In_{1-x}Ga_xAs_{1-y}P_y$) [39, 51] and indium gallium arsenide antimonide ($In_{1-x}Ga_xAs_ySb_{1-y}$) [52] are also commonly used for light-emission and detection within the near-infrared range, up to 2 μm. In this section, we will explore the lattice parameters and band gap energies of III-V semiconductors, which make them beneficial platforms for integrated photonics.

The lattice constant for crystalline materials depends on the physical dimensions of the atoms within a unit cell of its crystal structure. The atoms are arranged in specific systems called lattice types, defined by the lattice dimensions (a, b, c) and angles (α, β, γ). Cubic

lattice types, such as zinc-blende, are face-centred cubic crystal structures, with equal dimensions ($a = b = c$) and 90° angles between its edges ($90° = \alpha = \beta = \gamma$). For III-V semiconductors, the variation of the lattice constants relates to the band structure and band gap energy, as explained by Vegard's law, where the variation of the alloy concentrations causes the lattice constant to change linearly with the band gap energy. Using methods such as density functional theory (DFT) for calculating the band gap energy based on the interatomic distances, the lattice constant, and energy gaps of alloys can be determined. As illustrated in Fig. 1.1 [53, 54], the band gap energies are plotted as a function of the lattice constant for binary (red dot), ternary, and quaternary alloys (solid lines). For semiconductor alloys that have matching lattice constants, it is possible to epitaxially grow one alloy on another with minimal defects, such as dislocations.

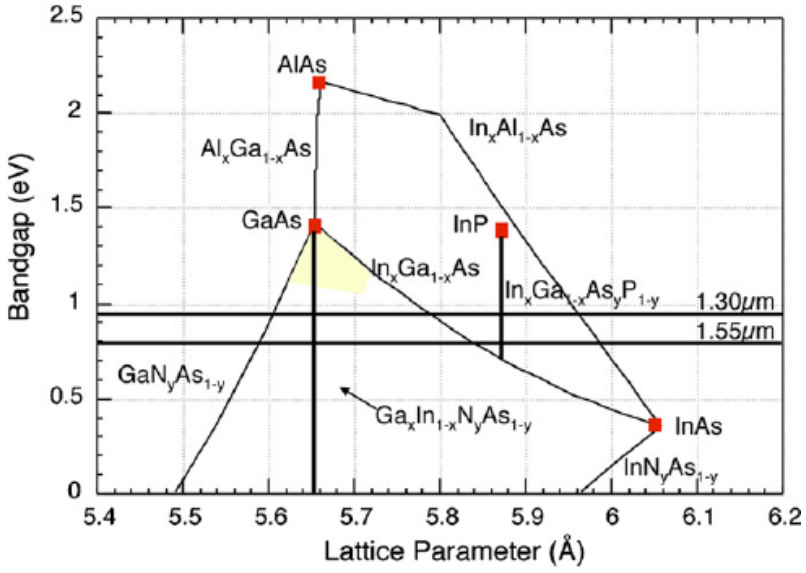

Figure 1.1: Band gap energy (eV) vs lattice parameter (Å) of different semiconductor alloys. Figure taken from [54].

The concentrations of the elements needed for lattice-matched growth of quaternary semiconductors are described in [55], by

$$x = \frac{A_0 + B_0 y}{C_0 + D_0 y}, \tag{1.1}$$

Where the coefficients A_0, B_0, C_0, and D_0 have different values for different value for example:

$$\text{GaAs substrate} : x = \frac{0.4050 - 0.1893y}{0.4050 + 0.0132y}, \tag{1.2}$$

$$\text{InP substrate} : x = \frac{0.1893 - 0.1893y}{0.4050 + 0.0132y}. \tag{1.3}$$

Here, in Eqs. (1.1) - (1.3), the coefficients needed for lattice-matched growth of InGaAsP are calculated, for both InP and GaAs substrates. The coefficients $\mathrm{A}_0, \mathrm{B}_0, \mathrm{C}_0$ and D_0 are given by Eqs. (1.2) and (1.3), as referenced in [55].

1.1.2 Band Gap energy of InGaAsP

The band gap energy is the energy range between the highest energy state of the valence band and the lowest energy state of the conduction band in a solid, where no electronic states exist. The electronic states are the energy levels of the atoms to which electrons can be promoted, or from which electrons can emit photons. Thus, to promote an electron from the valence band to the conduction band, additional energy input is required, usually described in units of electron volts (eV). For semiconductors, this range is typically between 0.1 and 3 eV; above this range, the material is an insulator, and below this range, it is a metal. For semiconductors, electrons may be promoted to the conduction band with photons (light) or phonons, discretized lattice vibrations carrying low energy but large momentum, $\vec{k}$. Using the coefficients from Eqs. (1.2) and (1.3), the respective band gap energies for InGaAsP quaternaries grown on either GaAs or InP are calculated, as described in [55],

$$\text{InGaAsP/GaAs} : E_0 = 1.43 + 0.30y + 0.18y^2, \tag{1.4}$$

$$\text{InGaAsP/InP} : E_0 = 0.75 + 0.46y + 0.14y^2. \tag{1.5}$$

Following Eqs. (1.4) and (1.5) in [55], the concentrations of the respective semiconductor elements for InGaAsP provide different ranges of band gap energies between 0.75 - 1.35 eV for InGaAsP/InP, and 1.43 - 1.91 eV for InGaAsP/GaAs. In this thesis, we will present integrated photonic components designed for a unique platform of $In_{0.14}Ga_{0.86}As_{0.3}P_{0.7}$,

grown on an InP substrate and bonded to SiO_2. This concentration allows for low propagation loss at telecom wavelengths (λ = 1260 nm - 1675 nm), due to photon energies below the band gap energy. However, equally important is the high rate of two-photon absorption for InGaAsP, where two photons are absorbed to promote electrons to the conduction band, discussed further in section 1.4.

Using Eqs. (1.4) and (1.5), the band gap energy for the chosen InGaAsP quaternary, $In_{0.14}Ga_{0.86}As_{0.3}P_{0.7}$, grown on InP and GaAs, is calculated as,

$$\text{GaAs substrate}: \quad E_0 = 1.728 \;\; eV = 717 \text{ nm}, \tag{1.6}$$

$$\text{InP substrate}: \quad E_0 = 1.141 \;\; eV = 1086 \text{ nm}. \tag{1.7}$$

This composition provides a telecom operational range further from the band gap energy than other compositions for low propagation loss. Considering two-photon absorption, all compositions of InGaAsP exhibit this effect, making low two-photon absorption compositions impossible; it is traditionally best to have a bandgap wavelength less than half of the operational wavelength. For operation at λ = 1.55 μm, the ideal band gap wavelength to minimize two-photon absorption should be λ < 775 nm (E_g > 1.6 eV). High rates of two-photon absorption exist for all compositions of InGaAsP, as demonstrated in [56, 57], the two-photon absorption rate in InGaAsP/InP multi-layer heterostructures has been reported as high as 60 cm/GW. Even considering this, the prevalence of InGaAsP as a common material platform for semiconductor lasers at telecom wavelengths makes it an attractive material for developing passive optical components and nonlinear optical

processes for photonics integration.

1.1.3 Active Devices

Active devices are components such as lasers, modulators, or photodetectors that require external power to generate, modulate, or detect light in photonic circuits. The incorporation of active devices in photonic circuits is essential to making capable devices for data and communications applications, with specific attention to electro-optic phase modulators [58], multi-quantum well lasers [59], and avalanche photodiodes [60].

Among materials used in active devices, those with direct band gaps are especially useful. A direct band gap is where the energy difference between the maximum energy of the valence band states and the minimum energy of the conduction band states corresponds to the same momentum, $\vec{k}$, of an electron [61]. Materials with indirect band gaps, such as silicon, require additional momentum compensation to achieve the promotion of an electron from the maximum of the valence band to the minimum of the conduction band. As shown in Fig. 1.2, in the case of an indirect-bandgap semiconductor, the difference in momentum between the valence and conduction band states needs additional momentum compensation, $\vec{k}$, which is typically provided for by phonons, since photons do not possess the momentum needed to achieve momentum conservation in these systems [61]. For light emission in indirect bandgap materials, the simultaneous emission of a photon and lattice vibration is highly unlikely, and for this reason, materials such as silicon are not used as light emitters. In contrast, direct bandgap semiconductors such as InGaAsP and AlGaAs

(for x < 0.45) are efficient light emitters. This property makes them ideal for semiconductor lasers and detectors in integrated photonic circuits.

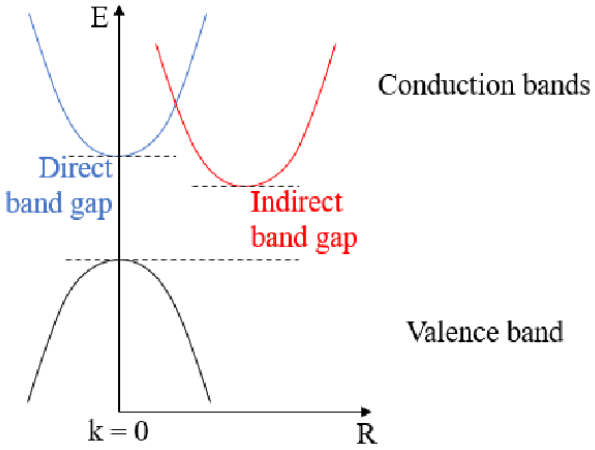

Figure 1.2: Direct vs indirect band gap, where the highest state in the valence band and lowest state in the conduction bands for direct and indirect band gap semiconductors are depicted with Energy along the y axis, and momentum along the x axis. Figure from [62]

.

Active semiconductor components such as lasers, modulators, and detectors are based on the work of p-n semiconductor junctions (positive-negative junctions). The p-side has a higher concentration of mobile holes that can move freely through the crystal lattice, and the n-side has a higher concentration of mobile electrons. The interface of these two regions creates a carrier-free depleted region (intrinsic layer) where no current flows, and an electric field with a barrier voltage opposing charge diffusion is formed [61]. When an external voltage is then applied to the junction, it will create a forward bias, allowing for current to flow and the recombination of electrons and holes for coherent light emission.

The construction of semiconductor lasers has advanced through the use of double-

layer heterostructures, modifying the density of states in both the conduction and valence bands. In these structures, a smaller band gap semiconductor (active layer) is sandwiched between two higher band gap p-doped and n-doped semiconductors. Electrons and holes in the valence and conduction bands become confined to the active layer, and injected charge carriers can participate in the lasing action of the system [13]. When the thickness of the active layer in the double heterostructures is reduced to a scale near the de-Broglie wavelength, $\lambda \approx \frac{h}{p}$, where p is the momentum of an electron, discrete energy levels are formed in the active layer, and a quantum well laser is achieved [63]. This type of structure has a higher density of states, a larger differential gain, and a decreased temperature sensitivity compared to larger heterostructures [64]. Multi-quantum-well lasers (MQWs) build upon this concept by incorporating multiple quantum wells, alternating active and barrier layers 10-20 nm in thickness. More wells improve the efficiency of the laser by increasing the density of states, quantum confinement, and allowing for more recombination opportunities in the active layers. Also, there are low absorption losses owing to the band gap mismatch of the emitted photons with the surrounding barrier layers. This confined recombination of electrons and holes in the active layer and low absorption losses give an increased optical gain, decreased threshold current, and tunable emission wavelength from the thickness of the quantum wells. [63–65]. An example of this process is shown in Fig. 1.3.

The invention of the semiconductor laser in 1962 by IBM, General Electric, and MIT Lincoln Labs marked the development of GaAs p-n junctions in compact integrated active components [13, 38, 66, 67]. From the late 1980s, compact semiconductor lasers based

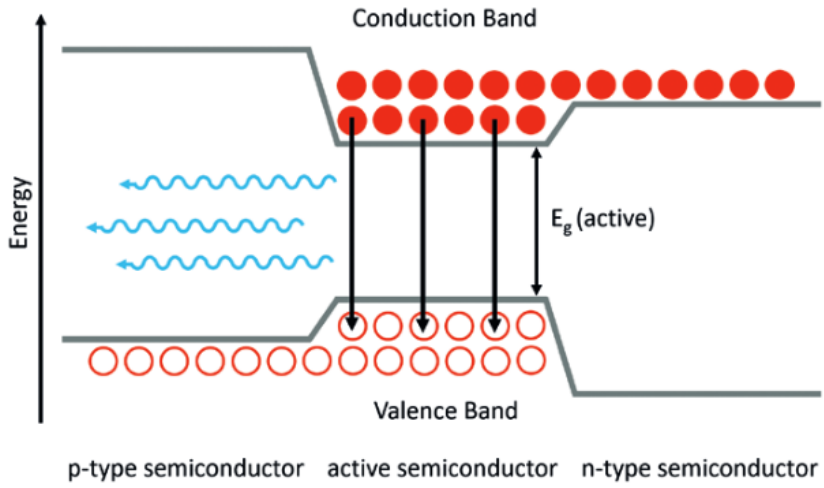

Figure 1.3: Energy diagram of charge carrier recombination in a double heterostructure for continuous wave emission. Figure from [63].

on AlGaAs and InGaAsP were deployed in long-distance communication networks, driven by advances in fabrication methods such as liquid phase epitaxy (LPE), molecular beam epitaxy (MBE), and metal organic chemical vapour deposition (MOCVD) [13, 68, 69]. Improvements in AlGaAs semiconductor lasers have come from these advances in thin film fabrication, with an emission range between 600-900 nm [13]. Further developments of MOCVD marked improvements in the InGaAsP/InP platform, with compact InGaAsP semiconductor lasers suited for integration with fibre optic communication systems. These lasers have the benefits of low transmission losses and high data transmission rates in wavelength ranges of approximately 1100 to 1600 nm, covering a wide range of frequencies.

In addition to semiconductor lasers, electro-optic modulators are especially relevant in the design of active components using III-V semiconductors. These devices change the

refractive index, and phase using an applied voltage and thus wave guiding properties of devices such as optical switches [70–73]. III-Vs are especially useful for this application due to their strong electro-optic and electro-absorption effects, providing high-speed and low-voltage modulation. Three common modulation methods using III-Vs are the Pockels effect for $\chi^{(2)}$ materials, the Kerr effect ($\chi^{(3)}$ effect), and free carrier absorption.

The Pockels effect linearly modulates the refractive index of non-centrosymmetric materials, such as zinc-blende semiconductors. This effect operates faster than other electro-optic effects, typically within picosecond time scales [74]. When a static low-frequency electric field is applied to an anisotropic material, such as an asymmetrical dielectric waveguide, the field vector representation of the energy density, for the electric field in the material, is an ellipsoid described by an index ellipse (indicatrix) [75]. The change in the refractive index of the indicatrix is described by

$$\Delta\left(\frac{1}{n^2}\right)_i = \sum_j r_{ijk} E_j, \tag{1.8}$$

where r_{ijk} is the electro-optic coefficient of the material, for materials belonging to the $\overline{4}3m$ space group, such as InGaAsP and AlGaAs. The equivalent electro-optic tensor simplifies elements of the electro-optic tensor, $r_{41} = r_{52} = r_{63}$, reducing the matrix complexity of the

tensor coefficients, r_{ij},

$$r_{ij} = \begin{bmatrix} r_{11} & r_{12} & r_{13} \\ r_{21} & r_{22} & r_{23} \\ r_{31} & r_{32} & r_{33} \\ r_{41} & r_{42} & r_{43} \\ r_{51} & r_{52} & r_{53} \\ r_{61} & r_{62} & r_{63} \end{bmatrix}. \tag{1.9}$$

This coefficient has been measured in AlGaAs and InGaAsP/InP to be approximately -1.43 pm/V and -1.34 pm/V, for an x fraction of 0.17 in $Al_xGa_{1-x}As$ and a y fraction of 0.20 in $In_{1-x}Ga_xAs_{1-y}P_y$, respectively [55, 76].

The Kerr effect differs from the Pockels effect in that it is a $\chi^{(3)}$ effect. The effect is characterized by the intensity-dependent refractive index,

$$n(I) = n_0 + n_2 I, \tag{1.10}$$

$$n_2 = \frac{3\chi^{(3)}}{4n_0^2\epsilon_0 c}. \tag{1.11}$$

Here, the material refractive index changes because of the nonlinear index, n_2, and intensity of the incident wave, I. The nonlinear index, n_2, is characterized by the third order nonlinear susceptibility, $\chi^{(3)}$, and the linear refractive index, n_0.

The last type of electro-optical modulation discussed in this section is free carrier absorption. This is an important type of modulation for semiconductors, where charge carriers can be injected or depleted in different regions to change the density of states within

the valence and conduction bands and thus the absorption properties of the material. These effects are described by intraband-free carrier absorption effects from the concentration of electrons and holes, leading to a change in the refractive index [77, 78],

$$\Delta n = -\left(\frac{e^2\lambda^2}{8\pi^2 c^2 \epsilon_0 n}\right)\left(\frac{N}{m_e} + P\,\frac{m_{hh}^{\frac{1}{2}} + m_{lh}^{\frac{1}{2}}}{m_{hh}^{\frac{3}{2}} + m_{lh}^{\frac{3}{2}}}\right), \tag{1.12}$$

where e is the charge of an electron, λ is the free space wavelength, n is the refractive index, m_e, m_{hh}, m_{lh} are the electron, heavy hole, and light hole effective masses, respectively, and N and P are the doping concentrations of charge carriers [77].

The optical properties of semiconductors give rise to unique interactions within the band diagram, and thus, electro-optic effects, useful for making efficient lasers, modulators, and photodetectors. This property contributes to the unique optical properties of semiconductors, making them useful materials for building both active and passive devices on the same monolithic platform [79]. Modulation techniques such as the Pockels effect, Kerr effect, and electro-absorption modulation induce refractive index changes in waveguides on the order of 10^{-3}, depending primarily on the charge carrier concentrations and voltage. In this way, III-V semiconductors such as AlGaAs and InGaAsP are good candidates to incorporate high-speed modulation in compact devices[77]. Furthermore, the development of the on-insulator platform presented in this thesis provides the opportunity for high-performance and tunable monolithic devices, with increased optical confinement as demonstrated by developments in AlGaAs-on-insulator [25, 80, 81].

1.2 Waveguide Theory

An optical waveguide is an essential building block for any integrated photonic component because it is responsible for routing light between different components in a circuit. The ability to achieve low-loss propagation of light in waveguides is an important consideration when designing photonic circuits. When light propagates, it experiences effects such as self-phase modulation (SPM), group velocity dispersion (GVD), scattering, and absorption losses, all of which distort and attenuate the optical signal. Scattering and absorption are the main sources of loss, while GVD and SPM affect the temporal profile or spectrum of the signal. Thus, a clear understanding of how light propagates in optical waveguides is essential for predicting device performance. In this section, we present the basic derivation of the electromagnetic modes seen in channel waveguide geometries such as buried/immersed strip, embedded, ridge, rib, and strip-loaded waveguides, illustrated in Fig. 1.4. With particular attention to a dielectric slab waveguide, illustrated in Fig. 1.5, the related effective refractive index is also used as an example for understanding light

propagation in optical waveguides using Maxwell's equations,

$$\vec{\nabla} \cdot \vec{E} = \frac{\rho}{\epsilon_0}, \tag{1.13}$$

$$\vec{\nabla} \cdot \vec{B} = 0, \tag{1.14}$$

$$\vec{\nabla} \times \vec{E} = \frac{\partial \vec{B}}{\partial t}, \tag{1.15}$$

$$\vec{\nabla} \times \vec{B} = \mu_0 \vec{J} + \mu_0 \epsilon_0 \frac{\partial \vec{E}}{\partial t}. \tag{1.16}$$

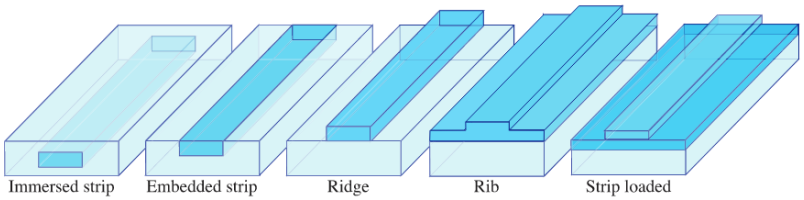

Figure 1.4: 2D channel waveguide geometries where the darker colour indicates a higher refractive index, going from left to right: Immersed/buried strip waveguide, Embedded strip waveguide, Ridge waveguide, Rib waveguide, and Strip-loaded waveguide. Figure from [82], chapter 9.3.

General treatment of Eqs. (1.13) - (1.16) (Maxwell's equations) typically requires a full vectorial solution, found using numerical methods such as the finite difference method implemented in finite difference eigenmode solvers (FDE solvers) or finite-difference-time-domain solvers (FDTD solvers). Following from Eqs. (1.13) - (1.16), the wave equations

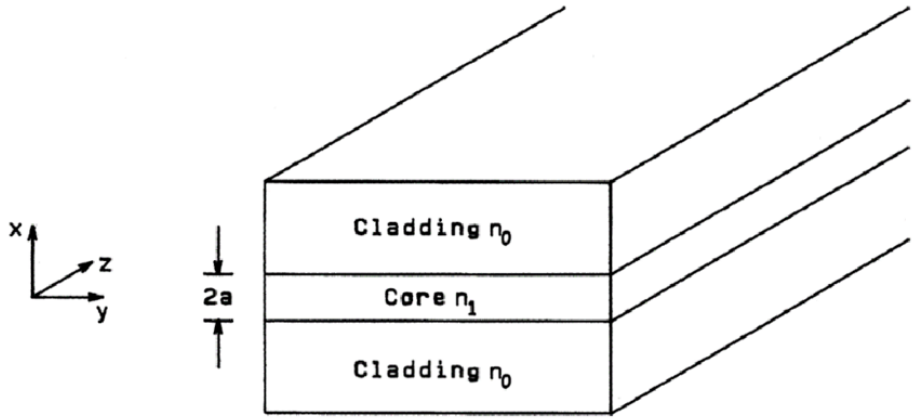

Figure 1.5: Dielectric slab waveguide. Figure from [83].

for the electric and magnetic fields can be derived as

$$\frac{\partial^2 \vec{E}}{\partial t^2} = \frac{1}{\mu_0 \epsilon_0} \nabla^2 \vec{E}, \tag{1.17a}$$

$$\frac{\partial^2 \vec{B}}{\partial t^2} = \frac{1}{\mu_0 \epsilon_0} \nabla^2 \vec{B}, \tag{1.17b}$$

providing a basis for the analysis of dielectric waveguides in time and space.

For solving for the allowed modes of a simple dielectric slab waveguide, pictured in Fig. 1.5, the wave equations (Eqs. (1.17a) and (1.17b)) for the electric and magnetic fields are used with plane wave solutions to the electric and magnetic fields,

$$\tilde{E} = \vec{E}(x,y)e^{i(\omega t - \beta z)}, \tag{1.18}$$

$$\tilde{H} = \vec{H}(x,y)e^{i(\omega t - \beta z)}. \tag{1.19}$$

In Eqs. (1.18) and (1.19), the substitution for the magnetic field strength, H, is used, where B = $\mu_0 \vec{H}$. The parameter β denotes the propagation constant in the transverse z-direction and represents the accumulated change in phase per unit length for the guided wave [83],

$$\beta = \frac{2\pi}{\lambda} n_1 \cos(\phi), \tag{1.20}$$

$$\kappa = \frac{2\pi}{\lambda} n_1 \sin(\phi). \tag{1.21}$$

Here, ϕ is the inclination angle of light in the waveguide. This value determines part of the propagation constant and must be less than the maximum angle determined from the total internal reflection condition. This angle is determined by the critical angle at the core-cladding interface described by,

$$\theta_{\max} \leq sin^{-1}\sqrt{n_2^2 - n_1^2}, \tag{1.22}$$

also known as the numerical aperture (NA), where n_2 is the refractive index of the core, and n_1 is the index of the cladding. Substituting these solutions into Maxwell's equations

gives the following six coupled equations for the electric and magnetic field components in Cartesian coordinates:

$$\frac{\partial \vec{E_z}}{\partial y} + j\beta \vec{E_y} = -i\omega\mu_0 \vec{H_x}, \tag{1.23a}$$

$$-\frac{\partial \vec{E_x}}{\partial x} - j\beta \vec{E_x} = -i\omega\mu_0 \vec{H_y}, \tag{1.23b}$$

$$\frac{\partial \vec{E_y}}{\partial x} - \frac{\partial \vec{E_x}}{\partial y} = -i\omega\mu_0 \vec{H_z}, \tag{1.23c}$$

$$\frac{\partial \vec{H_z}}{\partial y} + j\beta \vec{H_y} = i\omega\epsilon_0 n^2 \vec{E_x}, \tag{1.23d}$$

$$-\frac{\partial \vec{H_z}}{\partial x} - i\beta \vec{H_x} = j\omega\epsilon_0 n^2 \vec{E_y}, \tag{1.23e}$$

$$\frac{\partial \vec{H_y}}{\partial x} - \frac{\partial \vec{H_x}}{\partial y} = i\omega\epsilon_0 n^2 \vec{E_z}. \tag{1.23f}$$

The electromagnetic fields in the dielectric slab waveguide do not have a y-axis dependency ($\partial E/\partial y = 0$, $\partial H/\partial y = 0$), thus permitting two types of independent guided modes, the transverse electric (TE) and transverse magnetic (TM) modes. The TE mode wave equation is characterized by its electric field transverse to the direction of propagation, such that $\vec{E_z} = 0$.

$$\frac{d^2\vec{E}}{dx^2} + \left(k^2 n^2 - \beta^2\right) \vec{E_y} = 0. \tag{1.24}$$

Similarly, for the TM mode wave equation, it is polarized transverse to the direction of

propagation, such that $\vec{B}_z = 0$,

$$\frac{d}{dx}\left(\frac{1}{n^2}\frac{d\vec{H}_y}{dx}\right) + \left(k^2 - \frac{\beta^2}{n^2}\right)\vec{H}_y = 0 \tag{1.25}$$

.

Finding the allowed modes in waveguides is more commonly performed using tools such as finite-difference eigenmode solvers, which can be used to determine the allowed electromagnetic modes, effective index, group index, and dispersion parameters of optical waveguides.

In contrast, for low-index contrast waveguides and simple geometries, semi-analytical solutions using the effective index method are possible. The effective index is a dimensionless value of the weighted average ratio of the refractive indices in a waveguide, determined by the field distribution over the core, cladding, and substrate materials, and described by the equation,

$$n_{eff} = \frac{\beta}{k_0}, \tag{1.26}$$

where,

$$k_0 = \frac{2\pi}{\lambda}, \tag{1.27}$$

is the vacuum wavenumber. Considering the effective index, for the light to be confined to

the core material n_2, the condition,

$$n_1 \leq n_{\text{eff}} \leq n_2, \tag{1.28}$$

must be satisfied, where the effective index of a guided mode has a value between that of the cladding and core material. When the effective index falls below the refractive index of the cladding, n_1, the field along the transverse direction is dissipated from the core as a radiation mode [83]. More methods for studying wave propagation in optical waveguides are discussed in [83, 84]. In later chapters, the allowed modes for an InGaAsP-on-insulator waveguide are examined, using the effective index determined from an FDE solver.

In addition to the effective index and TE/TM mode characteristics of waveguides, the mode operation, either single-mode or multi-mode propagation, will be crucial for specific applications. In single-mode operation, only the fundamental mode, typically the TE_{00} or TM_{00} mode in waveguides, will be confined to the structure; this minimizes modal dispersion, transmission loss, and provides a higher transmission speed in optical communication networks. Multi-mode operation allows for higher-order electromagnetic modes to propagate within the structure and can support higher data transmission at the cost of speed, increased transmission losses, and increased dispersion [15].

Finally, in the consideration of optical pulse propagation in waveguides, dispersion is an important parameter that has two main contributions: material and waveguide dispersion. Material dispersion comes from the wavelength dependence of the refractive index, while waveguide dispersion is caused by wavelength-dependent field confinement influenced by

waveguide geometry. In high-index contrast waveguides, such as the platform proposed in this thesis, waveguide dispersion is typically higher at longer wavelengths and smaller waveguide geometries that are less confined to the core material. Because of this, the waveguide geometry is an important design parameter for integrated photonic circuits that influences the amount of light confined to the core material and the overall dispersion experienced by the guided modes.

1.3 Finite-Difference Time-Domain Simulation

The design of photonic integrated circuits requires simulation tools capable of modelling the propagation of electromagnetic (EM) waves for accurate and efficient prediction of the device performance. The advantages of simulation allow designers to predict the performance without needing to fabricate extensive amounts of prototypes, thus reducing cost and physical testing, and enabling faster iterations between designs. These benefits underline the importance of capable simulation tools for photonic devices, where devices undergo complex and costly fabrication processes at foundries [85]. This section will convey concepts of the finite-difference time-domain (FDTD) method by including a description and basic derivation of the FDTD algorithm one-dimensional case. Numerical methods such as FDTD are essential because, although analytical solutions to Maxwell's equations can be determined for simple geometries such as slab waveguides and cylindrical optical fibres, the designed photonic components discussed in later chapters have more complex structures and cannot be described analytically.

The FDTD method, first called Yee's Algorithm, was first proposed by Kane S.Yee in 1966 as a discrete finite-difference solution to Maxwell's equations in the time and space derivatives of the curl equations [86]. For a one-dimensional plane-wave, with an electric field oriented in the x-direction, a magnetic field in the y-direction, and propagation in the z-direction, the curl equations,

$$\frac{\partial \vec{E}}{\partial t} = \frac{1}{\epsilon_0}\frac{\partial H_y}{\partial z}, \tag{1.29}$$

$$\frac{\partial H_y}{\partial t} = \frac{1}{\mu_0}\frac{\partial E_x}{\partial z}, \tag{1.30}$$

allow us to take central difference approximations of both the spatial and temporal derivatives. In the FDTD method, Maxwell's curl equations are discretized in a grid, one cell of the grid being a "Yee cell", to update the electric and magnetic fields along different points in time and space. For an established cell in time and space, the curl equations for the electric field are calculated along the line edges of the unit cell, and the magnetic curl equations are computed along the faces of the cell, depicted below in Fig. 1.6.

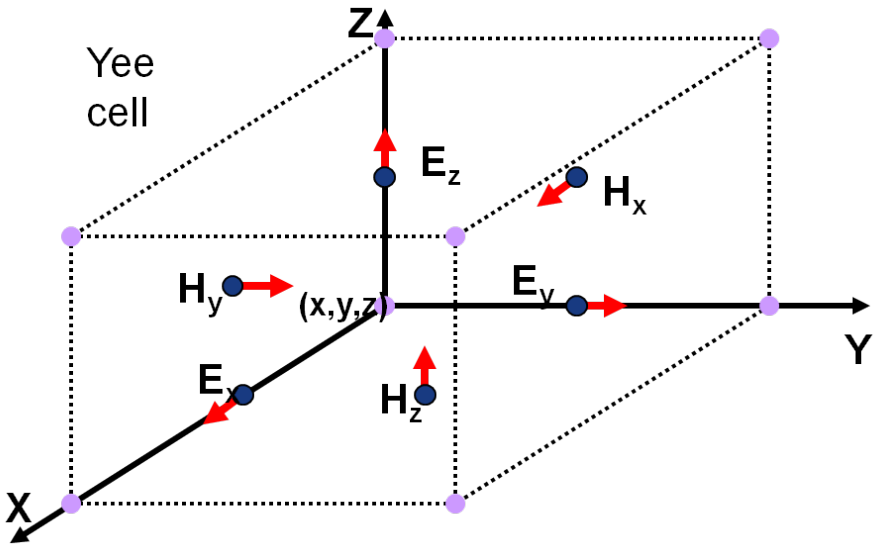

Figure 1.6: Yee grid cell in FDTD method. Figure from [87].

Solving these equations is done in discrete time steps where the fields are updated in alternating half-time steps; the electric fields are calculated from the curl of the magnetic fields, and the magnetic fields, $\vec{B}$, are calculated from the curl of the electric field. Fre-

quency domain information is calculated from the Fourier transform of the recorded time domain information and at the simulation boundaries, perfectly matched layers (PML) are commonly used to minimize the effect of reflections and evanescent waves on simulation results. Using this method, light can be injected into a simulation area, and as it evolves through the structure, the field information from the electric and magnetic fields is recorded in time and space, and a reconstruction of the spectrum, field evolution, effective indices, and resonant-like properties can be obtained.

To understand the alternating half-time steps in the FDTD method, the derivation of the fields for one-dimensional propagation of a plane wave is considered. In this example, the electric field is oriented in the x direction, the magnetic field in the y direction, and the propagation in the z direction. Eqs. (1.29) and (1.30) are used in a central difference approximation of the temporal and spatial derivatives used in a Yee cell, [88]:

$$\frac{\vec{E_x}^{\,n+\frac{1}{2}}(k) - \vec{E_x}^{\,n-\frac{1}{2}}(k)}{\Delta t} = -\frac{1}{\epsilon_0}\frac{\vec{H_y^n}(k+\frac{1}{2}) - \vec{H_y^n}(k-\frac{1}{2})}{\Delta x}, \tag{1.31}$$

$$\frac{\vec{H_y}^{\,n+1}(k+\frac{1}{2}) - \vec{H_y}^{\,n}(k+\frac{1}{2})}{\Delta t} = -\frac{1}{\mu_0}\frac{\vec{E_x}^{\,n+1.2}(k+1) - \vec{E_x}^{\,n+1.2}(k)}{\Delta x}. \tag{1.32}$$

Within Eqs. (1.31)and (1.32), n indicates a time step $t = \Delta t * n$, and k indicates a spatial time step, $z = \Delta x * k$. Δx and Δt are calculated using

$$\Delta t = \frac{\Delta x}{2 * c_0}, \tag{1.33}$$

in a sufficiently small step, such that the simulation produces stable results. This is further related to the Courant–Friedrichs–Lewy condition (CFL-condition). In this condition, a dimensionless number, deemed the Courant number C, may have a maximum value, ensuring the spatial and temporal steps are small enough in the grid to accurately calculate the fields,

$$C = \frac{c_0 \Delta t}{\Delta x}. \tag{1.34}$$

Often, the maximum value chosen for the Courant number is ≈ 1. For values larger than one, the step in the grid may miss some grid cells and lead to incomplete data. Conversely, if a value much less than 1 is used, the simulation becomes unnecessarily long [89].

Initially, the FDTD method was proposed with the condition that a perfectly conducting boundary allows one to model the scattering of an EM wave from a perfectly conducting object [86]. Since the original formulation of Yee's Algorithm, development of the FDTD method has seen many improvements for field discretization, perfectly matched layers (PML) for absorbing boundaries [90], and models for dispersive, anisotropic, and non-linear materials [91]. These improvements have seen FDTD become a standard approach used in applications for accurate modelling of complex systems in optical communications [92], bio-photonics [93], and photovoltaics [94].

In summary, the FDTD method provides an essential tool for modelling the propagation of EM waves in photonic devices. The discretization of Maxwell's equations in time and space enables accurate prediction of field evolution, mode profile, and spectral response in complex geometries, where an analytical solution is not easily derived. FDTD is the

standard for accurate 3D simulation of devices following advances in field discretization, boundary layers, and diverse material models. In the following chapters, tools such as Lumerical FDTD, OptiFDTD, and Tidy3D are used for FDTD simulations to analyze device designs for the InGaAsP-on-Insulator platform.

1.4 Nonlinear Optical effects in III-V Semiconductors

Nonlinear optical effects are light-matter interactions in which the optical response of a material is not linearly proportional to the incident electric field. These effects are used in a wide range of applications such as fluorescence microscopy [56], long-distance optical communications [95, 96], and quantum information processing [97], highlighting the central role of nonlinear optics in modern photonic technologies [98–100]. III-V semiconductors exhibiting strong second- and third-order nonlinear susceptibility are especially relevant for frequency conversion in compact, integrated photonic circuits. In this section, we discuss how the nonlinear response of a material can be characterized by its polarizability,

$$\vec{P} = \epsilon_0[\chi^{(1)}\vec{E}(t) + \chi^{(2)}\vec{E}^2(t) + \chi^{(3)}\vec{E}^3(t) + ...]. \tag{1.35}$$

Here, higher-order contributions can be produced from the incident electric field, $\vec{E}(t)$, and nonlinear susceptibility tensors, $\chi^{(n)}$, which describe the strength of the material response at each nonlinear order.

When high-intensity light interacts with a nonlinear medium, there is a chance for new frequencies to be generated, as the incident field acts as a driver for the new frequencies.

This is described by the nonlinear wave equation,

$$\nabla^2 \vec{E} - \frac{\epsilon^{(1)}}{c^2} \frac{\partial^2 \vec{E}}{\partial t^2} = \frac{1}{\epsilon_0 c^2} \frac{\partial^2 \vec{P}_{NL}}{\partial t^2}, \tag{1.36}$$

where $\epsilon^{(1)}$ is the linear permittivity and $\vec{P}_{NL}$ is the nonlinear polarization with contributions from higher order susceptibilities. This differs from the regular wave equation, Eq. (1.17a), by including a nonlinear polarization term that acts as a source for new frequency components.

The specific nonlinear response also depends on the crystal structure of the material. III-V semiconductors such as InGaAsP and AlGaAs possess non-centrosymmetric zinc-blende crystal structures, resulting in a non-zero second-order susceptibility, $\chi^{(2)}$. With this property, these materials can support second-order nonlinear effects such as sum frequency generation, second harmonic generation, difference frequency generation, and spontaneous parametric down-conversion. The InGaAsP-on-insulator platform presented in this work is particularly useful for nonlinear optics due to its large nonlinear susceptibility and large refractive index contrast between the core and cladding materials. For InGaAsP, at $\lambda = 1.55$ μm, the index contrast with SiO_2 is approximately $3.27 - 1.44 = 1.83$. This high index contrast improves optical confinement, described by

$$\Gamma = \frac{\int_{\text{core}} |\vec{E}^2| dA}{\int_{\text{total}} |\vec{E}^2| dA}, \tag{1.37}$$

and leads to an increased electric field intensity within the nonlinear waveguide, thereby

improving the efficiency of nonlinear optical interactions compared with a bulk crystal.

When the nonlinear interaction involves frequencies far from materials' resonances, where absorption and dispersion are low, Kleinman's symmetry, a type of permutation symmetry for the χ susceptibility tensor, may be applied. Kleinmann symmetry assumes that the nonlinear susceptibility is frequency independent, allowing the permutation of the indices of the second-order susceptibility tensor, $\chi^{(2)}$, to reduce the number of elements in the susceptibility tensor. An example of this symmetry for a second-order nonlinear process is

$$\vec{P}_i(\omega_l = \omega_n + \omega_m) = \epsilon_0 \sum_{jk} \sum_{nm} 2d_{ijkl} \vec{E}_j(\omega_n) \vec{E}_k(\omega_m), \tag{1.38}$$

where the coefficients, d_{ijk}, of the nonlinear susceptibility tensor $\chi^{(2)}$, are denoted by the components [75],

$$d_{ijk} = \frac{1}{2} \chi^{(2)}_{ijk}. \tag{1.39}$$

Among many nonlinear optical processes, second-order interactions are especially important. In second-harmonic generation, two photons of the same frequency, ω_1, will interact in a nonlinear material to emit one photon at frequency $2\omega_1$, as illustrated in Fig. 1.7. In this thesis, in Chapter 4, novel waveguide geometries for InGaAsP-on-insulator are designed for second-harmonic generation, converting infrared to telecom wavelengths. Similarly, in sum frequency generation, two photons of different frequencies combine to generate one photon at frequency $\omega_3 = \omega_1 + \omega_2$. Second harmonic generation and sum

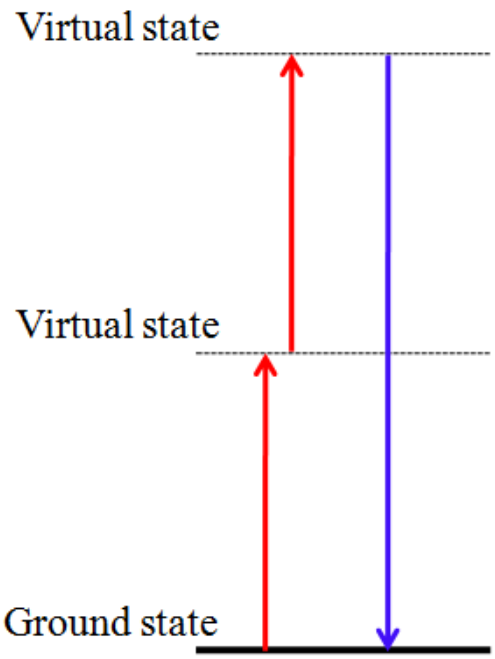

Figure 1.7: Second harmonic generation energy level diagram.

frequency generation can be applied to signal conversion for easier detectability in integrated devices from infrared to visible wavelengths, as well as imaging of tissues such as collagen and certain protein structures[101, 102]. In difference frequency generation, two photons of different frequencies interact in a nonlinear medium to produce a third photon at frequency $\omega_3 = |\omega_1 - \omega_2|$. Difference frequency generation is commonly used to generate mid-infrared and THz frequencies, which can be important for molecular sensing applications [103, 104]. In spontaneous parametric down-conversion (SPDC), a single higher-frequency photon is converted into two lower-frequency photons such that energy

and momentum are conserved, $\omega_1 = \omega_2 + \omega_3$. SPDC is commonly used in quantum information and communication due to its ability to produce two photons that are entangled in polarization and time with each other [75]. The efficient operation of all of these processes is enforced through phase matching of the given wavevectors in the coupled waves, such that momentum conservation is true, $\Delta k = 0$.

To describe the intensity-dependent refractive index change in nonlinear materials, the nonlinear index, n_2, is introduced. The change in the refractive index with intensity I is given by

$$n(I) = n_0 + n_2 I, \tag{1.40}$$

where n_0 is the linear refractive index. The nonlinear index, n_2, is related to the third-order susceptibility by

$$n_2 = \frac{3\chi^{(3)}}{4n_0^2\epsilon_0 c}. \tag{1.41}$$

Here, I is the intensity of light in units of $\mathrm{W/m^2}$, and the nonlinear index is used to define the nonlinear coefficient,

$$\gamma = \frac{n_2\omega_0}{cA_{\mathrm{eff}}}, \tag{1.42}$$

which has units of $\mathrm{W^{-1}m^{-1}}$. Here, the nonlinear coefficient, γ, is used to describe the accumulated nonlinear phase shift, ϕ_{NL}, by an optical wave,

$$\phi_{NL} = \gamma P L, \tag{1.43}$$

where P is the optical power, and L is the propagation length. These effects give rise to

phenomena such as self-phase modulation, where intensity-dependent phase shifts lead to spectral broadening of an optical pulse, as illustrated in Fig. 1.8.

To describe the propagation of optical pulses in a dispersive nonlinear medium, the nonlinear Schrodinger equation (NLSE) is used with the slowly varying envelope approximation,

$$\frac{\partial A(z,t)}{\partial z} + \frac{i\beta_2}{2}\frac{\partial^2 A(z,t)}{\partial t^2} + i\gamma|A^2(z,t)|A(z,t) = 0, \tag{1.44}$$

where β_2 describes the group velocity dispersion and γ accounts for the Kerr nonlinearity contributing to effects such as self-phase modulation. The balance between the dispersion and the nonlinear coefficient can lead to the formation of temporal optical solitons, whose field envelope is given by

$$A(z,t) = A_s^0 \text{sech}\left(\frac{\tau}{\tau_0}\right) e^{i\kappa z}, \tag{1.45}$$

where $\kappa = -\beta_2 = \gamma|A_s^0|^2\tau_0^2$, $|A_s^0|$ is the amplitude, and τ_0^2 is the full width half-max (FWHM) pulse duration. Soliton formation occurs when the group velocity dispersion, β_2, and the nonlinear coefficient γ have opposite signs.

Another third-order effect in nonlinear materials relevant for InGaAsP is two-photon absorption. As illustrated in Fig. 1.9, two-photon absorption occurs when two photons with energies approximately equal to half the band gap energy, $E_g/2$, are absorbed simultaneously. This effect occurs for all compositions of the InGaAsP alloy in the telecom wavelength range due to higher lying conduction bands present in the electronic band structure. The total absorption coefficient for a nonlinear material can thus be expressed as

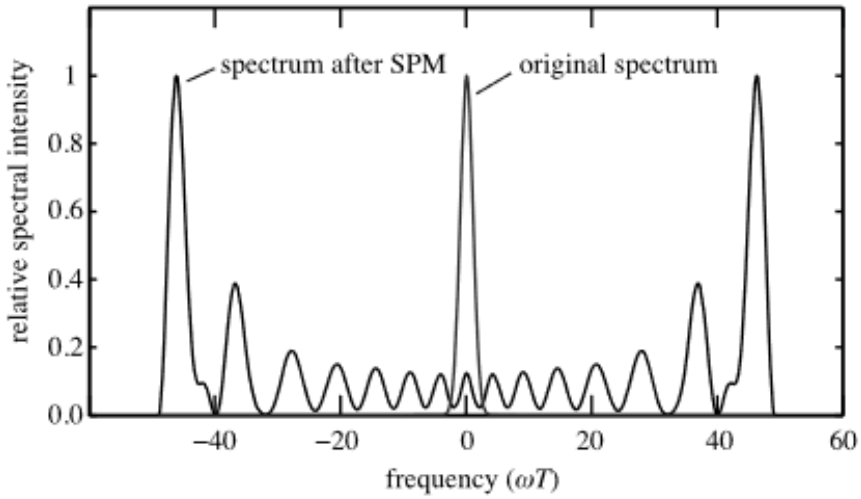

Figure 1.8: Self phase modulation of an optical pulse. Figure from [75].

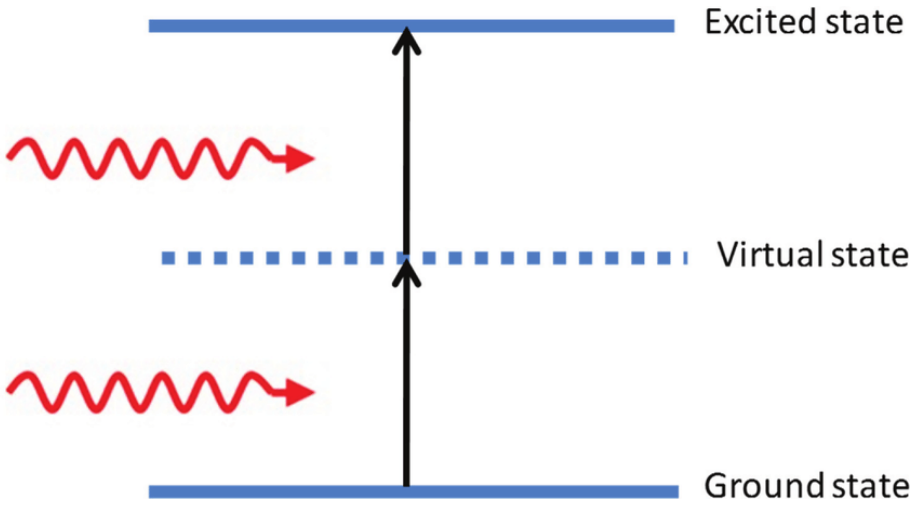

Figure 1.9: Energy diagram for two photon absorption. Figure from [105].

$$\alpha = \alpha_0 + \beta I, \tag{1.46}$$

where α_0 is the linear absorption coefficient, β is the two-photon absorption coefficient, commonly in units of cm/GW, and I is the intensity. Other third-order processes include third-harmonic generation, four-wave mixing, and cross-phase modulation, which are discussed in detail in [75], but are beyond the scope of this thesis.

The nonlinear processes discussed in this section are important considerations for the design of photonic components. Efficient devices for frequency-conversion require careful engineering of phase matching, dispersion, optical confinement, and absorption losses. In the following chapters, these principles are applied to the design and analysis of nonlinear devices implemented on the InGaAsP-on-insulator photonic platform, with specific mention in Chapter 4, discussing InGaAsP-on-insulator waveguides for second-harmonic generation.

1.5 Subwavelength Integrated photonics

The field of subwavelength integrated photonics was first realized in silicon by Dr. Pavel Cheben and Dr Jens Schmid, our collaborators for the design of the InGaAsP-on-insulator meta-waveguides presented in this thesis, which have currently never been realized in a III-V on-insulator platform. Since it's conception, subwavelength photonics have greatly enhanced the field of silicon photonics having a strong influence on the development of integrated optical components for dispersion engineering [106–110], record low-loss optical coupling [111–120], and size reduction in the footprint of photonic components. The advantages of subwavelength photonics are realized through manipulation of the refractive index distribution at scales much smaller than the operating wavelength. Since the field's conception, subwavelength structures have proved especially useful for applications in bio-sensing [121–124], and data and optical communications [114, 116, 125], benefiting from compact geometries which provide a wide operation bandwidth and low-loss. In this thesis, Chapter 3 presents the designs of a meta-waveguide in the form of a subwavelength grating (SWG) waveguide and subwavelength grating edge coupler, based on InGaAsP-on-insulator at λ = 1.55 μm. This work was performed in collaboration with Dr. Pavel Cheben and Dr. Jens H. Schmid at the National Research Council of Canada and demonstrates the versatility of the InGaAsP-on-insulator platform as a novel platform for designing subwavelength structures.

Subwavelength integrated photonics owes some of its conception to previous work on

periodic dielectric structures, which were considered early on by Yablonovitch and John [126, 127], who explored periodic modulation of dielectric materials leading to optical effects described by photonic band-gap structure, specifically, the photonic band-gap. The periodicity of such structures results in Bragg reflections in a specific spectral window, where the forward propagation of light is prevented [112]. In subwavelength devices, the core material (n_1) is periodically segmented with a lower index cladding (n_2) at a pitch Λ, much smaller than the propagating wavelength ($\Lambda \ll \lambda$), allowing the periodic refractive index to be treated as a quasi-homogeneous waveguide [112, 116]. For such periodic materials, the supported modes are represented by Floquet-Bloch modes, where the periodicity in the direction of propagation leads to a dependence of the electric field that is described by a plane wave with a periodic function [112, 128],

$$E(x, y, z) = F(x, y, z)e^{-ikz}, \tag{1.47}$$

where $F(x, y, z) = F(z, y, z + \Lambda)$ is periodic, and the exponential term, e^{-ikz} describes the phase of the Floquet-Bloch mode as it propagates along the unit cells. In the phase term, the complex Bloch wave vector, k, has real and imaginary components, $k = k_r + ik_i$. In the wavevector, k_r is the real part of the complex Bloch wave vector and is related to the effective index of the Floquet-Bloch mode by $k_r = (2\pi n_F/\lambda)$. With this condition, the

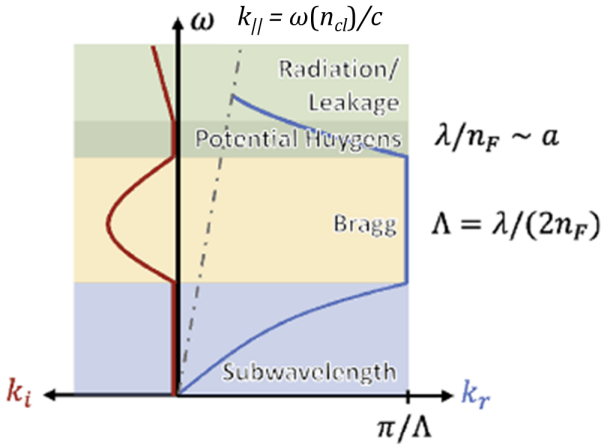

Figure 1.10: Subwavelength propagation regime diagram, where the real Bloch wavevector values are positive and to the right of the ω axis and the imaginary values are negative and to the left of the axis. Figure from [112].

propagation of the Floquet-mode falls into three different regimes:

- Lossless guided regime : $k_r > 0,\ k_i = 0,\ \Lambda < \lambda/(2n_F)$ (1.48)

- Bragg regime (Bandgap) : $k_r > 0,\ k_i < 0,\ \Lambda = \lambda/(2n_F)$ (1.49)

- Radiative regime : $k_r > 0,\ k_i < 0,\ \Lambda > \lambda/(2n_F)$ (1.50)

To understand how light will propagate in the periodic medium, the real and imaginary parts of the Floquet-Bloch wave vector are analyzed, as illustrated in Fig. 1.10. In all regions $k_r > 0$, and in the areas where $k_i \leq 0$, the guided wavelength λ_g will experience either the Bragg regime, where light is gradually attenuated and reflected, or the radiative regime, where the light leaks into the cladding and substrate. In the regime below the band gap ($\Lambda > \lambda/(2n_F)$), $k_r > 0$ and $k_i = 0$. Here, light achieves lossless propagation, where it propagates without the effects of diffraction, similar to a homogeneous waveguide.

These different regimes are described by the ratio of the pitch, Λ, and guided wavelength, λ_g. The Bragg regime, where light is reflected, occurs when $\Lambda = \lambda_g/(2n_F)$, the lossless regime below the bandgap occurs when $\Lambda < \lambda/(2n_F)$, and the radiative regime occurs when $\Lambda > \lambda/(2n_F)$; in this regime the light leaks into the cladding and substrate. In addition, the guided and unguided regimes for light in periodic structures are also described in relation to the lightline, $k_{||}$, in Fig. 1.10. The lightline describes the dispersion relation for radiative modes in the cladding and, in general, serves as the cutoff condition for guided and leaky Floquet-Bloch modes, where modes below the lightline are guided, and those above leak into the cladding. In addition, for regions far below the band gap ($\Lambda \ll \lambda$), the periodic waveguide can be thought of as a uniaxial homogeneous effective medium with an equivalent permittivity tensor,

$$\frac{\epsilon}{\epsilon_0} = n_{eq}^2 = \begin{bmatrix} n_{||}^2 & 0 & 0 \\ 0 & n_{||}^2 & 0 \\ 0 & 0 & n_{\perp}^2 \end{bmatrix}, \tag{1.51}$$

where n_{eq}^2 is the equivalent effective index of the infinite laminar medium. As well as ϵ_0, the vacuum permittivity, and $n_{||}^2$ and $n_{\perp}^2$ are the effective indices of a plane wave polarized in the parallel and perpendicular axes of the grating interfaces, respectively. These indices are described by the pitch and duty cycle of the periodic waveguide,

$$n_{||}^2 \approx \frac{a}{\Lambda} n_1^2 + \left(1 - \frac{a}{\Lambda}\right) n_2^2 + O\left(\frac{\Lambda^2}{\lambda^2}\right), \tag{1.52}$$

$$n_{\perp}^{-2} \approx \frac{a}{\Lambda} n_1^{-2} + \left(1 - \frac{a}{\Lambda}\right) n_2^{-2} + O\left(\frac{\Lambda^2}{\lambda^2}\right). \tag{1.53}$$

In Eqs. (1.52) and (1.53), a is the width of the core material with higher index, n_1, while Λ is the pitch of the periodic cell, λ is the free space wavelength and $O\left(\frac{\Lambda^2}{\lambda^2}\right)$ is a correction term with a static value that helps with correction closer to the band gap [129].

To understand the formation of the photonic band structure, the Bloch periodic boundary conditions are applied to a periodic dielectric medium. By using the symmetry of the unit cell, the solutions to the Floquet-Bloch modes are described by an eigenvalue problem when the boundary is restricted to the unit cell, with the fields satisfying the Bloch periodicity of a wavevector k. For a fixed Bloch wavevector k within the first Brillouin zone, the eigenvalue problem will yield a discrete set of frequencies, $\omega_n(k)$, where n is the band-index. As the Bloch wavevector is varied across the Brillouin zone, each frequency traces out a specific dispersion relation $\omega_n(k)$, forming a photonic band. The collection of these dispersion relations makes up the photonic band structure, describing the allowed frequencies that can propagate in a periodic dielectric medium [128]. In Chapter 3, a lossless

subwavelength grating waveguide and a high-efficiency subwavelength grating edge coupler are designed as part of the unique and high-performance subwavelength components that contribute to the InGaAsP-on-insulator platform.

1.6 Process Design Kit creation

A process design kit (PDK) is a library of basic and component-level building blocks (waveguides, couplers, and phase modulators), provided or supported by a fabrication facility for the efficient design of integrated circuits [130, 131]. A comprehensive PDK includes layer stack information such as refractive indices, layer thicknesses, and etching depths, as well as design rules such as minimum feature sizes, spacings, alignment specifications, and tolerances. In addition, a PDK typically contains parameterized cells (P-cells), compact models, and design verification tools. P-cells allow designers to customize components within the library, while compact models contain analytical or empirical models of component performance for circuit simulations. These models often include parameters such as effective index, group index, propagation loss, and dispersion, and may be derived from numerical simulations or experimental device characterization. This section addresses the requirements for PDK development and highlights the role of component design in the manufacturing of integrated photonic circuits. The discussion begins with the state of Canada's semiconductor and photonics industry in a global context, followed by the essential elements of a PDK, and how component design is important for PDK construction, as well as the benefits of an InGaAsP/SiO_2 photonic platform.

The adoption of photonic technologies has improved industries such as telecommunications, medical sensing, and quantum information processing [39, 132, 133]. In Canada, however, broad adoption is limited by the domestic design and fabrication capability of

semiconductor-based photonic components. Currently, there are only five semiconductor packaging facilities in Canada and only one publicly operated fabrication facility in North America with capabilities for Indium Phosphide (InP) wafers; namely, the Canadian Photonics Fabrication Centre (CPFC) [134]. Currently, the CPFC runs at full capacity and can address the needs of large enterprises; this leaves the research and development needs of small and medium enterprises, as well as academic institutions, unfilled. As part of Canada's strategy to improve the adoption of photonics technologies, a streamlined and accessible design-to-fabrication pathway is required that leverages existing Canadian fabrication infrastructure. Such pathways would allow users to make use of multi-project wafer runs (MPWs), where different users aggregate designs on one fabrication run, reducing the cost barriers and dependence on large commercial foundries such as TSMC and Global Foundries [85, 135]. Initiatives such as the Fabrication of Integrated Components for the Internet's Edge network (FABrIC) showcase progress in these areas [136]. The development of capable PDKs for versatile material platforms directly supports these national efforts and helps establish Canada as a valuable international partner in the commercialization of photonic technologies.

Component performance in PDKs is often represented using compact models based on scattering parameters (S-Parameters), which describe the net transmission and reflection characteristics between ports of a component. By representing this information as an S-matrix, a black box description for designed components in circuit simulations can be achieved, where the fabrication centre retains access to detailed fabrication process details, while the designer only has access to the modelled performance of the component [130].

This is beneficial for retaining specific intellectual property in the fabrication centre.

Within the workflow of a PDK, the component library is used at both the layout and schematic layers to perform a layout versus schematic (LVS) verification before final tape-out. The S-parameters provide information for generating a circuit netlist, defining the connectivity details between ports at the schematic level, which can then be imported to circuit simulation tools such as Ansys Lumerical Interconnect or OptiSpice. At the layout level, the components are represented using GDSII format for the mask design, and connectivity is defined from the port definitions found by doing a design check of the schematic netlist. From these parameters, circuit-level simulations can be performed for both frequency-domain transmission analysis and time-domain system modelling. Once complete, the design rule checks in place ensure the LVS verification has consistency between the layout and schematic levels, verifying that the physical implementation matches the intended circuit design.

The work presented in this thesis helps contribute to the development of a III-V semiconductor PDK by providing a passive-component library for the InGaAsP on SiO_2 (insulator) platform. Focusing on passive devices in the telecommunication O-band (1260 nm - 1360 nm) and C-band (1530 nm - 1570 nm), these contributions include: GDSII component layouts, associated S-parameter models, and waveguide effective index, group index, and dispersion models suitable for circuit-level simulations. The proposed component designs are based on a 220 nm guiding layer of $In_{0.14}Ga_{0.86}As_{0.3}P_{0.7}$, with a 3 μm SiO_2 substrate and top cladding, as illustrated in Fig. 1.11. This creates a structure with strong optical confinement and compatibility with standard single-etch fabrication processes.

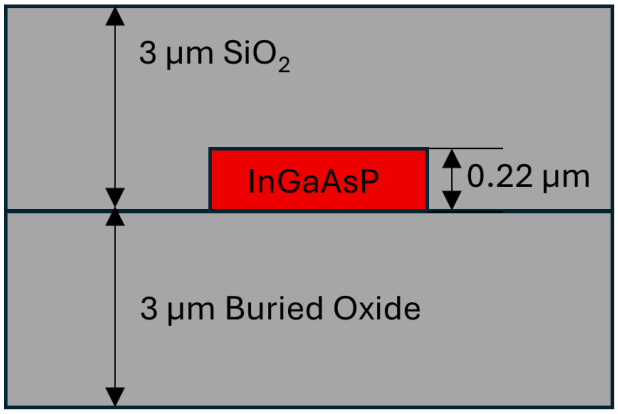

Figure 1.11: InGaAsP-on-insulator material stack.

1.7 Thesis Outline

The objective of this thesis is to present component designs for a novel material platform, InGaAsP-on-insulator, that can be used to integrate passive components capable of nonlinear photonics into monolithic photonic circuits. This would combine light sources, optical modulators, low-loss signal routing, and optical detection on the same chip. The designed components along with their associated wavelength ranges and polarizations are listed in Table 1.1. As a whole, the designed components in this thesis also lay the foundation for a component library for the InGaAsP-on-insulator platform that will create a valuable and necessary tool for building application-specific integrated photonic circuits as part of a process design kit.

An advantage of the InGaAsP-on-insulator platform is that it can be combined with active devices such as lasers, amplifiers, modulators, and detectors, which can all be grown

on Indium Phosphide, and bonded to silica (SiO_2). The versatility of having many components grown on the same material allows for enhanced functionality in photonic circuits that combine active and passive photonic components within a high-index contrast platform.

In the sections of this thesis, in Chapter 1, information on the optical properties of semiconductors, waveguide theory, numerical simulation methods for electromagnetic waves, relevant nonlinear optical effects, subwavelength integrated photonics, and process design kit creation is covered. In Chapter 2, material models for InGaAsP and simulation results for the designed components, developed in collaboration with Optiwave Systems Inc., are included. In Chapter 3, the design and analysis of a subwavelength meta-waveguide and subwavelength edge coupler, developed in collaboration with Dr. Pavel Cheben and Dr. Jens H. Schmid at the National Research Council of Canada (NRC), are included. Finally, in Chapter 4, designs for a nonlinear optical waveguide are presented for second harmonic generation from infrared to telecom wavelengths. The work presented in this thesis builds the foundation for a novel and versatile material platform, capable of nonlinear photonics and low-loss signal routing. In addition, these designs can also be incorporated into a process design kit for high-index contrast III-V materials with strong optical confinement and dispersion control.

Table 1.1: List of designed photonic components, wavelength ranges, and polarizations

Components	wavelength	polarizations
straight Waveguide	1550 nm, 1310 nm	TE, TM
Bent Waveguide	1550 nm, 1310 nm	TE, TM
Linear Waveguide Taper	1550 nm, 1310 nm	TE, TM
Y-Branch	1550 nm	TE, TM
2 × 2 MMI	1550 nm	TE
2 × 2 Directional Coupler	1550 nm	TE
Waveguide X-crossing	1550 nm	TE, TM
Subwavelength Waveguide	1550 nm, 1310 nm	TE
Subwavelength Edge Coupler	1550 nm	TE, TM

2

Chapter 2: Integrated Photonic Component Design

Integrated photonic circuits are important devices for the routing and processing of optical signals used in a wide range of applications, from sensing to optical data communications. These devices can be application-specific by assembling basic components such as those listed in Table 1.1, whose performance is defined by the transmission across different optical ports. These components are typically developed through a combination of analytical modelling, numerical simulation, and layout-level verification, where the performance is characterized using modal properties of the propagating light and scattering parameters (S-parameters) denoted by S_{ij}, where i is the receiving port and j is the sending port. In this Chapter, component-level modelling and validation are presented, developed in collaboration with Optiwave Systems Inc., with special mention to Cem Bonfil and Dr. Scott Newman for their feedback and guidance on device design and simulation testing. This collaboration leverages an industry-academic partnership for achieving results using standard design and simulation tools. The overall goal of the work presented here is to design and characterize passive photonic components for integration into a scalable process design kit for the InGaAsP-on-insulator material platform.

2.1 Software and Hardware specifications

The components presented in chapters 2 and 3 were modelled using a combination of 2D and 3D FDTD software, including OptiFDTD 16.0.1.2624 for preliminary 2D simulations on a Windows 11 system with an i7-9750H CPU and 16 GB of RAM. For 3D simulations, the Tidy3D web interface from Flexcompute was used. This is a cloud-based GPU-based FDTD software that greatly improves simulation time for 3D simulations. In Chapter 3, the subwavelength components presented were simulated using a dedicated simulation computer with a 13th Gen Intel(R) Core(TM) i9-13900K CPU with 32 cores and 128 GB of RAM, using Lumerical 2024 R1 version 1.9.3633. Python and Lumerical scripts developed with the help of generative AI tools such as ChatGPT and Claude were used to perform analytical modelling of the results of waveguide compact models, the effective coupling length of the 2 $\times$ 2 directional coupler, and theoretical efficiency of the second-harmonic generation waveguides. These scripts were then verified by the author and compared with results from numerical simulations.

2.2 Waveguide Modelling and Analysis

Optical waveguides are physical structures that confine and guide electromagnetic waves along a defined path. These structures serve as the fundamental building blocks of photonic devices, routing light on both chip-scale and fibre-based platforms. Various waveguide structures have been explored for photonic platforms in 3-layer, 2-layer, and multi-layer structures. As illustrated in Fig. 2.1, examples in AlGaAs include strip-loaded waveguides in 3-layer systems, on-insulator platforms in 2-layer systems, and quantum well waveguides in multi-layer systems [137].

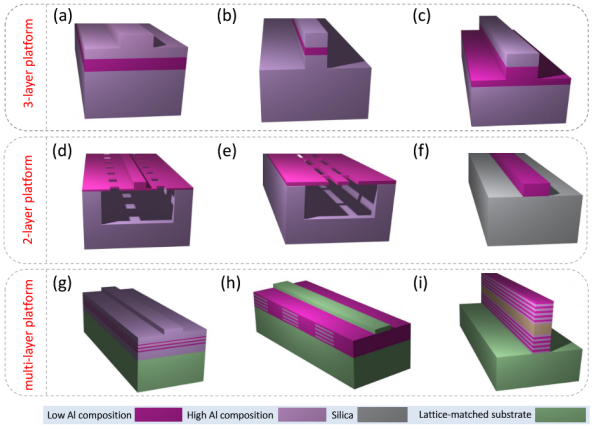

Figure 2.1: Waveguide material stacks in AlGaAs. Figure from [137]

Building on established waveguide architectures, this section details the steps taken for creating compact waveguide models of a buried oxide InGaAsP-on-insulator waveguide, where the oxide acts as a low-index cladding. This includes the material models used for the InGaAsP, convergence testing for determining waveguide parameters, and analytical

modelling techniques for the optical performance of the InGaAsP waveguide at telecom wavelengths.

2.2.1 Material Refractive Index Models

For modelling the optical response of materials in photonic circuits, accurate dispersion models are important for producing rigorous results. The design of passive photonic components for $In_{0.14}Ga_{0.86}As_{0.3}P_{0.7}$ requires reliable optical response data models below the band gap energy ($E_g = 1.1eV \ = 1127$ nm). In these transparent regions, the absorption is minimal, while the refractive index still exhibits variation with the wavelength. Common dispersion modelling approaches include methods such as polynomial fitting of the refractive index data, Sellmeier, and Lorentz-Drude models. Sellmeier equations are often used to describe the refractive index in the spectral regions with little linear absorption, particularly for wavelength regions below the bandgap energy, and are therefore well suited for modelling InGaAsP at telecom wavelengths. The Lorentz-Drude model describes the optical and electrical response of dielectric materials through the combination of the Drude model to describe free electrons in a material and the Lorentz model to describe the optical response of bound electrons. This approach is especially useful when free-carrier or absorption effects must be included over a broad spectral range. Polynomial fitting of refractive index data offers flexibility in describing the refractive index through the accuracy of different polynomial orders, and is typically valid over certain wavelength ranges. Examples of how these dispersion models are applied can be seen in various applications,

such as modelling 2D thin films [138], studying the optical properties of transition metals [91, 139], and investigating the permittivity of materials over large spectral windows [140].

The refractive index data of $In_{0.14}Ga_{0.86}As_{0.3}P_{0.7}$ used for modelling the components presented in this thesis is based on the approach described in [141]. In this approach, the refractive index, n, for photon energies below the bandgap is described by an analytical expression,

$$n = \sqrt{A\left[f(x_0) + \frac{1}{2}\left(\frac{E_0}{E_0+\Delta_0}\right)^{1.5} f(x_{os})\right] + B}, \tag{2.1}$$

where

$$f(x_0) = x_0^{-2}\left(2 - \sqrt{1+x_0} - \sqrt{1-x_0}\right), \tag{2.2}$$

$$f(x_{os}) = x_{os}^{-2}\left(2 - \sqrt{1+x_{os}} - \sqrt{1-x_{os}}\right), \tag{2.3}$$

$$x_0 = \frac{\hbar\omega}{E_0}, \tag{2.4}$$

$$x_{os} = \frac{\hbar\omega}{E_0+\Delta_0}. \tag{2.5}$$

In Eqs. (2.1) − (2.5), the coefficients A and B are obtained through linear interpolations of experimental binary compound data. The parameter A describes the contributions from the electronic transitions at the fundamental band gap energy, E_0, and the split-off band transition at $E_0 + \Delta_0$. The parameter B describes the approximate non-dispersive

contribution of higher energy electronic transitions to the refractive index. Furthermore, to extend the refractive index model across a wide wavelength range for photonic simulations, this refractive index data of $In_{0.14}Ga_{0.86}As_{0.3}P_{0.7}$ in the transparent regime is fitted to a three-term Sellmeier model described by

$$n^2(\lambda) = 1 + \sum_j \frac{A_j \lambda^2}{\lambda^2 - C_j}, \tag{2.6}$$

with the coefficients

$$n^2(\lambda) = 1 + \sum \frac{0.699\lambda^2}{\lambda^2 - (0.810)} + \frac{0.023\lambda^2}{\lambda^2 - (1.102)} + \frac{8.455\lambda^2}{\lambda^2 - (0.0525)}, \tag{2.7}$$

where λ is expressed in micrometers and the resonance coefficients C_j have the units of μm^2.

Using the refractive index data for $In_{0.14}Ga_{0.86}As_{0.3}P_{0.7}$ derived from Eq. (2.1) and Eq. (2.7), the corresponding Sellmeier equation fitting is illustrated in Fig. 2.2. This fitting provides a compact and computationally efficient representation of the material dispersion for use in modelling photonic components with FDTD simulations.

The Sellmeier Eq. (2.6) is identical to that produced from modelling the refractive index in the lossless regime, $\Gamma = 0$, for the Lorentz-Drude model,

$$\epsilon = 1 + \sum_{i=1}^{M} \frac{A_i \lambda^2}{\lambda^2 + j\Gamma_i \lambda - \lambda_i^2}, \tag{2.8}$$

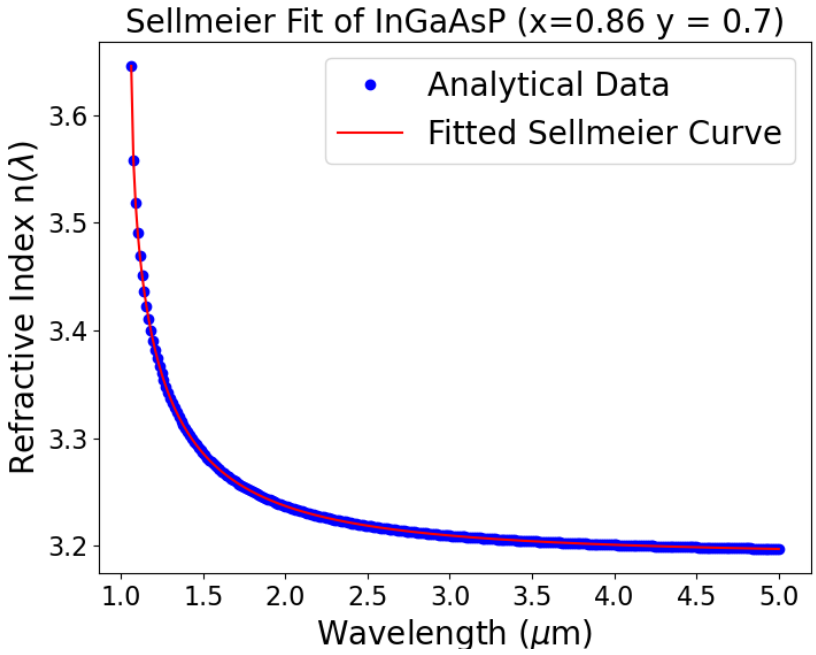

Figure 2.2: Sellmeier fit for the refractive index data of $In_{1-x}Ga_xAs_{1-y}P_y$ (x=0.86,y=0.7) $R^2 = 0.999997$

where ϵ is the relative permittivity and the refractive index is given by $n = \sqrt{\epsilon}$. The damping term, Γ, is included in the Lorentz-Drude model, which describes the electron scattering and absorption in conductive and lossy materials. Since Γ is assumed to be zero below the band gap energy, in this case, the Lorentz-Drude model reduces directly to the Sellmeier form, recovering Eq. (2.6),

2.2.2 Convergence testing

Reliable numerical simulations and mode solvers require convergence testing, which ensures physically accurate results and minimizes numerical errors arising from poor spatial and time resolution. One approach for convergence testing is to improve the mesh resolution in 2D simulations until the results approach a stable value. Commonly, this resolution is chosen to be approximately one-tenth of the wavelength inside the material, λ/n, where n is the refractive index of the waveguide core [142]. This is important because, in numerical simulations, the correct solution is always an approximation within some numerical error determined by factors such as spatial discretization and boundary conditions.

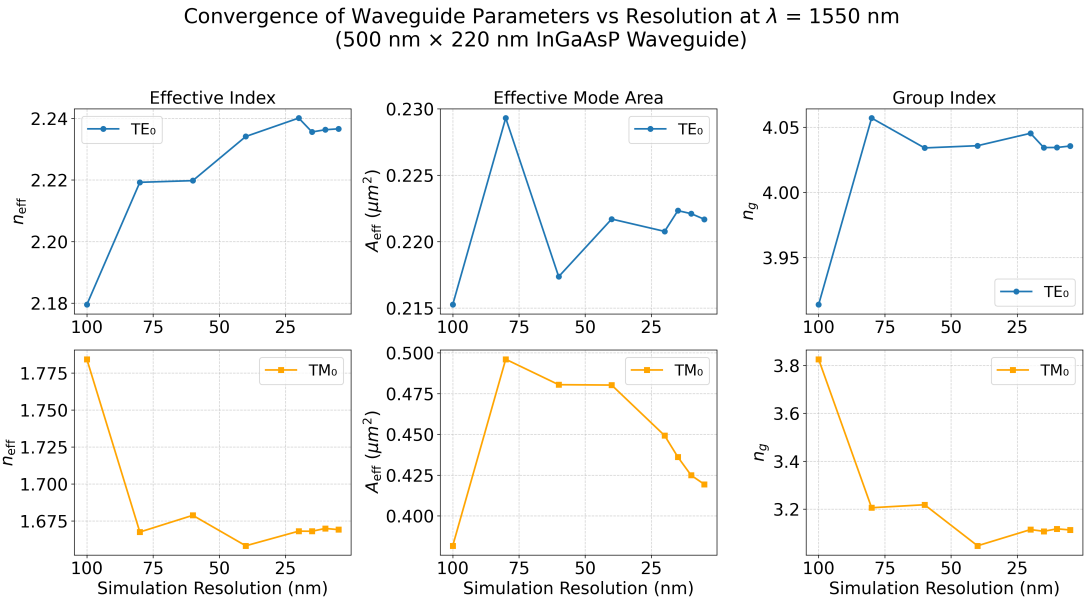

Figure 2.3: Convergence testing with the resolutions of 100 to 5 nm for the effective index, effective mode area, and group index of a 500 nm × 220 nm InGaAsP waveguide.

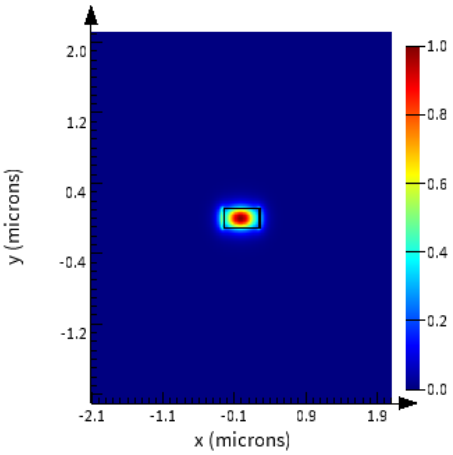

(a) TE_{00} mode profile at 5 nm resolution (linear scale).

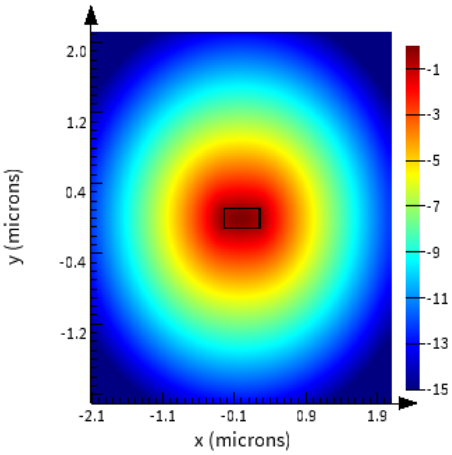

(b) TE_{00} mode profile at 5 nm resolution (log scale).

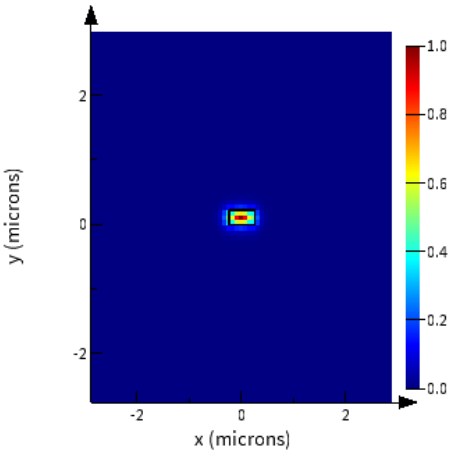

(c) TE_{00} mode profile at 80 nm resolution (linear scale).

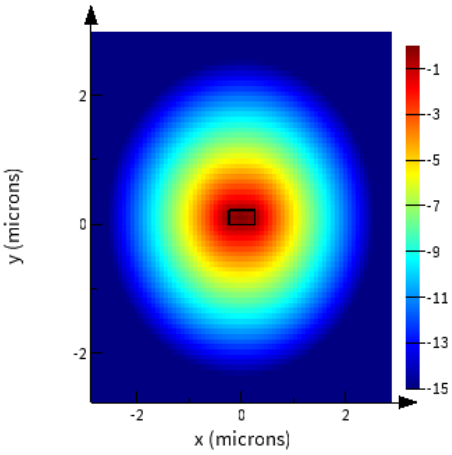

(d) TE_{00} mode profile at 80 nm resolution (log scale).

Figure 2.4: Linear and logarithmic scale plots of the TE_{00} mode field for 5 nm and 80 nm computational resolutions, where the colour plot indicates the normalized electric field amplitude (a.u).

To perform a convergence test for the InGaAsP-on-Insulator waveguides, the spatial resolution of the finite-difference eigenmode (FDE) solver was increased from 80 nm to 5 nm at a wavelength of $\lambda = 1.55$ μm. As shown in Fig. 2.3, the variation in the extracted modal parameters gradually reduces as the mesh resolution is refined. Particularly, the effective index, mode area, and group index of the TE_{00} mode exhibit smaller variations as the grid size decreases, as illustrated in Fig. 2.4.

From these results, the changes of ≤ 0.002 in the values of the effective index, group index, and effective area are obtained for the mesh resolutions finer than approximately 20 nm, relative to the highest resolution used (5 nm). Although the convergence is not exact, this level of variation provides an acceptable level of precision for determining parameters such as the effective index and group index in FDE simulations and is sufficient for the generation of reliable models.

2.2.3 Waveguide Compact Models

Compact models of the effective index are valuable for understanding waveguide behaviour across wide wavelength ranges without requiring repetitive numerical simulations. Fitting effective index data over a wavelength interval to a polynomial expansion allows the effective index, group index, and dispersion to be expressed analytically, enabling efficient system-level modelling of waveguides for photonic circuit design.

Before determining polynomial fitting parameters, an appropriate waveguide width for single-mode operation must be calculated. This is achieved by sweeping the effective index

as a function of increasing waveguide widths at the telecom wavelength ranges, $\lambda = 1.55$ μm and $\lambda = 1.31$ μm. A guided mode requires that the effective index be larger than that of the cladding (SiO_2), such that $n_{\text{neff}} \geq n_{\text{clad}}$. To ensure single-mode operation, higher-order modes must become unguided (leaky) when their effective index satisfies $n_{\text{eff}} \leq n_{\text{clad}}$, which defines the cutoff condition for higher-order modes.

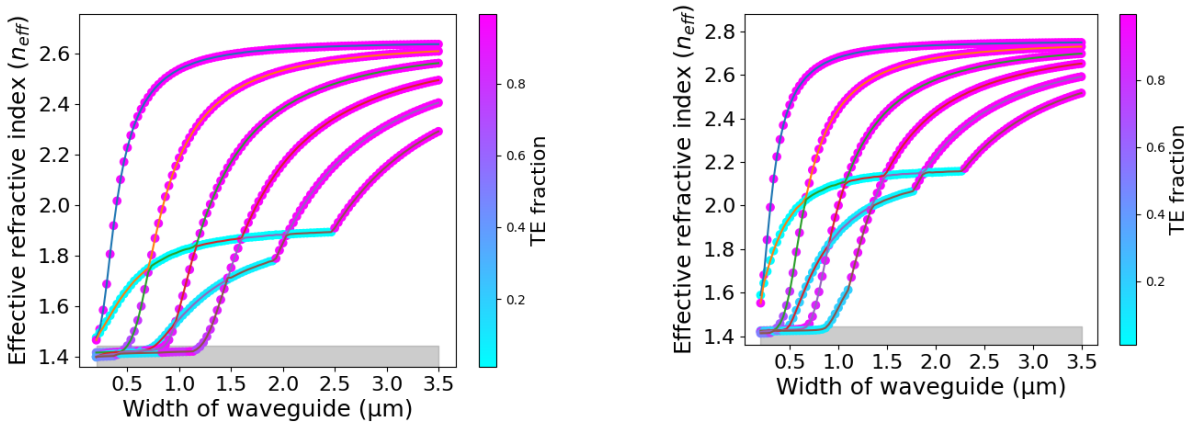

Figure 2.5: Effective index variation of the InGaAsP-on-insulator waveguide as a function of waveguide width for the first six modes, where gray is the cutoff condition, the pink colour represents the TE modes, and cyan colour represents the TM modes: (a) at $\lambda = 1550$ nm and (b) at $\lambda = 1310$ nm.

As shown in Fig. 2.5, the second magenta line indicating the TE_1 mode reaches a cutoff at approximately 500 nm in waveguide width for a fixed height of 220 nm at $\lambda = 1.55$ μm. At this width, the TE_{10} mode has an effective index near that of the cladding and is not guided ($n_{eff} \approx n_{clad}$). Consequently, a waveguide width of 500 nm supports only the fundamental TE_{00} and TM_{00} modes at ($\lambda = 1.55$ μm).

However, at 1.31 μm, the same 500 nm waveguide width does not fully satisfy the cutoff condition for the TE_{10} mode, which remains weakly guided with an effective index greater than the cladding $n_{eff} = 1.65 > n_{clad}$ ($n_{eff} \approx 1.65$). Despite this, a 500 nm waveguide width can still be considered appropriate in practice due to the strong mode confinement of the TE_{00} at $\lambda = 1.31$ μm. In this regime, higher-order modes are only weakly bound and therefore difficult to excite, particularly when the waveguide undergoes adiabatic tapering to only support the single-mode excitation.

The compact effective-index model is defined by

$$n_{eff}(\lambda) = A_1 + A_2(\lambda - \lambda_0) + A_3(\lambda - \lambda_0)^2, \tag{2.9}$$

which corresponds to a second-order Taylor expansion of the effective index centred about a central wavelength λ_0. Here, A_1 corresponds to the effective index at λ_0, A_2 determines the group index, and A_3 is used to calculate the dispersion, D, in units of s/m^2.

To determine the polynomial Taylor expansion coefficients, Eq. (2.9) is applied to effective index data over a finite wavelength range centred around the reference wavelength

λ_0, creating an analytical model of the effective index, group index, and dispersion using

$$n_0 = A_1, \tag{2.10}$$

$$n_g = A_1 - A_2\lambda_0, \tag{2.11}$$

$$D = \frac{-2\lambda_0 A_3}{c}. \tag{2.12}$$

The effective index data for the 500×220 nm waveguide were used to obtain polynomial fits over the ranges $1.26 - 1.36$ μm and $1.5 - 1.6$ μm. As illustrated in Fig. 2.6, the fitted curves in comparison with the simulated effective index data demonstrate good agreement across the wavelength ranges of interest. The polynomial expansion parameters, as illustrated in Fig. 2.6, for the fundamental TE and TM polarizations at both $1.26 - 1.36$ μm and $1.5 - 1.6$ μm wavelength regions are listed below in Table. 2.1.

Table 2.1: Effective Index Fitting Parameters

Coefficient	$\lambda_0 = 1.55$ μm TE	$\lambda_0 = 1.55$ μm TM	$\lambda_0 = 1.31$ μm TE	$\lambda_0 = 1.31$ μm TM
A_1	2.234	1.672	2.532	2.012
A_2	-1.163	-0.955	-1.372	-1.924
A_3	0.239	1.721	0.854	2.158

Table 2.1: Polynomial expansion fitting parameters for waveguide compact models are $\lambda = 1.55$ μm and $\lambda = 1.31$ μm in TE and TM polarization.

The examples of how these compact-model parameters are used to extract the effective index and group index in photonic devices, such as Mach-Zehnder interferometers and micro-ring resonators, can be found in [143–145]. Furthermore, using the compact model parameters, a group-velocity-dispersion (GVD) map can be calculated for a wide range of

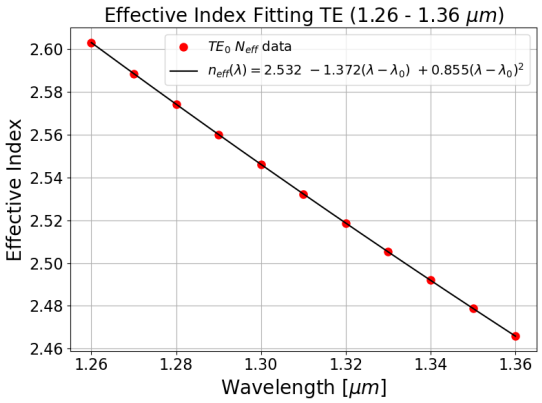

(a) 1260 - 1360 nm TE.

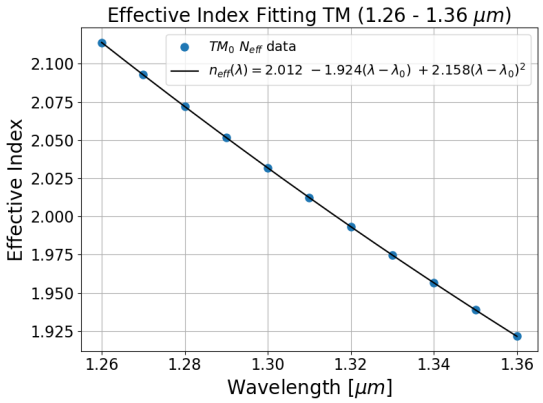

(b) 1260 - 1360 nm TM

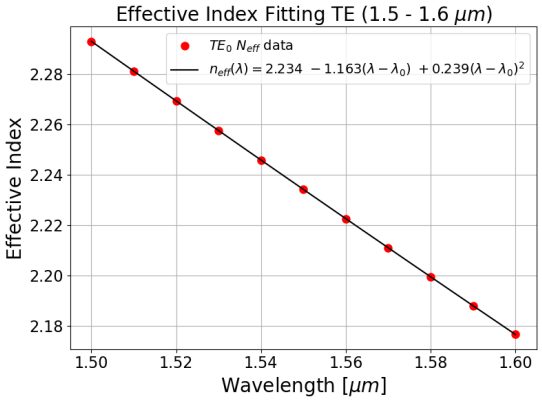

(c) 1500 - 1600 nm TE

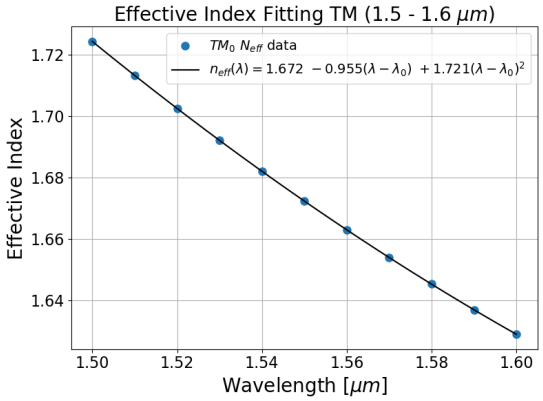

(d) 1500 -1600 nm TM

Figure 2.6: Polynomial fitting of the effective index for the TE_{00} and TM_{00} modes at $\lambda_0 = 1550$ nm and 1310 nm.

waveguide geometries, providing valuable information for the application-specific design of integrated photonic devices. The resulting colour maps of GVD, shown in Figs. 2.7a and 2.7b, provide a valuable sense of waveguide geometries with tailored dispersion properties where the increasing wavelength is generally seen to have lower dispersion values.

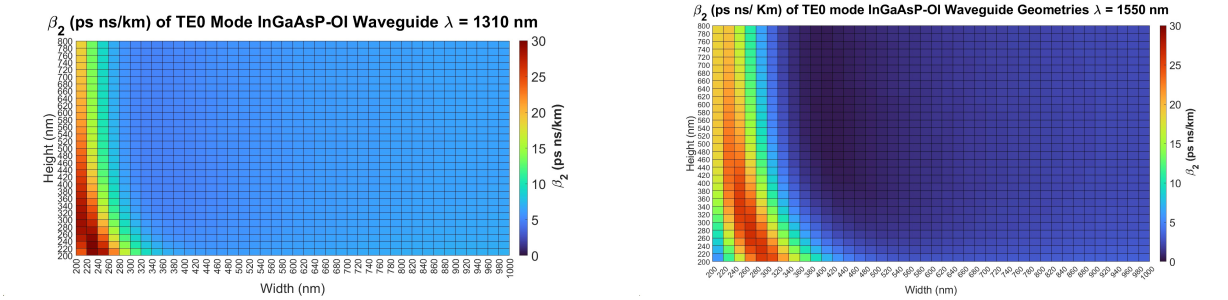

(a) 1310 nm group velocity dispersion map. Max = 29.83 ps ns/km (240 nm × 220 nm), Min = 3.84 ps ns/km (380 nm × 480 nm).

(b) 1550 nm group velocity dispersion map. Max = 26.36 ps ns/km (260 nm × 260 nm), Min = 0.39 ps ns/km (420 nm × 520 nm).

Figure 2.7: Comparison of group velocity dispersion (GVD) maps for InGaAsP-on-insulator (OI) at λ = a) 1310 nm and b) 1550 nm.

2.3 Bent Waveguides

The increasing density of photonic circuits requires low-loss components. One of the most essential components needed to enhance integrated circuit density is the 90° waveguide bend. Limiting the loss in waveguide bends maintains a good signal-to-noise ratio needed for applications in quantum photonics [146–150], biological sensing [151–154], and data and communications [21, 30, 155–157]. The loss in a waveguide bend is typically expressed in decibels per turn (dB/turn) and is attributed to two main factors: mode mismatch between the straight and bent waveguide sections, and radiation loss due to mode leakage in the waveguide bend [131]. In the bent section of the waveguide, the effective index inside is changed because of a gradient formed between the propagation constant at the inside and outside edges of the bend, causing the mode to shift towards the outside edge of the bend. The displacement creates an asymmetric field profile, contributing to mode-mismatch loss,

as well as an increased field overlap with the cladding material, thus contributing to radiation losses in the bend. At small radii, the mode profile is further displaced, and the loss in the bends increases rapidly, with the TM polarization typically experiencing greater sensitivity to the curvature radius and wavelength dependence[131, 158].

The loss of single-mode waveguides has been reported for high-index contrast material platforms such as silicon-on-insulator (SOI). For a 445 nm width and 220 nm height SOI waveguide, a bend radius of 1 μm has a reported bend-loss of 0.086 $\pm$ 0.005 dB/ turn at $\lambda = 1.5$ μm [159]. In addition to the loss characterization in circular waveguide bends, several approaches have been used to decrease the amount of loss using Euler bends for smaller bend radii [160, 161], bezier curves [162, 163], lateral offset waveguides to reduce loss by mode-matching [164], adiabatic tapered waveguide widths [161, 165], and other bends based on unique mathematical functions [166, 167]. In this section, we present the simulation results for 90° circular waveguide bends, with the waveguide cross-section dimensions of 500 nm in width and 220 nm in height, for both TE and TM modes at the wavelengths of $\lambda = 1.31$ μm and $\lambda = 1.55$ μm. For determining the loss in 90° waveguide bends, 3D FDTD simulations are performed in the OptiFDTD and Lumerical FDTD environments. The simulations in Lumerical FDTD are configured according to the methods described in [131], where an optical mode source within a straight input waveguide is connected to a circular bend of radius, R. At the output waveguide, an eigenmode expansion monitor is included to determine the power transmitted to the fundamental mode. The Eigenmode expansion monitor measures the power transferred to the fundamental mode of the waveguide, accounting for the power lost from higher-order modes that will radiate

out of the waveguide over longer distances [131]. The simulations performed in OptiFDTD are used to examine the mode transformation in waveguide bends with small radii, as illustrated in Fig. 2.8a and 2.8b.

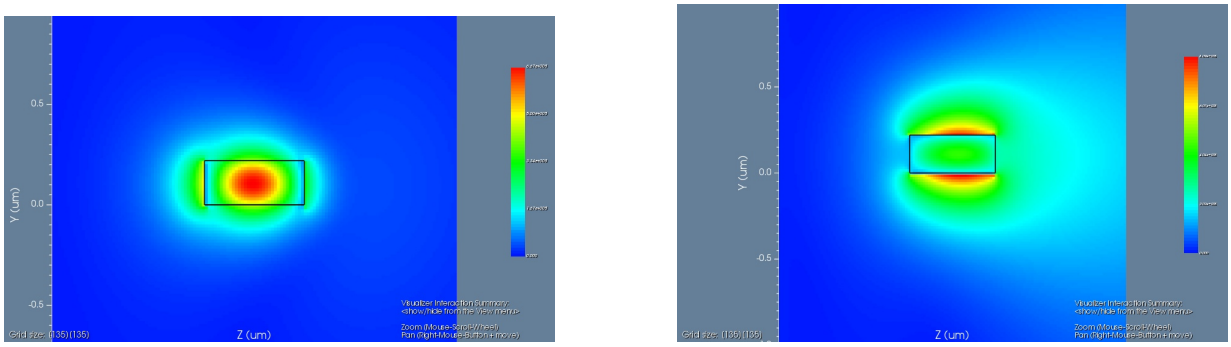

(a) TE_{00} mode in a 2 μm bend.

(b) TM_{00} mode in a 2 μm bend.

Figure 2.8: OptiFDTD simulation for the a) TE_{00} mode with E_x mode profile in a 2 μm waveguide bend. b) TM_{00} mode with E_y mode profile in a 2 μm waveguide bend, where the colour plot indicates the electric field amplitude in V/m.

As illustrated in Figs. 2.8a and 2.8b, the field profile of the TE mode is displaced to the outer edge of the waveguide and offset from the centre. Similarly, the TM mode is also offset and experiences much more displacement compared to the TE mode, with the field profile overlapping strongly with the cladding. In waveguide geometries, such as the one here, where the width is larger than the height, the TE mode is contained more by the sidewalls of the waveguide than the TM mode, and thus has a smaller field profile. [131].

90° bend radius (μm)	Loss TE (dB/turn)	Loss TM (dB/turn)
0.5	4.2788	10.5566
1	1.8428	6.3045
2	0.3264	3.8123
3	0.1069	2.5714
4	0.0473	1.7023
5	0.0346	1.2014
6	0.0231	0.8670
10	0.0083	0.3330
20	0.0086	0.0858
30	0.0089	0.0251

Table 2.2: $\lambda = 1550$nm Bend loss of the TE_{00} and TM_{00} modes in 90° bends from 0.5 μm - 30 μm.

90° bend radius (μm)	Loss TE (dB/turn)	Loss TM (dB/turn)
0.5	3.6982	7.4312
1	0.6431	2.2207
2	0.1215	0.7205
3	0.0549	0.1672
4	0.0350	0.1642
5	0.0215	0.0832
6	0.0183	0.0491
10	0.0099	0.0347
20	0.0036	0.0157
30	0.0033	0.0169

Table 2.3: $\lambda = 1310$nm total Bend loss of the TE_{00} and TM_{00} mode in 90° bends from 0.5 μm - 30 μm.

Tables 2.2 and 2.3 display that the bend loss (dB/turn) is consistently lower for the TE mode at both wavelength ranges. At small radii, this is more apparent as the TE mode has a stronger confinement and experiences less radiative losses compared to the TM mode. This aligns with the explanation provided of how the TE mode will suffer less loss than the TM mode in the waveguide bend because the field profile is more contained by the sidewalls of the waveguide core. As a result, TM waveguide bends will require larger bend radii to achieve the same performance for this waveguide geometry.

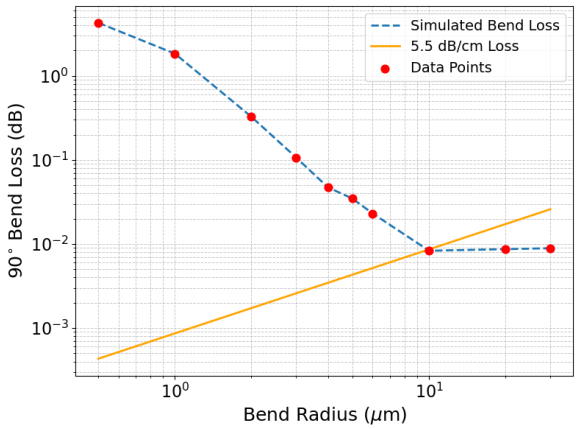

(a) TE mode at 1550 nm

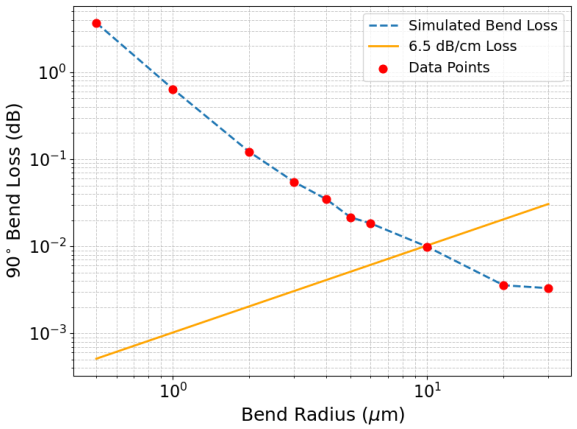

(b) TE mode at 1310 nm

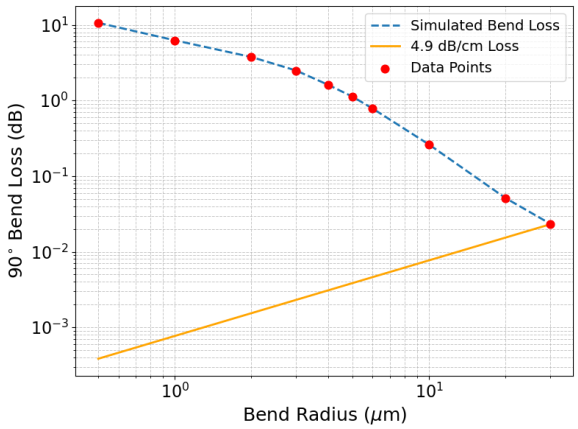

(c) TM mode at 1550 nm

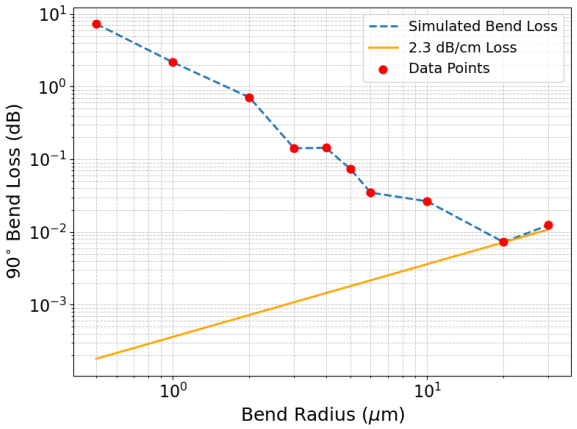

(d) TM mode at 1310 nm

Figure 2.9: Bend loss of circular waveguide bends for TE and TM polarized modes at wavelengths of 1310 nm and 1550 nm.

To determine an appropriate minimum waveguide bend radius, assumptions must be made regarding the propagation loss of straight waveguides, and a comparison drawn between the simulated values presented in Tables 2.2 and 2.3, and other high-index con-

trast material platforms. The simulated waveguide bend loss is often compared with the propagation loss for straight waveguides on the same material platform to determine the additional loss introduced by the waveguide bend. Because these data are not currently available for this particular material platform, a comparison is made with other high-index contrast material platforms such as SOI (1.2 - 2.4 dB/cm) [168, 169], AlGaAs-on-insulator (0.8 - 1.5 dB/cm) [81, 170], and notably similar InGaAsP-on-insulator ridge waveguides with an Al_2O_3 passivization layer (4 dB/cm) [171]. Based on this comparison, an upper loss limit of 5 dB/cm is used to determine an appropriate minimum circular waveguide bend radius for $\lambda = 1.55$ μm and $\lambda = 1.31$ μm. An appropriate radius will therefore have a bend loss below approximately 5 dB/cm. As illustrated in Fig. 2.9a, at 10 μm bend radius, for the TE mode at $\lambda = 1.55$ μm, the loss is 0.0083 dB/turn (5.28 dB/cm). To translate this value to dB/cm, we use the relation for the arc length and loss/turn of the waveguide bend,

$$\alpha_{dB/cm} = \frac{\alpha_{\text{bend}}}{\frac{\pi R}{2}}, \tag{2.13}$$

where α_{bend} is the loss of a single 90° bend in dB, and the arc length is $\pi R/2$. As shown in Figs. 2.9a - 2.9d, the propagation loss (orange line) intersects the waveguide bend data (red points) at the minimum bend radius close to the assumed 5 dB /cm generalization. Because the simulated TE and TM-mode loss at a radius of 10 μm slightly exceeds the 5 dB/cm limit, this value is considered an approximate design limit rather than a cutoff.

Furthermore, as illustrated in Figs. 2.9a - 2.9d, the loss experienced by the fundamental

modes in a 90° circular waveguide bend decreases as the radius of the bend increases. The loss for the TE mode is similar for wavelengths of $\lambda = 1.55$ μm and 1.31 μm due to the confinement of the TE mode to the waveguide core. In contrast, the propagation loss experienced for the TM mode at $\lambda = 1.55$ μm is greater than that experienced at 1.31 μm, due to the larger field profile that overlaps with the cladding, leading to more loss occurring in the bend.

	$\lambda = 1.55$ μm	$\lambda = 1.31$ μm
Minimum radius TE (μm)	10	10
Minimum radius TM (μm)	30	20
Loss TE (dB/cm)	5.5	6.5
Loss TM (dB/cm)	4.9	2.3

Table 2.4: Bend loss (dB/cm) for the minimum circular bend radius for TE and TM polarizations at $\lambda = 1.55$ μm and $\lambda = 1.31$ μm.

Using the upper loss limit of 5 dB/cm, from comparisons with other high-index contrast material platforms, the minimum bend radii for 90° waveguide bends are summarized in Table 2.4. The minimum radius for the TE mode at both $\lambda = 1.55$ μm and $\lambda = 1.31$ μm is 10 μm. Conversely, a much larger minimum bend radius for the TM mode is obtained at $\lambda = 1.55$ μm and $\lambda = 1.31$ μm; 30 μm and 20 μm, respectively.

Further work in this area would incorporate designs for low-loss waveguide bends, such as Euler or Bezier curves, to limit excessive mode-mismatch and radiative losses. In addition to low-loss waveguides, experimental data for the propagation loss of 500 nm x 220 nm InGaAsP-on-insulator waveguides would provide data for determining the excess loss introduced by the waveguide bends.

2.4 Linear Waveguide Tapers

A linear waveguide taper is a waveguide whose width varies linearly to match the mode size and effective index between two waveguides of different widths, as shown in Fig. 2.10.

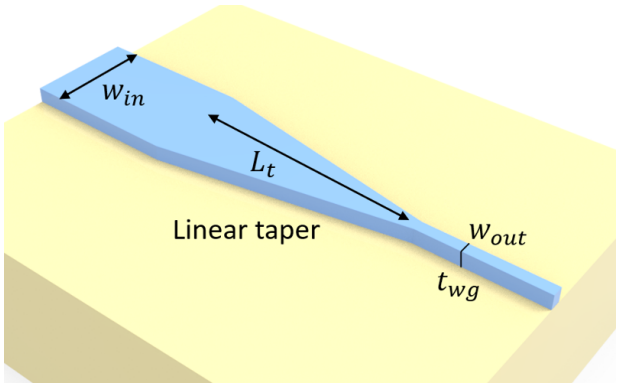

Figure 2.10: Linear taper with an input width of w_{in} and output width of w_{out} over a taper length L_t. Figure from [172].

Linear waveguide tapers are crucial for integrated photonic circuits, enabling compatibility between components of different sizes and leveraging the benefits of single-mode and multi-mode waveguides, as well as spot-size and mode conversion. It is often desired to have adiabatic transitions between waveguides, where the fundamental mode transitions without losing power to the excitation of higher-order modes, often caused by diffraction of the phase front [173], described by

$$\theta_d = \alpha \frac{\lambda}{n_{\text{eff}} \pi w_0}, \tag{2.14}$$

where α is a value close to 1 to correct for the Gaussian approximation made for light propagating in a slab region, θ_d is the divergence angle of the mode described by Gaussian beam optics, n_{eff} is the effective index of the mode at the largest width, and w_0 is the mode field radius.

Adiabatic transitions can occur in waveguide tapers when the local taper angle, θ, is less than the divergence angle θ_d,

$$\theta \ll \theta_d. \tag{2.15}$$

This condition is especially useful when transitioning from single-mode waveguides to components with wider inputs, where mode matching improves the performance of devices over a broad spectral range. Among the methods stemming from this condition, Eq. (2.15), exponential and parabolic tapers change the local taper angle, θ, as a function of length as the effective index changes along the taper for ensuring adiabatic mode evolution in compact footprints [174–177].

In this section, we present linear waveguide tapers for both TE and TM polarizations at $\lambda = 1.55$ μm and 1.31 μm transitioning between a single-mode 500 nm width, 220 nm height waveguide, to both a narrow-width 0.2 μm and a large-width 1.0 μm waveguides. In addition, a taper width of 1.54 μm is included for tapering to the geometry of a second harmonic generation waveguide discussed later in Chapter 4. The waveguide widths provided include an example of the design of waveguide tapers, which can be used as spot-size or mode converters.

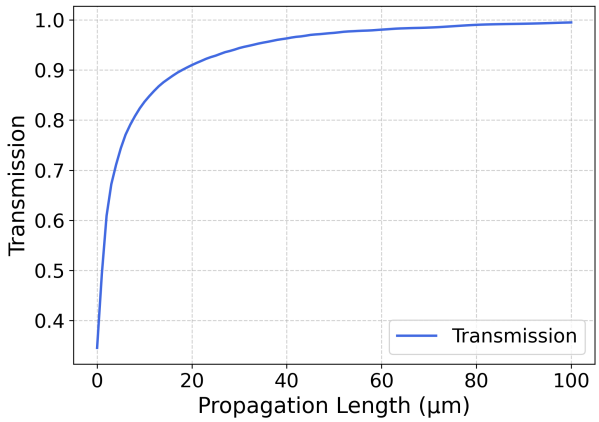

Figure 2.11: Transmission vs taper length for a linear waveguide taper with an output width of 200 nm.

Eigenmode expansion (EME) is used to determine the mode transition between the two waveguide widths, w_{in} and w_{out}. EME is a mode expansion method used for calculating the total electromagnetic fields as a sum of local eigenmodes and then propagating their amplitudes and mode overlaps between multiple cells, maintaining field continuity between segments. This method is well-suited for simulating devices with long propagation distances, such as tapers, that have bi-directional inputs. In the simulation environment, the EME simulation is divided into three groups: the input width of the linear taper, the linear transition from width 1 to width 2, and the final output width of the linear taper. Within the second group, the cell is split into 20 sections for local eigenmode simulation. Next, the number of modes to be expanded across the cells is set to 50 modes to ensure accurate field evolution. Finally, the propagation length is swept from 0 - 100 μm, as shown in Fig. 2.11.

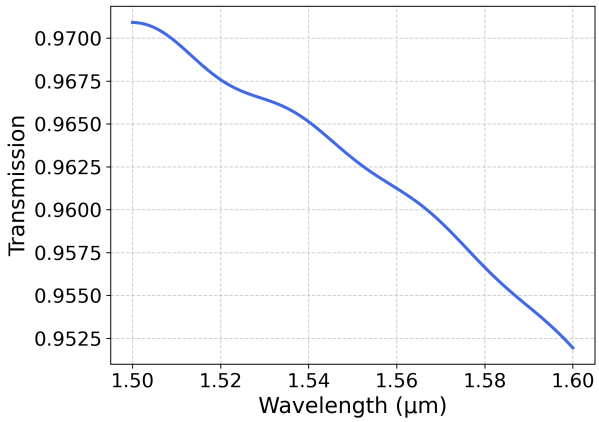

Figure 2.12: Transmission vs wavelength for a 40 μm taper length linear waveguide taper.

Once the transmission reaches a plateau, a corresponding length is then used for a wavelength sweep in the same EME simulation from 1.5 μm to 1.6 μm and 1.26 μm to 1.36 μm for both TE and TM polarization. As shown in Fig. 2.12 for a 40 μm long linear taper transitioning from a width of 500 nm to 200 nm, a high efficiency is obtained for the TE mode in the 1.5 - 1.6 μm wavelength range.

Following the same method for the other waveguide widths, the corresponding loss for each of the tapers is presented in Tables 2.5 and 2.6, with the loss being attributed to the radiation and small mode-mismatch losses.

Taper width (w_{out})	Taper length (L_t)	loss (dB) TE	loss (dB) TM
0.2	40	0.1647	0.0283
1.0	10	0.0003	0.0002
1.54	15	0.0018	0.0021

Table 2.5: loss (dB) in linear tapers at $\lambda = 1550$ nm

Taper width (w_{out})	Taper length (L_t)	loss (dB) TE	loss (dB) TM
0.2	40	0.1638	0.0036
1.0	10	0.0003	0.0004

Table 2.6: loss (dB) in linear tapers at $\lambda = 1310$ nm

2.5 Splitters

The combining and splitting of light in integrated photonic circuits is essential for taking full advantage of nonlinear and interference effects in quantum photonics [178, 179], data transmission and signal processing [180, 181], and multiplexing in optical communication systems [182]. Various methods for splitting and combining light have been explored, such as Y-branches [183–185], directional couplers [186–188], and multi-mode interferometers [189, 190]. The Y-branch is unique because it provides uniform power splitting in the two output waveguide arms across the wavelength, which is partly due to the symmetric design of the Y-branch. Various design approaches, including multi-mode tapering [191], section optimization [192], and asymmetric waveguide tapers [193], have been explored for creating low-loss Y-branches. In sections 2.4 - 2.6 in this work, splitters such as a Y-branch, directional coupler, and multi-mode Interferometer are explored for even power splitting in TE and TM polarizations for the wavelength range of $1.5 - 1.6$ μm.

2.5.1 Y-BRANCH

A Y-branch is a photonic component that evenly splits light from one input waveguide into two output waveguides, acting as a 50/50 beam splitter. In reverse, this device can also act as a combiner, where the two input waveguides are used to constructively interfere light into the fundamental mode of the output waveguide. When the Y-Branches are connected by waveguides, a Mach-Zehnder interferometer can be realized, where if one waveguide has a 180° phase shift relative to the other, destructive interference occurs. This interference occurs because, within the larger branching region, the two waveguide modes interfere to excite higher-order modes, which will then radiate out of the waveguide as the waveguide width tapers down to the single-mode output waveguide. The geometry of the Y-Branch is illustrated in Fig. 2.13.

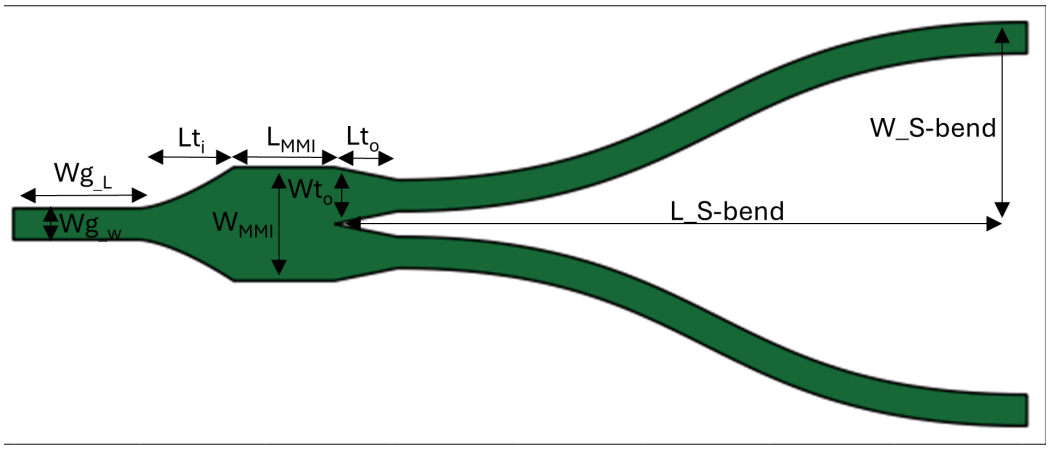

Figure 2.13: Geometrical parameters of the designed Y-branch waveguide splitter.

Considering the intensity and electric field of the light, in a Mach-Zehnder interferom-

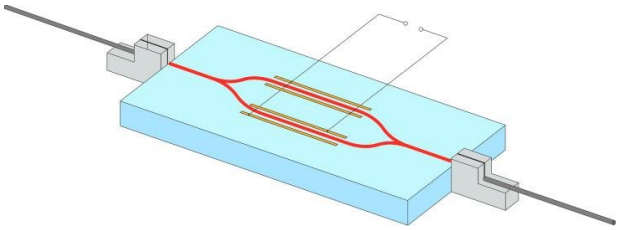

Figure 2.14: Mach Zehnder Interferometer with Y-branches used as waveguide splitter/recombination configuration. Figure from [194].

eter, the Y-Branch acts to split light with intensity $I_1 = |E_1|^2$ into two output waveguides with intensity $I_2 = I_3 = I_1/2$ ($E_2 = E_3 = E_1/\sqrt{2}$). In the two output arms, the light will propagate a distance L, with respective propagation constants $\beta_1 = \frac{2\pi n_1}{\lambda}$ and $\beta_2 = \frac{2\pi n_2}{\lambda}$. As illustrated in Fig. 2.14, the Y-branch can also be used recombine light. When the light then meets at the second Y-Branch, the corresponding electric field at the output is given as $\frac{1}{\sqrt{2}}(E_{o1} + E_{o2})$ where the electric field in each arm is represented by, $E_{o1} = E_1 e^{-i\beta_1 L_1}$, and $E_{o2} = E_2 e^{-i\beta_2 L_2}$ respectively. From the electric field at the output, the intensity in the output waveguide of the combiner is

$$I_0 = \frac{I_i}{2}\left(1 + cos(\beta_1 L_1 - \beta_2 L_2)\right). \tag{2.16}$$

This allows the Y-Branch to be a very versatile device, because a phase shift in one of the waveguide paths creates a sinusoidal variation in the intensity based on wavelength [131]. This is the principle in how Mach-Zehnder interferometers function, a fundamental device in interferometry used in applications such as quantum optics, data transmission, and optical sensing [70, 195–197].

To evaluate the optical performance of the designed Y-Branch, the mode evolution and transmission spectra of the electric field for the fundamental TE and TM modes were analyzed using 3D FDTD simulations. For simulating the Y-branch, 2D simulations were initially performed in OptiFDTD, before conducting 3D simulations in Tidy3D. The resolution of the 3D simulations was performed using 30 steps per wavelength in a non-uniform grid, with a Gaussian optical source centred at 1.55 μm within Tidy3D, providing accurate resolution compared to uniform meshing of 15 nm [198].

The mode field profiles in Figs. 2.15a and 2.15b provide insight into power transfer between the coupled waveguides and mode confinement, while the transmission spectra detail the wavelength dependence of the coupling efficiency in decibels (dB). The 50/50 splitting occurs at -3.01 dB, where the transmission in decibels is calculated from

$$\mathrm{dB} = 10\log_{10}k, \tag{2.17}$$

where k is the transmission in %.

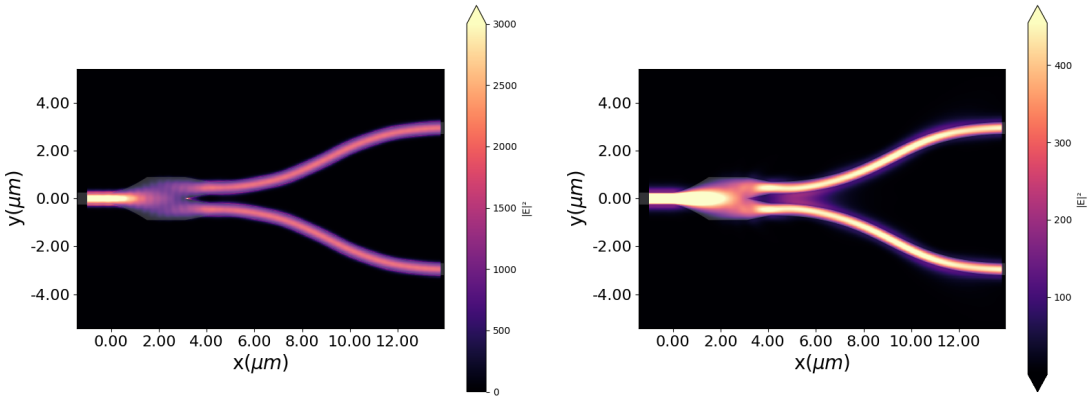

(a) TE mode evolution $\lambda = 1550$ nm. (b) TM mode evolution $\lambda = 1550$ nm.

Figure 2.15: TE_{00} and TM_{00} Mode evolution in the Y-Branch, with the electric field intensity $|E|^2$, in W/m^2.

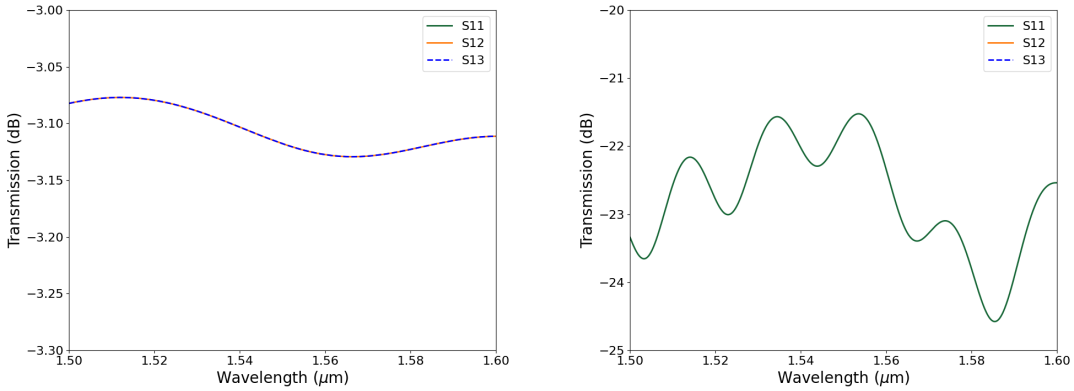

(a) −3 dB Y-Branch TE transmission. (b) −3 dB Y-Branch TE reflection.

Figure 2.16: Transmission results of $1.5 - 1.6$ μm in TE mode Y-branch

The mode evolution displayed in Figures 2.15a and 2.15b shows how the input electric field for the TE and TM modes is evenly divided into the two output arms after propagating through the branching region of the Y-branch. As illustrated in Fig. 2.16a, across the

wavelength region of $1.5 - 1.6$ μm, the TE mode shows even splitting in the two arms close to the optimal value of -3.01 dB, where the light is even split between -3.07 and -3.13 dB, and the reflected ratio at the input is very low, between -21 and -25 dB.

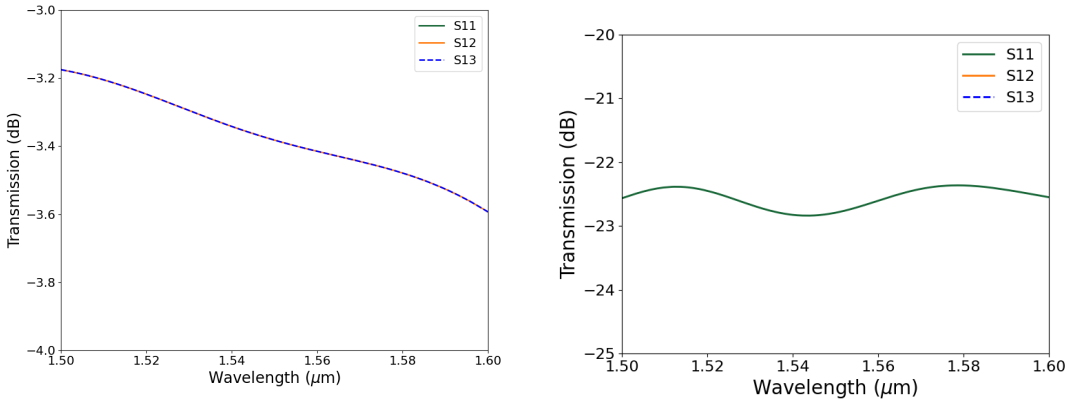

(a) -3 dB Y-Branch TM transmission. (b) -3 dB Y-Branch TM reflection

Figure 2.17: Transmission results of $1.5 - 1.6$ μm in TM mode Y-branch

For the TM mode, as shown in Fig. 2.15b, the Y-branch demonstrates higher loss, stronger wavelength dependence, and higher mode coupling in the output arms compared to the TE mode, for the same geometry. As shown in Fig. 2.17a, evaluating the performance of the TM splitting between the two arms, even splitting between the arms, shows a variation in transmission between -3.2 and -3.6 dB, and the reflections for the TM mode are also low, with reflected power being between -22 and -23 dB.

Overall, across the wavelength range $1.5 - 1.6$ μm, the Y-branch shows good performance for the TE mode and acceptable performance for the TM mode, providing polarization versatility without modifying the geometry of the component.

Parameter	dimension (μm)
input waveguide length (Wg_L)	2
input taper length (Lt_i)	1.5
MMI box length (L_{MMI})	1.6
MMI box width (W_{MMI})	1.8
linear output taper length (Lt_o)	1.0
waveguide width (Wg_w)	0.5
waveguide height	0.22
S-bend length (L˙S-bend)	10
S-bend vertical offset (W˙S-bend)	2.5

Table 2.7: Design parameters for the Y-branch splitter, including the input taper, MMI section, waveguide geometry, and S-bend layout.

The component parameters of the Y-branch are summarized in Table 2.7, and illustrated in Fig. 2.13, describing the dimensions of each region along the optical propagation path from the input to the output; The input and output waveguides have a width and height of 500 nm and 220 nm, respectively. The input taper transitions from the single-mode waveguide to the width of the multi-mode interference region (1.8 μm), through a concave parabolic taper. This transition provides an adiabatic transition to minimize reflection and excitation of higher-order modes.

From the input taper, the wider multi-mode interference region supports higher-order modes that constructively and destructively interfere to distribute the optical power into the two single-mode output waveguides. Beyond the multi-mode interference region (MMI), linear output tapers focus the light into the single-mode waveguides within the S-bends, which have a vertical offset of 2.5 μm and a horizontal length of 10 μm, laterally separated to prevent excessive unwanted mode coupling between the two waveguides.

The Y-branch designed in this section provides a useful component for the splitting and recombination of light that can be used in integrated photonic devices such as Mach-Zehnder interferometers. Further work in the development of the component can be done for designing parameters for a target wavelength of 1.31 μm in the O-band (1.26 $-$ 1.36 μm), as well as incorporating fabrication-aware design algorithms for small spacings, such as the junction of the linear tapers. In the following sections, other devices such as 2×2 directional couplers and multi-mode interferometers for splitting and combining light are also discussed.

2.5.2 2 × 2 Multi-Mode Interferometer

A multi-mode interferometer (MMI) is a component used for splitting and combining light predictably. In contrast to Y-branches and directional couplers, MMIs function based on the multimode interference and self-imaging in a broad waveguide region that supports multiple guided modes. The first developments of MMIs for integrated circuits were demonstrated for single and double self-imaging interference in multi-mode waveguides [199]. The operating principle of an MMI is based on the self-imaging principle, where a monochromatic plane wave incident on a periodic diffraction grating repeats its own image at a fixed distance away [200, 201]. In self-imaging, the guided modes supported by the multimode waveguide interfere constructively to reproduce replicas of the input mode field at well-defined self-imaging lengths. Applied to MMIs, the input electric field will repeat its own self-image at the beat length L_π [202],

$$L_\pi(\lambda) = \frac{\pi}{\beta_1 - \beta_2}, \tag{2.18}$$

where L_π represents an approximate beat length for multimode interference in high-index contrast waveguides and β_i is the respective propagation constant for the two lowest order modes. The guided modes are supported in the broad waveguide with different propagation constants, β, and their relative phase accumulation produces periodic interference patterns along the propagation direction. This is used to determine the approximate MMI length

for N self-images to form, given by $L_{MMI} = L_\pi/N$,

$$L_{MMI} = \frac{4n(\lambda)W_{MMI}^2}{N\lambda}. \tag{2.19}$$

Here, $n(\lambda)$ is the effective refractive index of the multi-mode waveguide region, W_{MMI} is the width of the multi-mode region, and N is the number of self-images produced. The interference images produced in MMIs make them versatile components for photonic circuits in applications such as optical communications [203, 204], sensing [205, 206], and signal routing [207]. In this section, we present a 2 × 2 InGaAsP-on-insulator MMI, illustrated in Fig 2.18, designed for 50/50 power splitting of the TE_{00} mode within the wavelength range of $\lambda = 1.5 - 1.6$ μm.

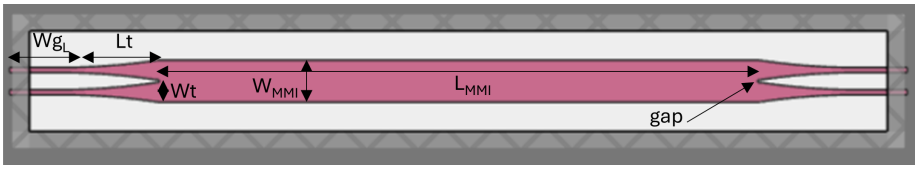

Figure 2.18: 2 × 2 MMI diagram

To design the MMI, the width, W_{MMI}, is set large enough to support higher-order mode propagation, described by a V number,

$$V = \frac{W_e\pi}{\lambda}\sqrt{n_r^2 - n_c^2} \gg 1, \tag{2.20}$$

where λ is the wavelength, n_r is the refractive index of the InGaAsP core, and n_c is the refractive index of the cladding, SiO_2. Since the InGaAsP-on-insulator platform is a high-

index contrast waveguide, the physical width of the waveguide is used as the effective width, $W_e \approx W$, ignoring the Goos-Hänchen shift associated with lateral mode field penetration at the ridge boundaries of the material [208, 209]. This approximation is valid for high-contrast waveguides and simplifies the estimation of the number of supported modes in the multimode waveguide as:

$$V = \frac{4.2\pi}{1.55}\sqrt{3.277^2 - 1.44^2} = 25.05. \tag{2.21}$$

Following Eq. (2.19), the required MMI length, L_{MMI}, for a specified number of self-images depends on the width of the MMI, W_{MMI}, the effective index in the multimode region, n_r, and the number of output images N [201, 202, 208, 209].

For the designed 2 × 2 MMI, with a specified length, L_{MMI}, the calculated parameters are as follows: the effective indices of the two lowest-order guided modes in the multi-mode region at $\lambda = 1.55$ μm are $n_{TE_{00}} = 2.6377$ and $n_{TE_{01}} = 2.6165$. The width of the MMI is 4.2 μm, and the number of self-images needed at the output is N = 2. Using these parameters, the calculated imaging length is $L_{MMI} = 60$ μm based on Eq (2.19).

Parameter	dimension (μm)
taper lengths (Lt)	10.0
taper widths (Wt)	2.0
gap	0.2
MMI box length (L_{MMI})	60
MMI box width (W_{MMI})	4.2
Waveguide lengths (Wg_L)	5.0
waveguide width	0.5
waveguide height	0.22

Table 2.8: 2×2 MMI geometry parameters

To reduce mode mismatch between the single-mode input and output waveguides and the multi-mode interference region, as listed in Table 2.8, linear tapers with a length of 10 μm and a width of 2.0 μm are added. These tapers adiabatically transform the mode from the single-mode waveguide to better match the field distribution in the multimode region, thus reducing excess mode-mismatch and insertion loss at the junction of the MMI and waveguides. The effective index of the 2.0 μm taper is $n_r = 2.616490$, and that of the TE_{01} mode with two self-images in the MMI is $n_r = 2.618590$, leading to a relative mismatch of approximately 0.08%. Similar methods have been introduced in other MMI designs to reduce mode mismatch and improve broadband performance [202].

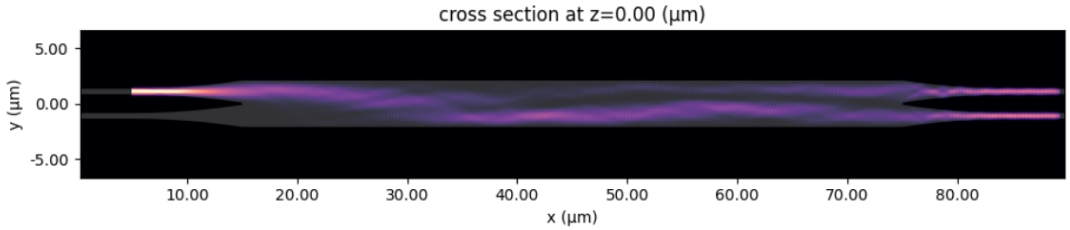

Figure 2.19: TE_{00} mode evolution in a 2 $\times$ 2 MMI, with the electric field intensity $|E|^2$, in W/m^2.

The mode evolution of the 2 $\times$ 2 MMI is illustrated in Fig. 2.19. Light injected from the left propagates through the input taper, where the mode expands to match the multimode region. Within the multimode region, constructive interference produces self-images of the input field at the designed length L_{MMI}. The self-images are collected by two output tapers of width 2 μm, separated by a 0.2 μm gap, resulting in near-equal power splitting between the two output arms. This behaviour is confirmed by the transmission spectra shown in Fig. 2.20.

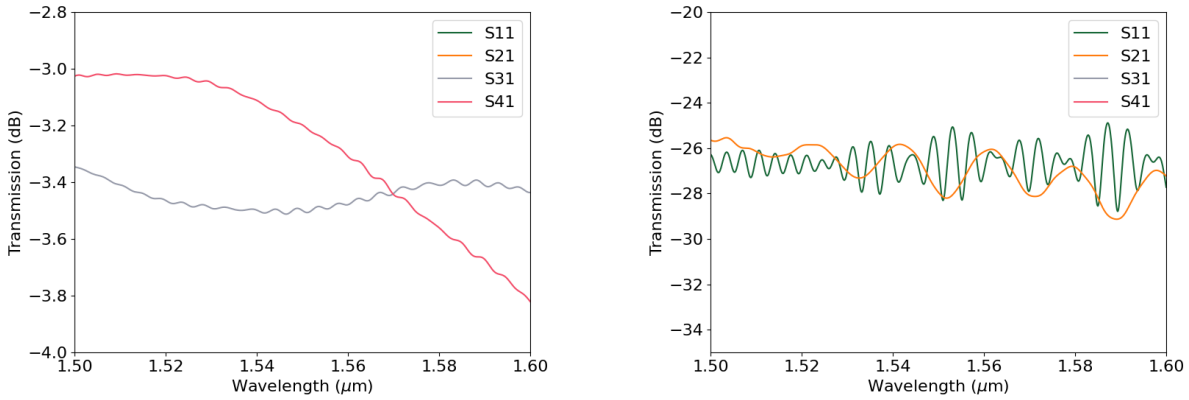

(a) Transmission S-parameters (S_{31} and S_{41}). (b) Reflection S-parameters (S_{11} and S_{21}).

Figure 2.20: Simulated transmission and reflection S-parameters for the 2 × 2 MMI coupler.

As illustrated in Fig. 2.20, the S_{41} parameter, relating to the transmission in the lower output arm of the 2 × 2 MMI, demonstrates power splitting with a transmission range between −3 dB and −3.8 dB (41 - 50 %) nearing an optimal value of −3.01 dB at 1.5 μm. While the S_{31} parameter demonstrates splitting within −3.4 and −3.6 dB (43 -45%) over the 1.5 - 1.6 μm wavelength range. This results in a small power imbalance in the output amplitudes across the wavelength range $\lambda = 1.5 - 1.6$ μm; however, the performance is acceptable for near −3 dB splitting applications. The MMI can therefore be used for splitting and combining light from single or dual inputs, providing near-even splitting and easy fabrication with the parameters outlined in Table 2.8. Future optimizations of the MMI length, width, and taper geometry could be employed to improve balance across the wavelength range of interest, while future designs of the MMI will benefit from designs for TM polarization in the wavelength range of $1.26 - 1.36$ μm.

2.5.3 2 × 2 Directional Coupler

A 2 × 2 directional coupler is a photonic component with two input and output ports used to split or combine light in two closely spaced waveguides. Directional couplers are seen in a variety of applications, including state manipulation in quantum photonics [210, 211] and tunable multiplexing in signal processing [212]. In a 2 × 2 directional coupler, the optical power between two closely spaced waveguides is split between the two arms via evanescent wave coupling. This coupling is wavelength dependent and is important for enabling interference effects and power splitting in multiplexing and de-multiplexing applications [213]. The behaviour of the 2 × 2 directional coupler is described in more detail in [131], and a summary of the behaviour of the directional coupler will be included in this section for the InGaAsP-on-Insulator platform. In this section, as illustrated in Fig. 2.21, we present a 2 × 2 directional coupler designed for 50/50 power splitting of the TE_{00} mode at $\lambda = 1.55$ μm, which can be used for more intricate circuits such as Mach-Zehnder interferometers.

In the 2 × 2 directional coupler, power is transferred between two closely spaced waveguides and exits the device through either the through port or the cross port, which are characterized by the field transmission coefficient t and the field coupling coefficient κ, respectively. The corresponding power fractions are given by $|t^2|$ and $|\kappa^2|$. The power transmission in the waveguides can therefore be described by the relations:

$$\kappa^2 = \frac{P_{cross}}{P0} = \sin^2(C * L), \tag{2.22}$$

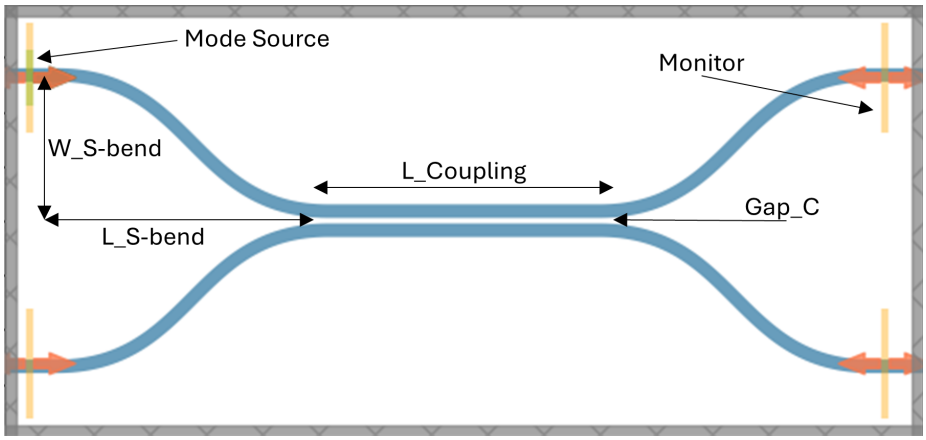

Figure 2.21: Geometrical parameters of the 2 × 2 directional coupler.

$$t^2 = \frac{P_{through}}{P_0} = \cos^2(C * L). \tag{2.23}$$

These power fractions in each waveguide will vary sinusoidally depending on the coupling coefficient, C, and the interaction length, L, over which the two evanescent waves couple. The coupling strength is determined using

$$C = \frac{\pi \Delta n}{\lambda}. \tag{2.24}$$

Here, $\Delta n = n_+ - n_-$, is the effective index difference between the two lowest-order even, n_+, and odd, n_-, modes present in the waveguides for a fixed coupling gap. In addition to Δn, the coupling gap, g, is also important for determining the coupling strength, described by the exponential function

$$C(g) = B * e^{-A*g}, \tag{2.25}$$

where g is the gap between the waveguides, and A and B are constants dependent on

factors such as the geometry of the waveguides and the operational wavelength. These constants are extracted by fitting simulated coupling data to Eq. (2.25).

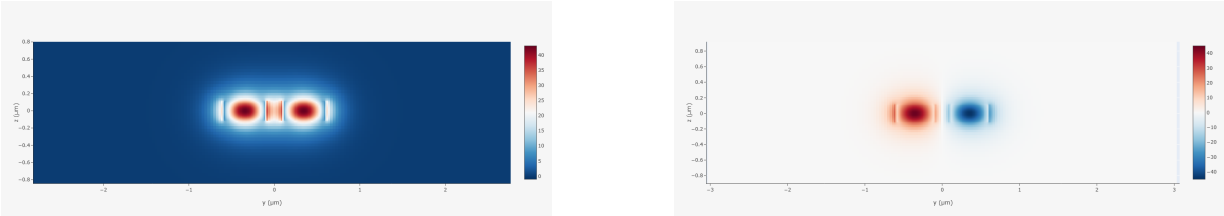

(a) TE real $\vec{E}_y$ - symmetric modes

(b) TE real $\vec{E}_y$ - anti-symmetric modes

Figure 2.22: Magnitude of the electric field of the fundamental TE_{00} modes of a directional coupler, measured in the units of V/m. The plot shows (a) a symmetric and (b) an anti-symmetric hybrid modes.

To determine the coupling coefficient C, the effective indices for the symmetric and anti-symmetric modes must be obtained for the respective polarization. The high index contrast of the InGaAsP-on-Insulator platform allows for strong coupling between the waveguides due to the index difference of the symmetric and anti-symmetric modes present in the coupling region, whose modes are illustrated in Figs. 2.22a and 2.22b.

Following the symmetric and anti-symmetric mode profiles in Figs. 2.22a and 2.22b, respectively, the effective index data for each mode are illustrated in Fig. 2.23. The effective index data for the even and odd modes present in the coupling region with a gap of 0.2 μm provide a nearly constant refractive index difference Δn. The nearly constant separation between these curves indicates that Δn varies weakly over the wavelength range of interest, enabling predictable coupling behaviour.

The coupling dynamics of the directional coupler are governed by the cross-over length

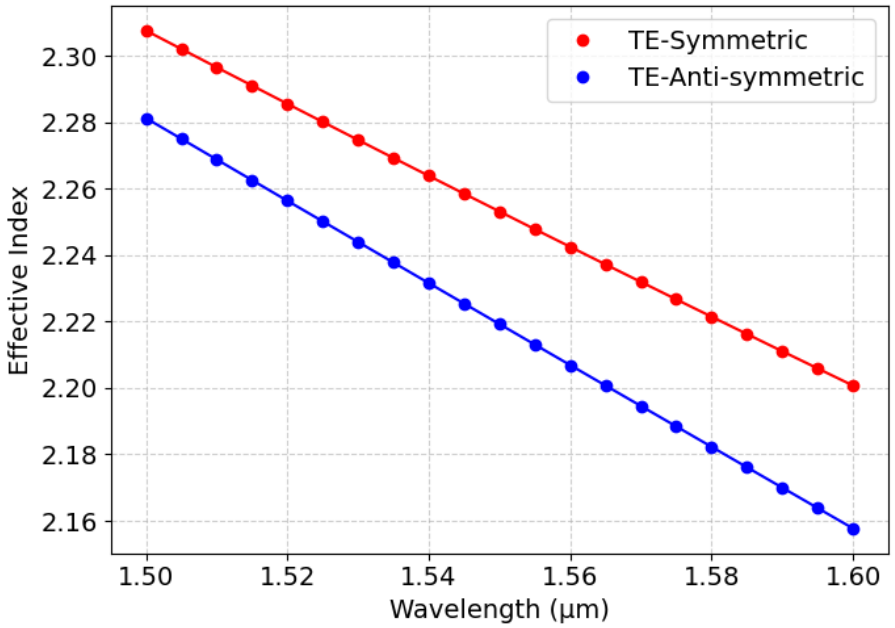

Figure 2.23: Polynomial fit to the effective indices of the even and odd TE modes in the coupling region for a minimum gap of $g_{\min} = 0.2$ μm over the wavelength range 1.5–1.6 μm.

(beat length), L_c, which corresponds to the propagation distance at which complete power transfer to the cross port occurs in an ideal, symmetric, and lossless coupler. This length is given by

$$L_c = \frac{\lambda}{2\Delta n}, \tag{2.26}$$

where complete power transfer to the cross port occurs in an ideal symmetric lossless coupler. This is achieved when the accumulated relative phase in the even and odd modes,

with propagation constants β_1 and β_2, equals π,

$$\beta_1 L_c - \beta_2 L_c = \pi. \tag{2.27}$$

Under this condition, the argument of the sine function in Eq. (2.22) becomes $\pi/2$, yielding complete power transfer to the cross waveguide port:

$$\kappa^2 = sin^2\left(\frac{\pi}{2}\right) = 1. \tag{2.28}$$

Incorporating the $\frac{\pi}{2}$ phase shift into the phase relationship between the two waveguides, the transmission for the through and cross ports can be written more generally as a function of the propagation distance, z, and the cross-over length, L_c

$$\kappa = \sqrt{\frac{P_{cross}}{P_0}} = \left|\sin\left(\frac{\pi\Delta n}{\lambda}L_c\right)\right| = \left|\sin\left(\frac{\pi}{2}\frac{z}{L_c}\right)\right|, \tag{2.29}$$

$$t = \sqrt{\frac{P_{through}}{P_0}} = \left|\cos\left(\frac{\pi\Delta n}{\lambda}L_c\right)\right| = \left|\cos\left(\frac{\pi}{2}\frac{z}{L_c}\right)\right| \tag{2.30}$$

Here, within the sin and cos arguments, 100% power coupling to the opposing waveguide occurs when $\sin\left(\frac{\pi\Delta n}{\lambda}L_c\right) = 1$, this happens when $\left(\frac{\pi\Delta n}{\lambda}L_c\right) = \frac{\pi}{2}$. This normalizes the expression in terms of the power coupled as a function of the cross-over length L_c. These expressions normalize the coupling behaviour in terms of the cross-over length, L_c, providing a convenient framework for determining the required coupling length, z, for a desired splitting ratio.

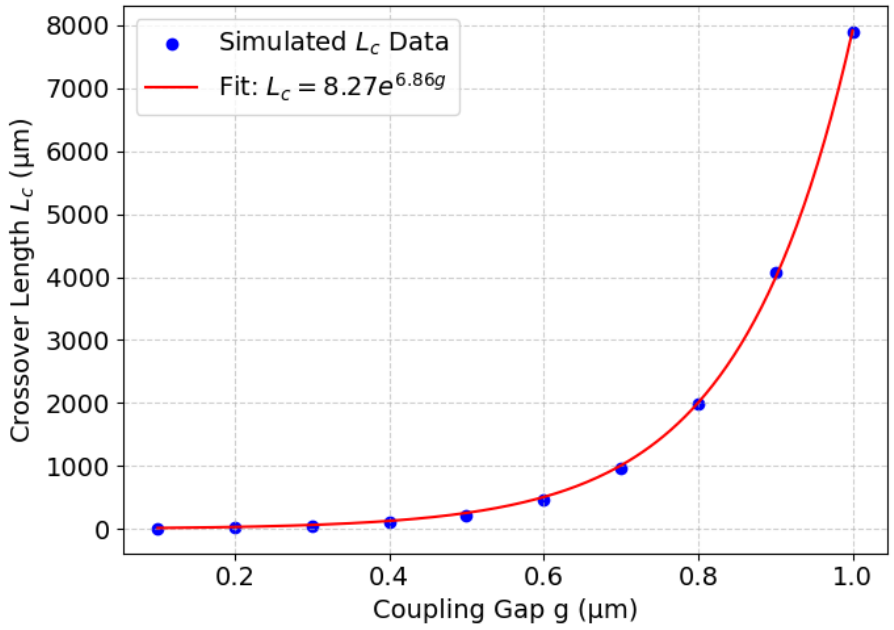

Figure 2.24: Exponential fit of the cross-over length L_c as a function of coupling gap for the TE_0 mode at $\lambda = 1.55$ μm.

As shown in Fig. 2.24, the cross-over length increases exponentially as the coupling gap is increased from 0.1 to 1.0 μm. This trend reflects the rapid decay of evanescent field overlap with increasing separation. Fitting the data using Eq. 2.25 yields the coefficients A = 6.86 and B = 8.27, which are used to model the coupling strength as a function of the gap size.

Coupling Gap (μm)	Cross over length L_c (μm)
0.1	9.947
0.2	22.858
0.3	49.336
0.4	104.829
0.5	220.943
0.6	462.905
0.7	964.539
0.8	1996.601
0.9	4067.926
1.0	7882.944

Table 2.9: Cross over lengths, L_c, for the TE_{00} mode in a 50/50 2 $\times$ 2 directional coupler at $\lambda = 1.55$ μm.

Analyzing the cross-over lengths, L_c, for the different coupling gaps based on Eq. (2.27) provides the cross-over lengths listed in Table 2.9.

Parameter	dimension (μm)
S-bend length (L_S-bend)	10.0
S-bend offset (W_S-bend)	5.0
Coupling length (L_Coupling)	10.0
Coupling gap (Gap_C)	0.2
Waveguide width	0.5
Waveguide height	0.22

Table 2.10: Geometrical parameters for the 2 $\times$ 2 directional coupler, including the coupling region and S-bend sections.

Because practical directional couplers include bends leading both into and out of the coupling region, it is also important to calculate the extra effective length, L_{eff}, introduced by the waveguide S-bends that lead into the coupling region in the 2 $\times$ 2 directional coupler to achieve the target splitting ratio. To account for the effective length of the waveguide

S-bends, the shape of the bend must be taken into consideration to model the gap between the two waveguides. For this bend, the shape is described by a cosine function,

$$g(z) = g_{\min} + \Delta y * \left(1 - \cos\left(\frac{\pi z}{L_b}\right)\right), \tag{2.31}$$

where $g_{min} = 0.2$ μm is the minimum coupling gap, Δy is the lateral offset of the S-bend ($\Delta y = 5.0$ μm), and L_b is the length of the S-bend ($L_b = 10$ μm). The parameters describing the rest of the dimensions of the 2 $\times$ 2 directional coupler are listed in Table 2.10. This function can then be integrated over the length of the S-bend to determine L_{eff}, and to find the effective length of one bend, we can integrate the normalized coupling strength as a function of z to obtain z_{bend}, the effective length of one S-bend section,

$$z_{bend} = \int_0^{L_b} \frac{C(z)}{C(g_{min})}\, dz. \tag{2.32}$$

Following this integration, the effective length of the S-bend, z_{bend}, can be found as

$$z_{bend} = \int_0^{L_b} e^{-A*g(z)-c}. \tag{2.33}$$

From this approach, evaluating Eq. (2.33) gives an effective coupling length of $z_{bend} = 0.684$ μm for a single S-bend section. Taking into account the two sections of the S-bend that lead into and out of the coupling region, the two S-bends contribute $2z_{bend} = 1.367$ μm to the coupling length of the 2 $\times$ 2 directional coupler.

Using Eq. (2.26) and the effective index data for the even and odd modes, illustrated

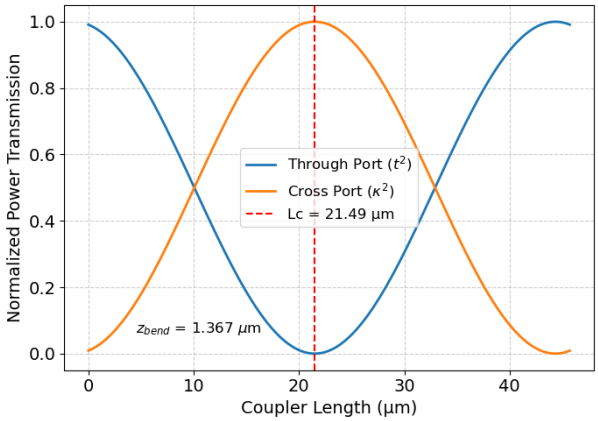

Figure 2.25: Analytical transmission of the through and cross ports as a function of coupling length for the TE polarization at $\lambda = 1.55$ μm, including the effective additional coupling length introduced by the S-bends.

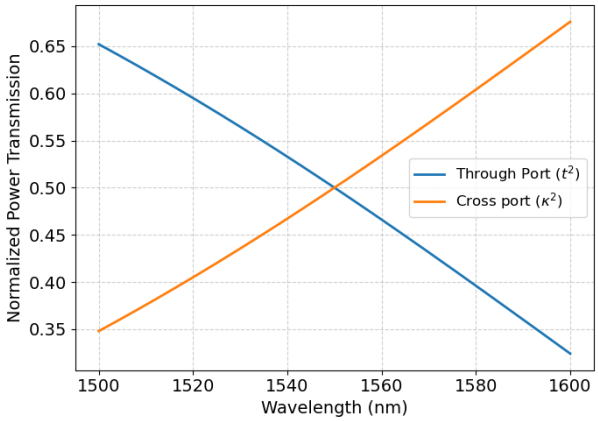

Figure 2.26: Analytical transmission of the through and cross ports as a function of wavelength for a coupling length of 10 μm, showing the wavelength dependence of the coupling strength around the 50/50 splitting condition.

in Fig. 2.23, the cross-over length for a coupling region with a 0.2 μm gap is calculated to be 22.85 μm at $\lambda = 1.55$ μm, and for a 50/50 power splitting ratio, the required coupling length is 11.43 μm. Subtracting the effective coupling length introduced by the input and output S-bends, $2z_{\text{bend}} = 1.367$ μm, yields a straight coupling region of L = 10.06 μm used in the final design, as illustrated by the transmission and coupling length in Fig. 2.25, as well as the calculated transmission vs wavelength in Fig. 2.26.

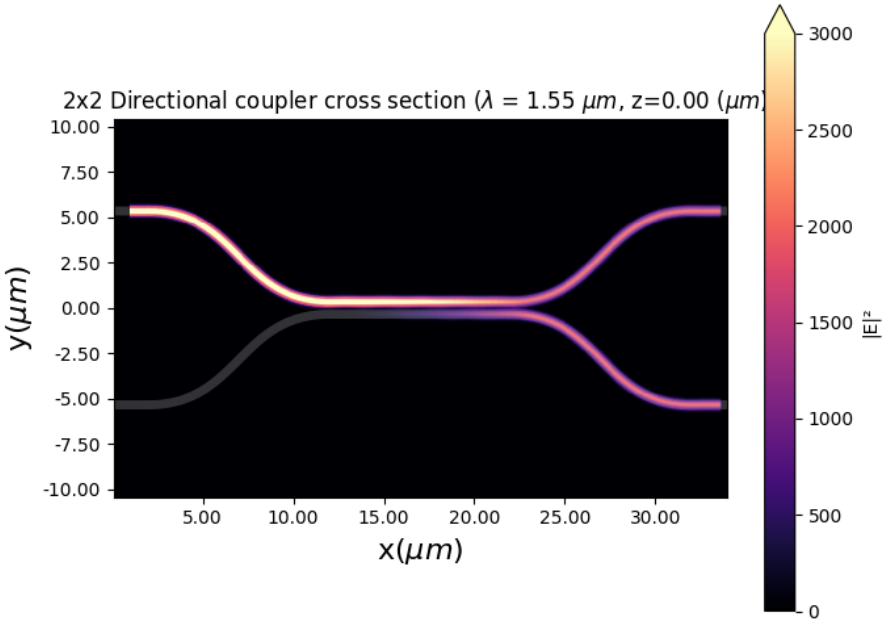

Figure 2.27: Electric-field intensity in units of W/m^2, illustrating mode evolution in the 2 × 2 directional coupler at $\lambda = 1.55$ μm.

To validate the analytical calculations, 2D simulations were performed in OptiFDTD, followed by 3D FDTD simulations in Tidy3D. The TE_0 mode was evaluated for -3 dB splitting at $\lambda = 1.55$ μm. The 3D FDTD simulation region was defined as 33 μm x 15 μm x 4.4 μm, with PML boundary conditions with 12 layers, and the structure is extended beyond the PML boundaries to reduce back reflections into the simulation region and prevent diverging results. The resolution of the simulation was performed at 30 steps per wavelength to maintain high accuracy close to that of a uniform mesh of 15 nm. As illustrated in Fig. 2.27, power launched into the input waveguide transfers progressively to the adjacent waveguide along the coupling region, demonstrating evanescent coupling and 50% power exchange for a 10 μm coupling length at $\lambda = 1.55$ μm.

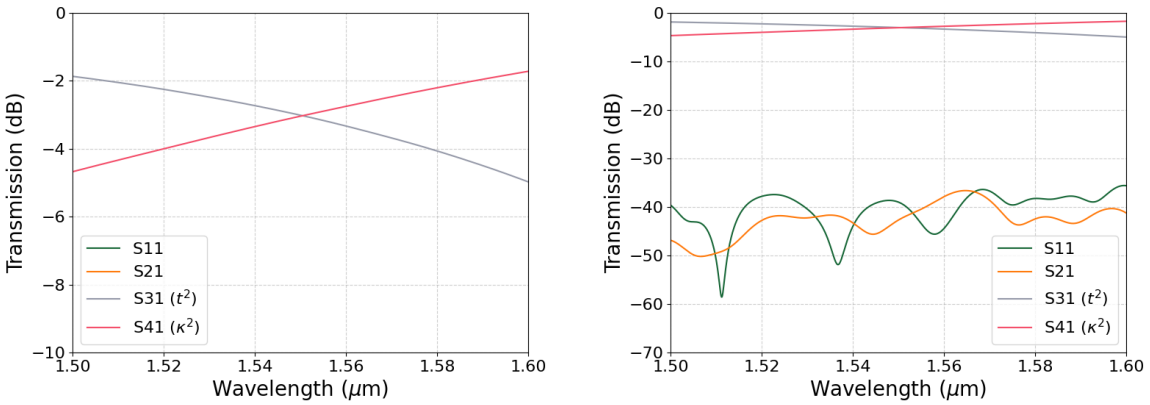

(a) through and cross transmission

(b) Transmission vs wavelength

Figure 2.28: Simulated transmission spectra of the 2 × 2 directional coupler for the TE_{00} mode. (a) Log-scale view highlighting the near -3 dB splitting between through and cross ports. (b) Log-scale view showing low crosstalk and suppression of unwanted transmission outside the coupling band.

As illustrated in Fig. 2.28b, the transmission spectrum in the wavelength range of

$1.5 - 1.6$ μm shows a -3 dB split at 1.55 μm, matching the calculation of Eqs. (2.29) and (2.25). The wavelength dependence observed in the analytical model closely matches the 3D FDTD results, showing an expected linear wavelength dependence of the coupling strength. The results of the 3D FDTD transmission spectrum match those of the calculated wavelength dependence in Figs. 2.25 and 2.26, demonstrating the validity of analytical expressions in predicting the performance of the directional coupler. In addition, the 3D FDTD results in Fig. 2.28b show very low reflection and cross-talk across the -40 to -60 dB range for the S_{11} and S_{21} S-parameters, respectively.

The 2×2 directional coupler presented here serves as an important component needed to split and combine light in photonic circuits. Excellent agreement is observed between analytical predictions and full FDTD simulations when accounting for extra wave coupling introduced by waveguide bends, consistent with the methods described in [131]. Further improvements may be achieved through designs for uniform broadband splitting, using methods such as phase control and asymmetric waveguides [187], and subwavelength materials [188, 214, 215]. The demonstrated approach provides a robust framework for designing directional couplers with different splitting ratios. Such couplers, when cascaded, can be implemented in wavelength division multiplexing systems for signal processing [196].

2.6 Waveguide X-crossing

A waveguide X-crossing is a type of photonic component that allows for multiple optical waveguides to intersect with minimal signal loss and minimal crosstalk between channels. This component is essential for the routing of waveguides in photonic circuits, particularly when chip design space is limited. An ideal waveguide x-crossing allows two waveguides to intersect at a 90° angle while preventing optical power from coupling into the orthogonal waveguide path, thus minimizing crosstalk. Low crosstalk between channels is important for maintaining signal integrity, and especially important for dense routing, data transmission, and optical interconnects [216, 217].

The design of the X-crossing presented in this section uses beam shaping of two single-mode waveguides, and an intersection region based on a shape-optimized back-to-back parabolic tapers similar to cosine-based curves demonstrated in [218]. In this approach, the guided mode is gradually expanded and then refocused across the intersection region, reducing scattering and radiative loss, and suppressing coupling into the orthogonal waveguides. By shaping the optical field to be focused at the centre of the crossing, the mode is reproduced at the output waveguide with minimized loss. The controlled expansion over the distance Lt_1 and focusing over the distance Lt_2 in Fig. 2.29, forms a lens-like beam-shaping region that reduces beam divergence across the intersection region, increases the mode size, and tailors the beam waist to maximize overlap with the output waveguide mode.

Other approaches for designing compact waveguide crossings include: fish eye lenses [219], MMI-based crossings [220], optimized-angle crossings [221], and subwavelength grating crossings [222]. While some of these designs achieve extremely low loss or crosstalk, they often require larger footprints or increased complexity in fabrication. Beam-shaping crossings maintain a relatively simple geometry for fabrication and offer excellent transmission, low crosstalk, and a compact footprint for dense photonic integration. In this section, a compact waveguide X-crossing using beam shaping is designed with cosine tapers, achieving a compact footprint of approximately 10 μm x 10 μm, as described by the geometrical parameters listed in Table 2.11 and illustrated in Fig. 2.29. This footprint and design approach are comparable to newer beam-shaped crossings discussed in [218].

X-crossing Parameter	dimension (μm)
parabolic taper length 1 (Lt_1)	2.0
parabolic taper width 1 (Wt_1)	1.4
parabolic taper length 2 (Lt_2)	0.7
parabolic taper width 2 (Wt_2)	1.0
intersection width (Wt_2)	1.0
intersection length (Lt_3)	1.0
waveguide width (Wg_{w1})	0.5
waveguide length (Wg_L)	2
Waveguide height	0.22

Table 2.11: Geometrical parameters of the waveguide X-crossing.

To evaluate the performance of the X-crossing design, 2D simulations were performed in OptiFDTD, and 3D FDTD simulations were performed in Tidy3D. For the simulation, a Gaussian excitation source is centred at 193.4 THz with a bandwidth spanning $1.5-1.6$ μm ($\approx$ 12.6 THz). PML boundary conditions with 12 PML layers are used on all boundaries,

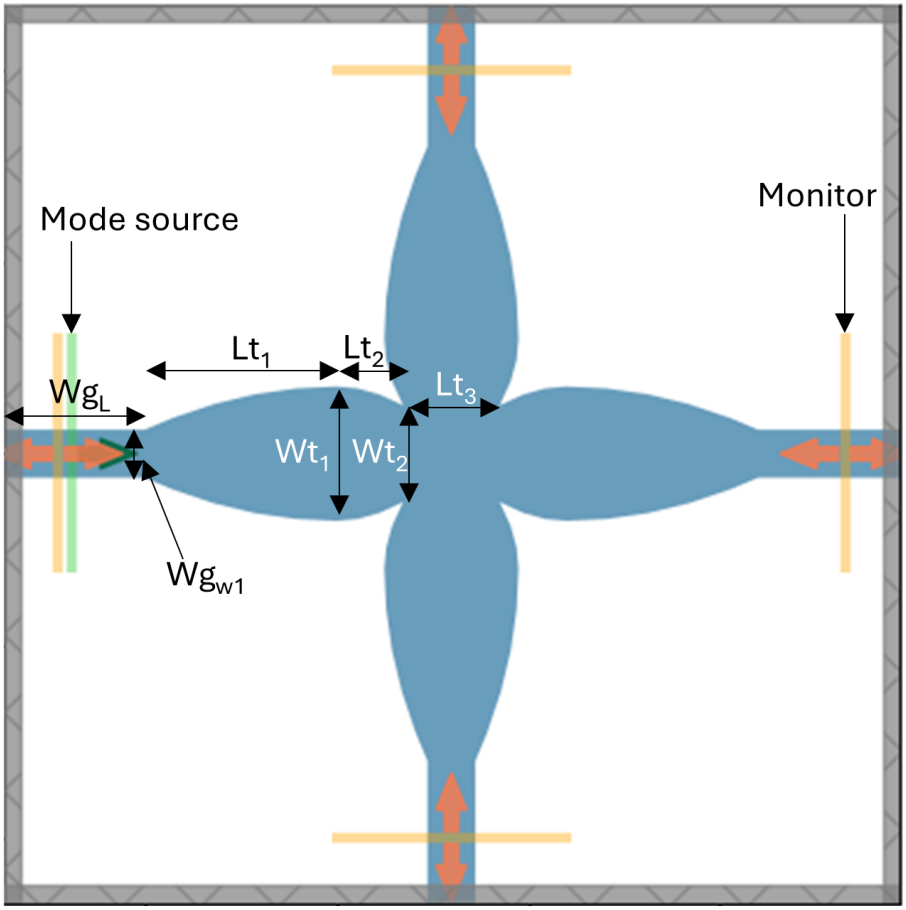

Figure 2.29: X-crossing parameters.

and the simulation uses a uniform resolution of 15 nm, providing sufficient accuracy over the wavelength range of interest. The simulation domain has a size of 9 μm x 9 μm x 4.22 μm, ensuring a 2 μm cladding above and below the 220 nm InGaAsP core layer and allowing the structure to extend partially into the PML regions, suppressing back reflections.

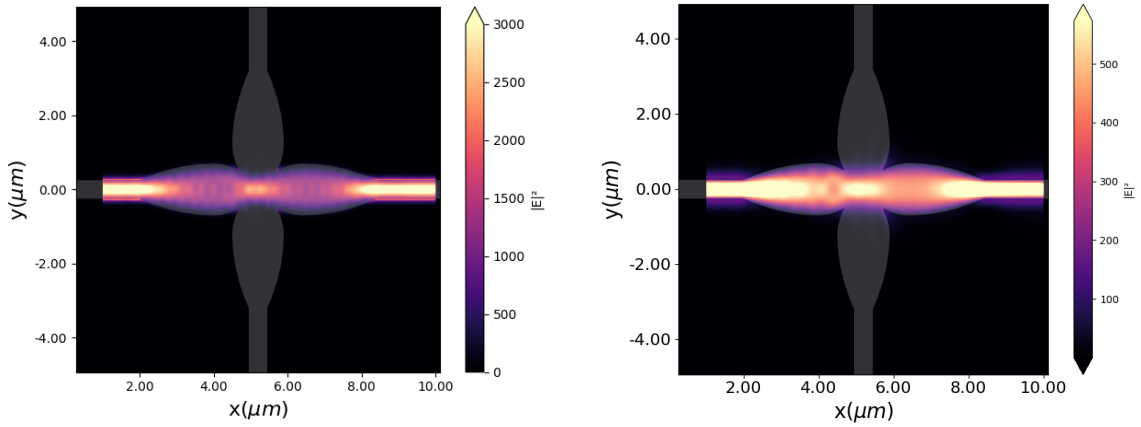

(a) $\lambda = 1550$ nm TE. (b) $\lambda = 1550$ nm TM.

Figure 2.30: Electric field intensity in units of W/m^2, at $\lambda = 1.55$ μm in the waveguide X-crossing for the a) TE_{00} mode, b) TM_{00} mode.

The mode evolution of the waveguide x-crossing for both TE and TM polarizations at $\lambda = 1.55$ μm is shown in Figs. 2.30a and 2.30b. The light is launched from the left input waveguide and propagates into the larger cosine taper, where the mode gradually expands to the maximum width of 1.4 μm over a length of 2 μm. The taper then narrows to a minimum width of 1.0 μm over an additional 0.7 μm, focusing the mode into the 1.0 μm x 1.0 μm intersection region. After propagating through the crossing, due to the symmetrical geometry of the x-crossing, the mode is then refocused into the output waveguide.

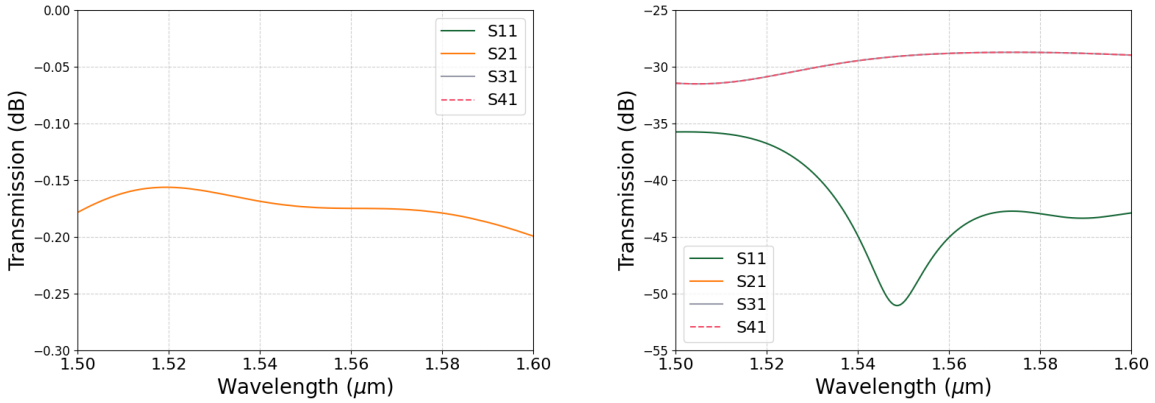

(a) S_{21} TE x-crossing transmission.

(b) S_{31} and S_{41} TE x-crossing transmission.

Figure 2.31: Simulated transmission spectra of the x-crossing at $\lambda = 1.55$ μm for the (a) S_{21} transmission with TE polarization, showing a -0.3 dB bandwidth region, and (b) S_{31} crosstalk and S_{41} reflection transmission response down to -50 dB.

As illustrated in Fig. 2.31a, the S_{21} transmission for the TE mode at $\lambda = 1.5 - 1.6$ μm exhibits low loss with values between -0.15 and -0.2 dB and approximately -0.17 dB at $\lambda = 1.55$ μm. Furthermore, as illustrated in Fig. 2.31b, the S_{31} and S_{41} values corresponding to the waveguide crosstalk, and S_{11} values corresponding to the reflected power, S_{11}, indicate suppression between -29 and -31 dB across the same wavelength range, demonstrating good isolation between mode propagation in the intersecting waveguides. These results are consistent with similar previously reported beam-shaped crossing [218].

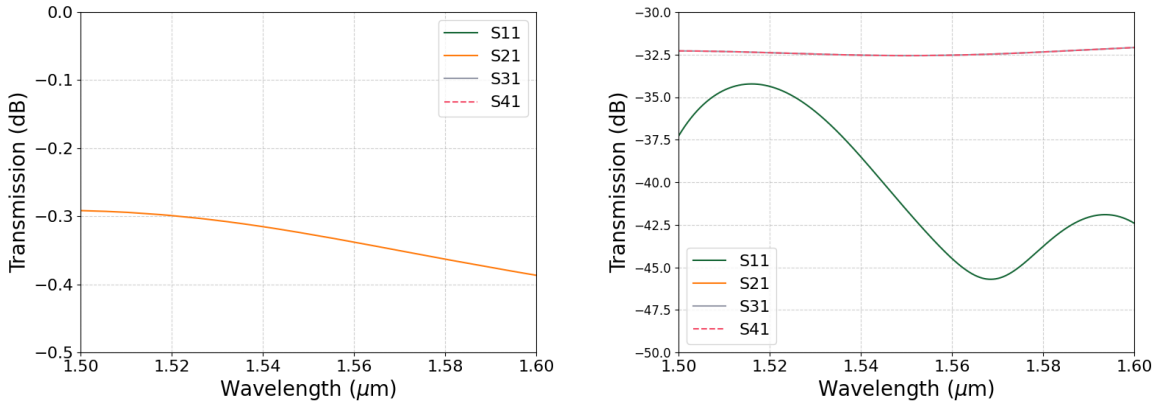

(a) S_{21} TM x-crossing transmission. (b) S_{31} and S_{41} TM x-crossing transmission.

Figure 2.32: Simulated transmission spectra of the x-crossing at $\lambda = 1.55$ μm for the (a) S_{12} transmission with TM polarization, showing a -0.5 dB bandwidth region, and (b) S_{31} crosstalk and S_{41} reflection transmission response down to -47 dB.

For the TM polarization, higher loss is observed compared with the TE transmission spectrum, which can be attributed to weaker mode confinement and less symmetric beam focusing at the intersection region, as shown in Fig. 2.30b. The reduced focusing efficiency leads to slightly higher scattering and radiation loss, resulting in the S_{21} transmission spectrum shown in Fig. 2.32a.

As illustrated in Fig. 2.32a, the S_{21} TM transmission values exhibit loss between -0.3 and -0.4 dB across the wavelength range $\lambda = 1.5 - 1.6$ μm, with an approximate loss of -0.32 dB at $\lambda = 1.55$ μm. Furthermore, as illustrated in Fig. 2.32b, the corresponding crosstalk levels for the TM polarization are slightly higher than for the TE case, with S_{31} and S_{41} values of approximately -32.5 dB and a reflection in the S_{11} port between -34 dB and -45 dB, reaching values of approximately -42 dB at $\lambda = 1.55$ μm, as illustrated

in Fig. 2.32b. Despite this increase in S_{21} transmission loss, the TM performance remains comparable for beam-shaped X-crossing designs [218].

The 3D FDTD simulation results demonstrate that the proposed waveguide x-crossing achieves sub -0.5 dB insertion loss and low crosstalk for both TE and TM polarizations with a compact 10 μm x 10 μm footprint. These results are consistent with similar previous beam-shaping x-crossing devices reported in [218]. The demonstrated performance highlights the beam-shaped x-crossings for dense waveguide routing in InGaAsP-on-insulator photonic integrated circuits, where a compact footprint, low loss, and polarization-tolerant operation are important.

3

Chapter 3: Subwavelength Integrated Photonic Components

3.1 Subwavelength Grating (SWG) Waveguide

Following the discussion of subwavelength photonics in Section 1.5, the overview of the theory of subwavelength structures provides context for the designed subwavelength components discussed here in Chapter 3. In this section, a subwavelength grating (SWG) waveguide is designed for the TE polarization at $\lambda = 1.55$ μm and $\lambda = 1.31$ μm. TE polarization is chosen over TM polarization for its better confinement of light in the waveguides, allowing for easier manipulation, which is important for optical communications, as well as compatibility with other components in the InGaAsP-on-insulator platform. The SWG waveguide is modelled as a periodic waveguide in four steps, first by calculating the photonic band structure within the region below the bandgap for the specific SWG waveguide geometry. Second, verifying the Floquet-Bloch mode for a target frequency in a single 3D FDTD simulation. Third, extracting the effective index and dispersion characteristics for the desired frequency from the photonic band diagram. Finally, injecting the Floquet-Bloch mode into a longer 3D FDTD simulation to ensure lossless propagation [223].

The periodic waveguide structure is depicted in Fig. 3.1. The Floquet-Bloch mode, $F(x, y, z)e^{-ikz}$, of the periodic structure is calculated using 3D FDTD simulations in Lumerical FDTD. In the 3D structure, Bloch boundary conditions are placed on the transverse propagation axis, the x-direction, while PML boundary conditions are placed on the y and z axes, ensuring the Floquet-Bloch condition in the direction of propagation, and minimizing reflections in other directions. For the InGaAsP SWG waveguide presented, the

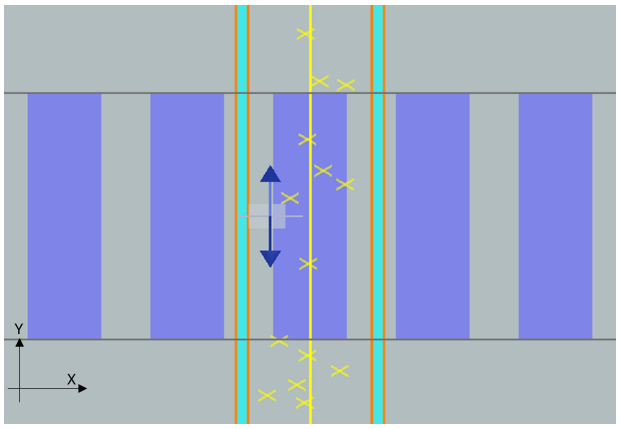

Figure 3.1: Unit cell of the SWG grating waveguide with the pitch $\Lambda = 0.2$ and a duty cycle $f = 0.6$, with a waveguide width of 0.4 μm and height of 0.22 μm. The Bloch boundary conditions are placed on the x-axis with time monitors (yellow stars) placed randomly around the unit cell, a frequency time monitor placed in the middle of the unit cell, and a TE dipole source placed at y = 0 near the unit cell boundary.

unit cell and waveguide grating dimensions are (0.2, 4, 4) μm and (0.12, 0.4, 0.22) μm in $(x,\ y,\ z)$, respectively. For the SWG waveguide, the pitch and duty cycle are $\Lambda = 0.2$ and $f = 0.6$.

The photonic band structure is initially calculated by using several broadband dipole sources placed randomly around the unit cell to ensure all the possible guided modes within the periodic structure are excited. Time monitors, from the bandstructure analysis group found within Lumerical FDTD, are then placed randomly around the unit cell with an appropriate apodization (200 fs) to exclude effects at the start and end of the simulation [224]. The wavevectors are then swept across the first Brillouin zone. In one dimension, the first Brillouin zone contains wavevectors from $-\frac{\pi}{a} \leq k \leq \frac{\pi}{a}$. However, because of the mirror symmetry of the unit cell, only wavevectors within the first Brillouin zone from

$0 \leq k \leq \frac{\pi}{a}$ are taken into account. After normalizing the k vectors ($k = k_x\Lambda/2\pi$), they are swept in a range from $k_x = 0$, the centre of the first Brillouin zone, to the boundary edge, $k = 0.5$. The resulting photonic band diagram in the lossless regime for the TE-like SWG waveguide is shown below in Fig. 3.2.

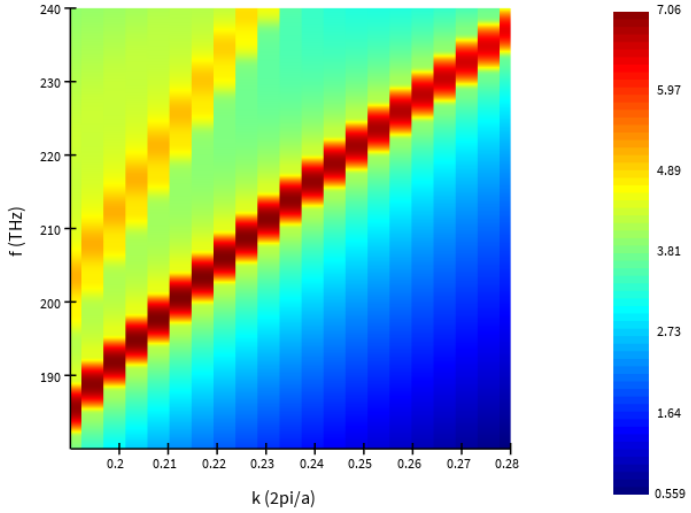

Figure 3.2: Photonic band structure of the TE mode in the subwavelength grating (SWG) waveguide for frequencies between 180–240 THz and Bloch-wavevectors, k_x, between 0.19 – 0.28, the colour plot indicates the resonant peaks of the band structure in arbitrary units.

After the calculation of the photonic bandstructure is complete, the Floquet-Bloch mode at the desired frequencies, 193.414 THz and 228.849 THz (1.55 μm and 1.31 μm), is simulated. The wavevectors corresponding to these frequencies ($k_x = 0.2$, $k_x = 0.263$) are extracted for a single simulation to determine $\omega_n(k)$. To determine the field profile of the Floquet-Bloch mode, a single simulation with the respective wavevector is performed with

a dipole source placed symmetrically across the unit cell to excite the fundamental TE-like mode, and a frequency-time monitor is placed in the centre of the unit cell spanning the simulation domain. This monitor records the Floquet-Bloch mode profile across the centre of the unit cell in the middle of the waveguide grating as shown below in Fig. 3.3.

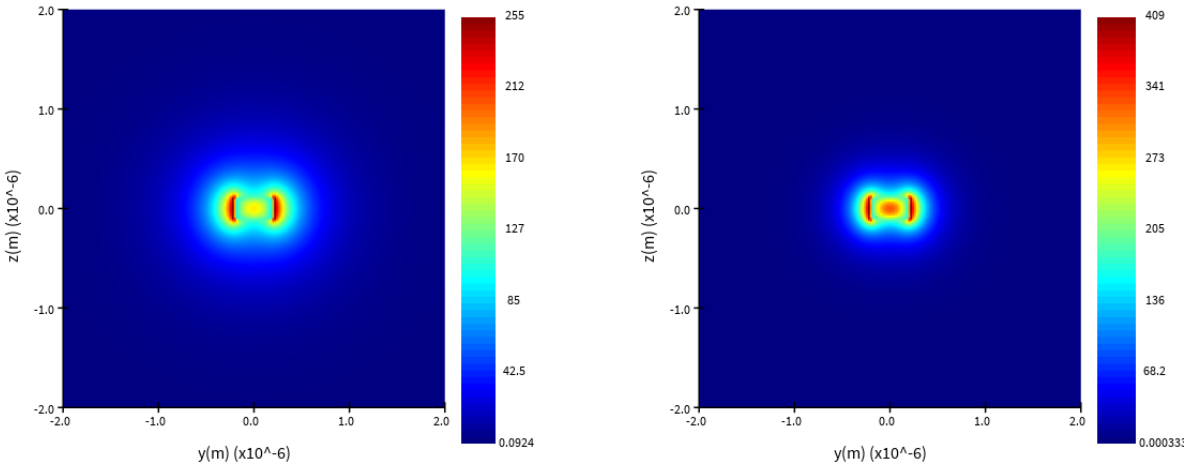

(a) (b)

Figure 3.3: TE-mode field distributions (V/m) at (a) 1550 nm and (b) 1310 nm in the subwavelength InGaAsP-on-insulator waveguide.

To verify both Floquet-Bloch modes propagate without diffraction or loss, the mode profile from the frequency-time monitor is injected into a fixed length, 20 μm, SWG waveguide at the same relative point within the unit cell at the desired carrier frequencies, 193.414 THz (1.55 μm) and 228.849 THz (1.31 μm). A frequency-time monitor is then placed at the output, also within the same relative point in the unit cell. The SWG waveguide is also extended into the PML boundaries to eliminate reflections re-entering the simulation

domain.

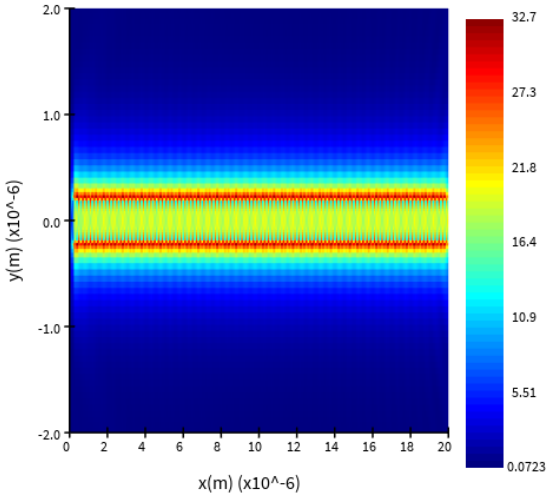

(a)

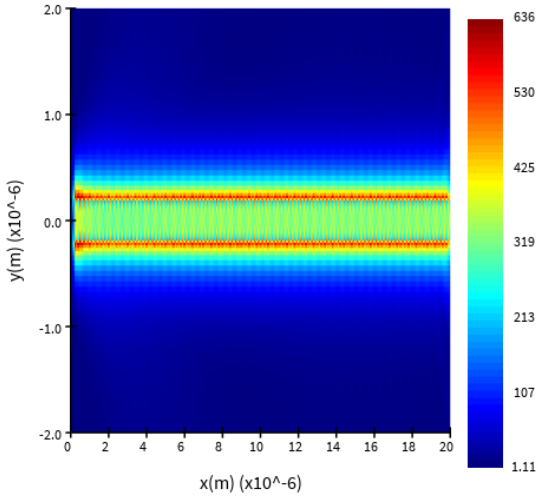

(b)

Figure 3.4: Propagation of the TE Floquet–Bloch mode field (V/m) at (a) 1550 nm and (b) 1310 nm, in a 20 µm InGaAsP-on-insulator SWG waveguide.

As shown in Fig. 3.4, lossless transmission is observed when the mode profile remains continuous in its propagation, and the power output matches the input, within some percentage due to numerical errors and differences in resolution between the calculated field profile and simulation domain. The simulation domain is defined as (20, 4, 4) μm with a high meshing order of 4 in Lumerical FDTD and a time stability factor of 0.3, resulting in an appropriate time step of 0.0124538 fs.

To obtain the effective index, group index, and group velocity dispersion (ps^2/km), a third-order polynomial fitting was used to fit the $\omega_n(k)$ data to the photonic band diagram. As illustrated in Fig. 3.5, the polynomial fitting of the angular frequency over the propaga-

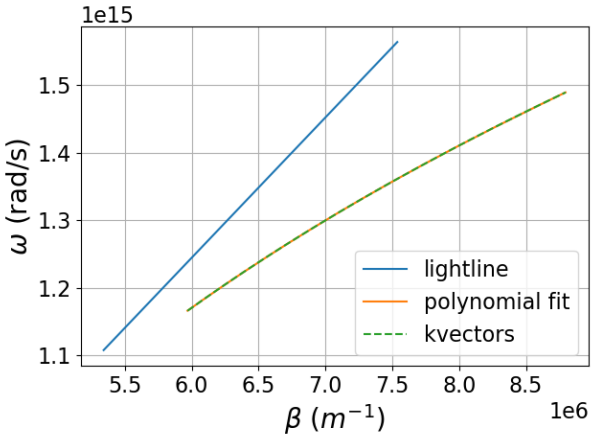

Figure 3.5: Polynomial fit of the wavevector k_x for the TE-like mode as a function of wavelength.

tion constant, ω/β, matches the dispersion relation for the guided TE-like Floquet Bloch modes below the lightline. This dispersion relation is then used to find the parameters

Property	$\lambda = 1.550$ μm	1.310 μm
k_x	0.201	0.263
Effective Index	1.56113	1.72455
Group Index	2.25988	2.99797
Group Velocity Dispersion	9520 (ps^2/km)	11387 (ps^2/km)

Table 3.1: Optical mode characteristics of the fundamental TE mode in the InGaAsP waveguide at 1.550 µm and 1.310 µm. The table lists the wavevector k_x, effective index n_{eff}, group index n_g, and group velocity dispersion (GVD).

listed in Table. 3.2, where

$$n_{\text{eff}}(\omega) = \frac{c\,\beta(\omega)}{\omega}, \tag{3.1}$$

$$n_g(\omega) = c\,\frac{\partial\beta}{\partial\omega}, \tag{3.2}$$

$$\beta_2(\omega) = \frac{\partial^2\beta}{\partial\omega^2}. \tag{3.3}$$

The n_{eff} and n_g listed in Table. 3.2 are consistent with simulated values reported for other SWG waveguides in silicon-on-insulator, a similar high-index contrast platform [108]. The fitted curves and extracted parameters are summarized in Table. 3.2 and Fig. 3.6.

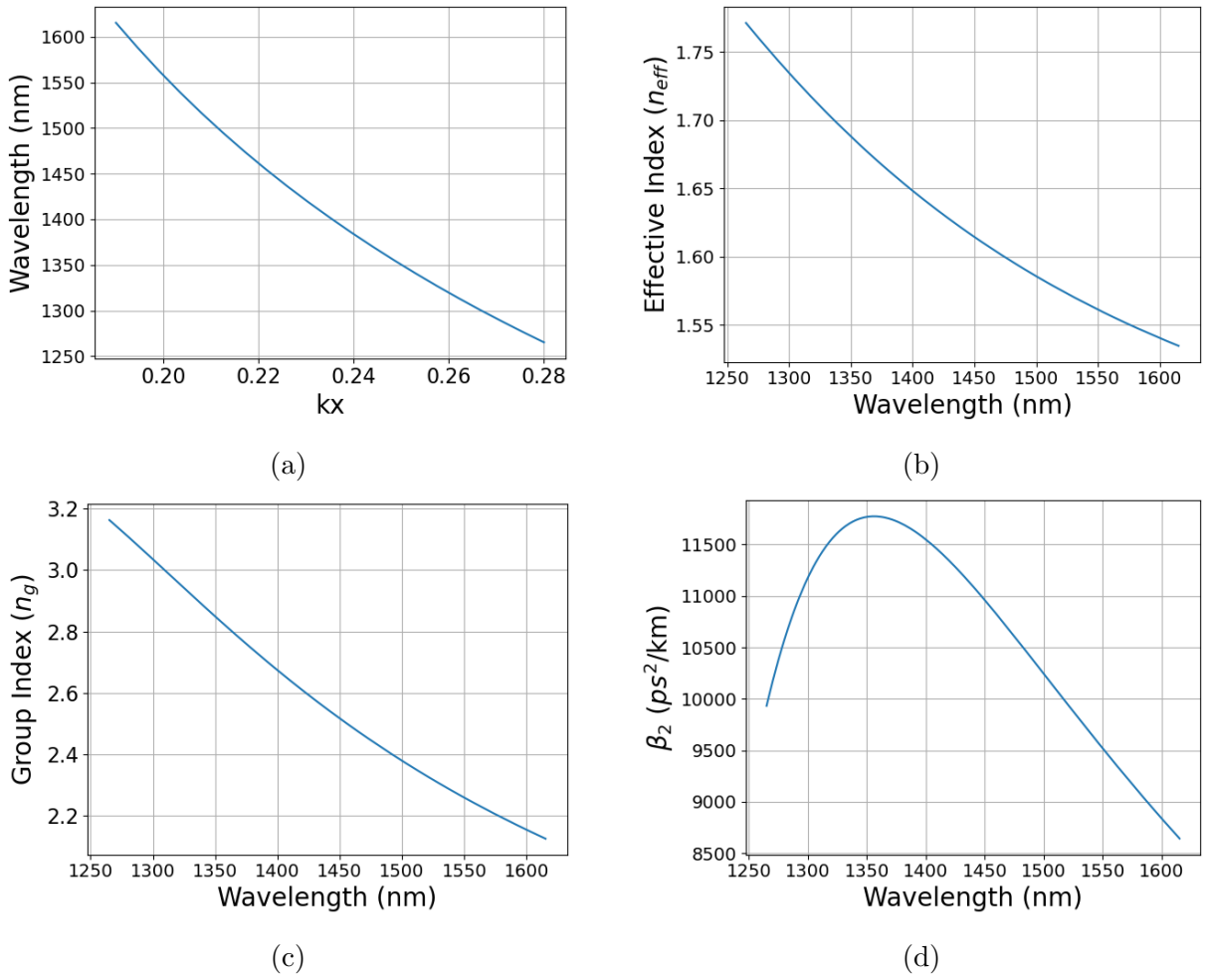

Figure 3.6: TE-mode dispersion characteristics: (a) k-vectors, (b) effective index (n_{eff}), (c) group index n_g, (d) GVD parameter β_2.

Some cases for modelling more complex subwavelength structures benefit from approximation in the deep-subwavelength regime ($\Lambda \ll \lambda$) as homogeneous waveguides using effective medium theory for compact model development [112, 125]. The SWG presented can be treated as an anisotropic homogeneous medium characterized by parallel and perpendicular effective refractive indices $n_{||}$ and $n_{\perp}$ [112]. For the present geometry, at a wavelength of $\lambda = 1.55$ μm, the refractive index of InGaAsP is 3.277 and that of SiO_2 is 1.444. The duty cycle ($f = 0.6$) and pitch ($\Lambda = 0.2$) results in an effective $n_{||}$ and $n_{\perp}$ with the values,

$$n_{||} \approx \left[\frac{0.12}{0.2}(3.277^2) + \left(1 - \frac{0.12}{0.2}\right)(1.444^2)\right]^{\frac{1}{2}} \approx 2.698, \tag{3.4}$$

$$n_{\perp} \approx \left[\frac{0.12}{0.2}(3.277^{-2}) + \left(1 - \frac{0.12}{0.2}\right)(1.444^{-2})\right]^{-\frac{1}{2}} \approx 2.009. \tag{3.5}$$

This gives an equivalent permittivity tensor for the effective homogeneous material,

$$\frac{\epsilon}{\epsilon_0} = n_{eq}^2 = \begin{bmatrix} 7.277 & 0 & 0 \\ 0 & 7.277 & 0 \\ 0 & 0 & 4.037 \end{bmatrix}. \tag{3.6}$$

In this section, the methods and results for designing an InGaAsP-on-insulator SWG waveguide were presented for target wavelengths of 1.55 μm and 1.31 μm. The simulated results presented show a guided Floquet-Bloch mode that can propagate below the

photonic band gap and below the lightline cutoff, in the lossless regime of the photonic band diagram. The effective index, group index, and group velocity dispersion are useful for modelling SWG devices that can be incorporated into more complex circuits for efficient light propagation and manipulation. Further work in this area will benefit from designs for TM polarization at the mentioned wavelengths, as well as mode-converting structures for transitioning from conventional waveguides to meta-waveguides.

3.2 Subwavelength Edge Coupler

The performance of Integrated photonic circuits is largely limited by optical loss associated with components such as waveguides and couplers. Input and output (I/O) couplers, such as edge couplers and surface grating couplers, are especially important for coupling light into and out of photonic circuits. The performance of these components is measured directly by their coupling loss, which describes the power efficiency when coupling light, often from an optical fibre into the chip. Various approaches have been explored for reducing the coupling loss for both fibre and free space coupling, including inverse tapers [225], V-grooved coupling stages [226], and micro lenses [227].

Among approaches for fibre coupling light into photonic circuits, the edge coupler is a popular choice for maintaining low coupling loss and broadband performance compared to surface grating couplers, which achieve best coupling efficiencies of approximately -3.8 dB [113]. However, the distinction of edge couplers from surface grating couplers is that the edge couplers require the wafer to be diced to expose the chip facet and precise alignment of optical fibres, which increases fabrication complexity. In addition, edge couplers traditionally have lengths which can exceed 300 μm, thus making dense integration difficult [228]. To address this limitation, subwavelength grating (SWG) edge couplers offer compact footprints while maintaining high coupling efficiency. Examples of these couplers have been realized in silicon, with device lengths below 70 μm and coupling loss as low as -0.32 dB [117]. In this section, we present a high-performance subwavelength edge coupler

Figure 3.7: Geometry of a subwavelength edge coupler, where section A denotes the grating width at the end of the taper from the tip of the edge coupler, B denotes the starting grating width of the following taper section, and C denotes the starting width of the solid core waveguide taper which couples the mode to a single-mode waveguide. Figure from [117].

for the InGaAsP-on-insulator platform. The proposed device has a total length of 45 μm and simulated coupling loss near -0.5 dB at $\lambda = 1.55$ μm, following design strategies such as those described in [117], for an edge coupler such as the one illustrated in Fig. 3.7.

To couple light efficiently from an optical fibre, two different sections of the edge coupler, illustrated in Figs. 3.8 - 3.12, must be carefully designed: i) the taper tip, illustrated in Fig. 3.8, which will face the edge of the chip and interface directly with light from the optical fibre, and ii) the subwavelength and solid linear taper sections, which gradually transform the optical mode into the single-mode waveguide of dimensions 500 nm $\times$ 220 nm, illustrated in Fig. 3.11. The junction of these two sections, illustrated in Fig. 3.10, should also be carefully designed.

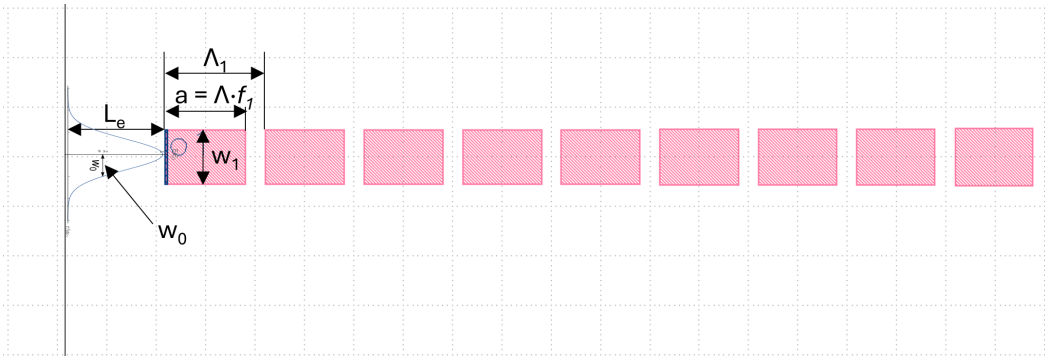

Figure 3.8: Subwavelength grating (SWG) edge coupler tip geometry.

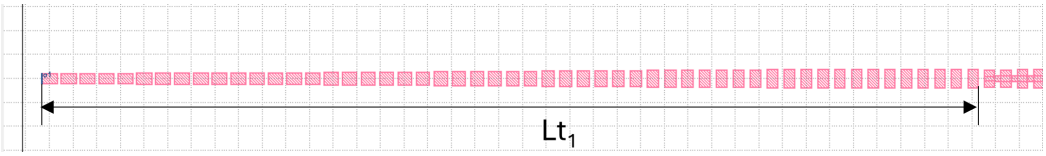

Figure 3.9: Subwavelength grating (SWG) edge coupler taper geometry.

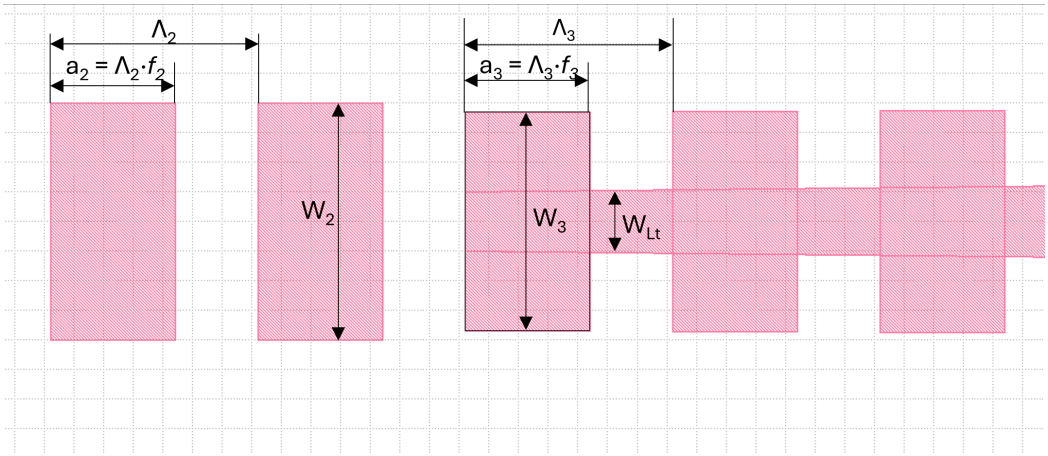

Figure 3.10: Subwavelength grating (SWG) edge coupler taper junction, showing the transition from the grating region to the linear taper and grating section.

In this work, a polarization-maintaining anti-reflective tapered lensed fibre from Oz Optics Ltd. (TPMJ-X-1550-8/125-0.4-10-2.5-14-1-AR) is assumed to be the input source.

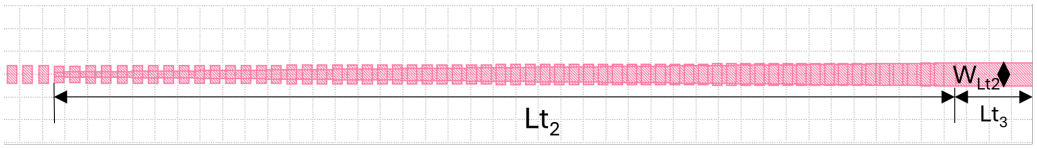

Figure 3.11: Second taper section of the subwavelength grating (SWG) edge coupler.

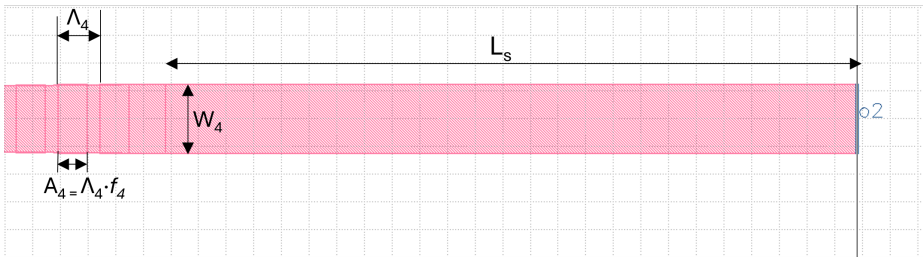

Figure 3.12: Transition of the second taper section of the subwavelength grating (SWG) edge coupler leading into a straight waveguide.

The optical fibre coupling is assumed to have a Gaussian field intensity for an ideal mode field diameter of 2.5 $\pm$0.5 μm (MFD, at $1/e^2$ intensity) at $\lambda = 1.55$ μm, illustrated in Fig. 3.13a. To ensure maximum coupling efficiency, the guided mode at the coupler tip must overlap strongly with the Gaussian mode from the optical fibre.

To evaluate this mode overlap, the SWG section at the tip of the edge coupler is modelled as a homogeneous waveguide in Lumerical FDE, and the mode overlap between the Gaussian mode and guided TE mode is calculated [229]. The mode fields are illustrated in Fig. 3.13, providing a maximum overlap of 0.938 for the TE mode of a 190 nm wide and 220 nm tall waveguide and an overlap of 0.910 for the TM mode, indicating a strong spatial match between the fibre and on-chip modes.

As illustrated in Fig. 3.13b, the small waveguide width of 190 nm lowers the effective

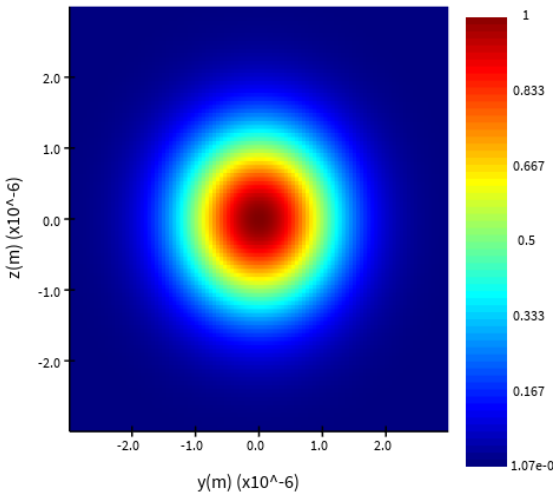

(a) Gaussian input mode field profile used for coupling into the edge coupler, with beam radius $w_0 = 1.25$ μm.

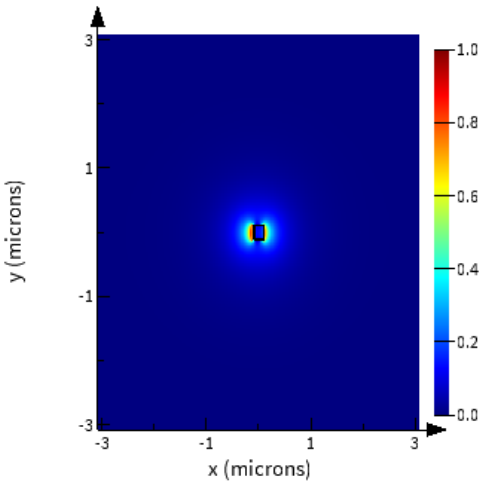

(b) Electric-field profile of the TE_{00} mode for the 190 nm-wide InGaAsP waveguide.

Figure 3.13: Comparison of the normalized electric field amplitude of a Gaussian fibre mode and the guided TE_{00} mode at the 190 nm-wide SWG edge coupler tip, illustrating mode matching for efficient fibre-to-chip coupling.

index of the waveguide and expands the optical mode into the cladding, providing stronger field overlap with the Gaussian beam, and minimizing scattering and radiation loss between the fibre-chip interface. To determine the alignment tolerance, the mode overlap is calculated as a function of the lateral fibre misalignment, as illustrated in Fig. 3.14. Here, a coupling efficiency above 80% is maintained for lateral misalignment of less than 0.7 μm.

However, in realistic packaging of integrated circuits, the chip edge commonly contains

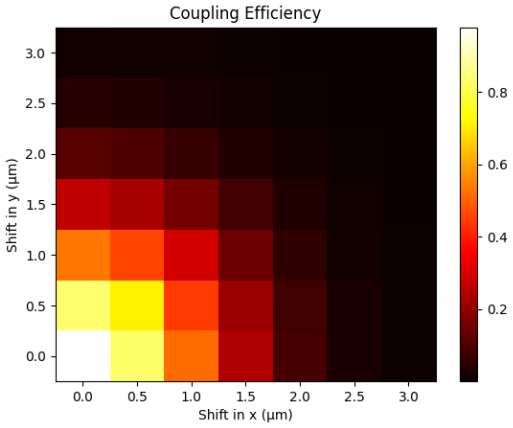

Figure 3.14: mode overlap alignment tolerance for a 190 nm waveguide width of the tip of the SWG edge coupler.

a small cladding region before the waveguide tip, particularly in non-polished chip facets. Because of this, the full three-dimensional FDTD simulation incorporates a 0.5 μm cladding separation to the edge coupler tip that causes the field profile to change slightly, shifting the optimal tip width to 220 nm. This new ideal mode overlap can be seen in the coupled mode at the tip of the edge coupler in Fig. 3.15. The change from the ideal overlap analysis in realistic coupler constraints highlights how full-vectorial simulation can account for these conditions.

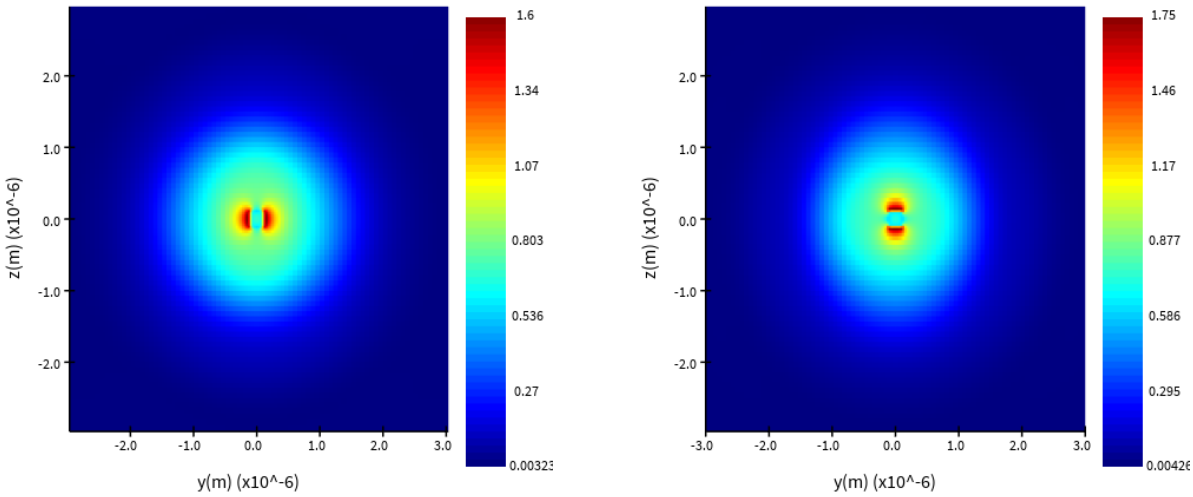

(a) Coupled optical mode at the edge-coupler tip for TE polarization.

(b) Coupled optical mode at the edge-coupler tip for TM polarization.

Figure 3.15: Simulated electric-field profiles (V/m) at the tip of the subwavelength grating edge coupler after coupling from a Gaussian input beam for (a) TE and (b) TM polarizations.

To couple the mode present at the tip of the edge coupler, illustrated in Fig. 3.15, the grating pitch near the coupler tip is chosen to be sufficiently away from the bandgap pitch, described by

$$\Lambda_{\text{Bragg}} = \frac{\lambda_{\text{g}}}{n_{\text{eff}}} = \frac{1.55\ \mu\text{m}}{1.47} = 1.05\ \mu\text{m}, \tag{3.7}$$

where 1.47 is the effective index of the TE-like Floquet Bloch mode present at the tip of the edge coupler. From this point, the mode effective index is gradually transformed from that near the cladding, $n_{\text{cl}} = 1.445$, to that of the straight waveguide, $n_{\text{wg}} = 2.24$ (TE

mode), using pitch and duty cycle variation. A pitch of 0.4 μm and duty cycle of 0.8 is chosen near the tip, based on parameter sweeps for maximizing transmission through a 20 μm taper length (Lt_1) to a wider waveguide grating width (w_2) of 400 nm.

Following the tip interface with the Gaussian field profile, the optical mode is adiabatically transformed through the first taper, Lt_1, using a chirped SWG taper, as illustrated in Fig. 3.9. In this section of the coupler, the pitch and duty cycle of the subwavelength taper will vary from 0.4 to 0.35 μm and 0.8 to 0.6, respectively, while increasing the grating width from 0.22 μm at the tip to 0.4 μm over a distance Lt_1. The grating pitch, duty cycle, and grating width over this distance are varied smoothly using a cosine function,

$$f(x) = a + (b - a)\frac{1 - \cos(\pi x/L)}{2}, \tag{3.8}$$

where a is the starting position of the gratings, b is the end position of the gratings, and L is the tapering length over which the gratings' width will change. This function is chosen for an adiabatic transition to ensure that the mode evolution starts and ends with zero slope, ideal for minimizing scattering between the different tapering sections of the coupler and not exciting higher-order modes. At the junction of the SWG region and the linear taper, illustrated in Fig. 3.10, the volume fraction of the high-index InGaAsP material and low-index cladding material (SiO_2) is matched approximately, and refined in 3D FDTD simulations, following design methods described in [117]. This approximate volume fraction matching between the gratings and the solid-core linear taper at the taper junction minimizes mode mismatch between the two taper sections and aids in a low-loss

Parameter	dimension (μm)
beam radius (w_0)	1.25
chip edge distance (L_e)	0.5
Width 1 (w_1)	0.22
waveguide height (h)	0.22
tip section pitch 1 (Λ_1)	0.4
tip section duty cycle 1 f_1	0.8
Tip section taper length (L_t)	20
tip section pitch 2 (Λ_2)	0.35
tip section duty cycle 2 (f_2)	0.6
Width 2 (w_2)	0.4
Width 3 (w_3)	0.36
taper section pitch 1 (Λ_3)	0.35
taper section duty cycle 1 (f_3)	0.6
linear taper width 1 (w_{Lt})	0.1
taper section length 2 (Lt_2)	20
linear taper length 2 (Lt_2)	20
taper section pitch 2 (Λ_4)	0.3
taper section duty cycle 2 (f_4)	0.7
straight waveguide width (w_4)	0.5
straight waveguide length (L_s)	5

Table 3.2: Geometrical parameters of the InGaAsP-on-insulator subwavelength edge coupler

transition between the grating and the solid-core waveguide. From this point, the pitch, Λ_3, duty cycle, f_3, and width w_3, of the gratings will vary linearly over 20 μm (Lt_2), to be a pitch Λ_4, duty cycle, f_4, and width w_4, adiabatically coupling the TE-like mode into the 500 nm width, 220 nm height single-mode waveguide, illustrated in Figs. 3.11 and 3.12. Throughout the edge coupler, the grating pitch and duty cycle are chirped to reduce the potential for Bragg resonances, as listed in Table 3.2 with the full parameters of the subwavelength edge coupler.

The simulation for the edge coupler was performed using three-dimensional FDTD simulations in Ansys Lumerical FDTD using a mesh refinement level of 4 and a stability factor of 0.3, corresponding to a time step of 0.0183 fs, yielding accurate results and reasonable simulation times. The simulation domain, illustrated in Fig. 3.16, was 45 $\times$ 9.5 $\times$ 6.22 μm in (x, y, z), and included an 8-layer PML boundary on all sides to reduce reflections from entering back into the simulation domain. To simulate the TE and TM-polarized coupling, the polarization angle of the Gaussian mode is set to 0 and 90°, respectively, as illustrated in the mode coupled into the waveguide tip in Figs. 3.15a and 3.15b. The Gaussian beam source was placed 0.5 μm from the tip of the edge coupler, modelling realistic fibre-to-chip coupler constraints, where the facet of the chip has a small amount of cladding material before the tip of the coupler.

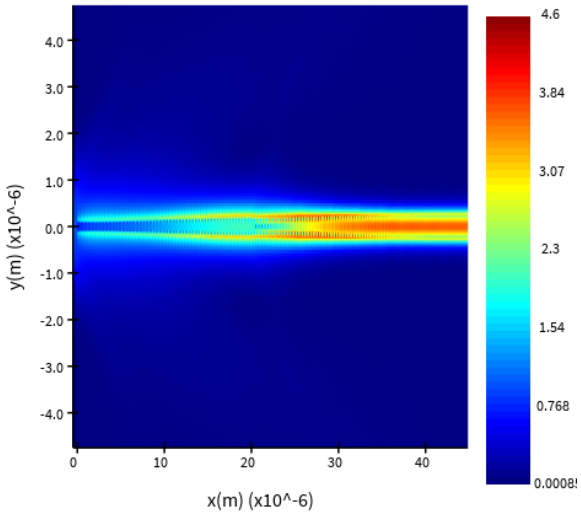

Figure 3.16: Mode evolution of the electric field (V/m) of the coupled TE Gaussian mode to the straight waveguide in the subwavelength edge coupler.

The simulated transmission spectrum, shown in Figs. 3.17a and 3.17b, indicate coupling loss of approximately -0.58 dB at $\lambda = 1.55$ μm for TE-polarized light, and as low as -0.4 dB for TM-polarized light at the same wavelength. The TM polarization exhibits a smoother transmission spectrum profile across the $1.5 - 1.6$ μm wavelength range, with sub -1 dB coupling loss maintained across the entire bandwidth. This improved TM performance could be due to the reduced interaction with the waveguide sidewalls compared to the TE mode, reducing the scattering and mode-mismatch losses during propagation through the grating and taper sections. In addition, the square geometry of the waveguide tip minimizes asymmetry in the TE and TM mode coupling, thus reducing polarization-dependent loss and enabling high-performance for coupling the TE and TM modes into

the waveguide.

Overall, the remaining loss seen can likely be attributed to mode-mismatch loss at the chip facet, as well as small radiation loss and scattering loss at interfaces between grating sections and the taper junction. Despite the residual loss, the compact 45 μm footprint for the subwavelength edge coupler presented here achieves good simulated coupling efficiency, in both TE and TM polarizations, comparable to the performance of other designs for edge couplers reported in [228, 230].

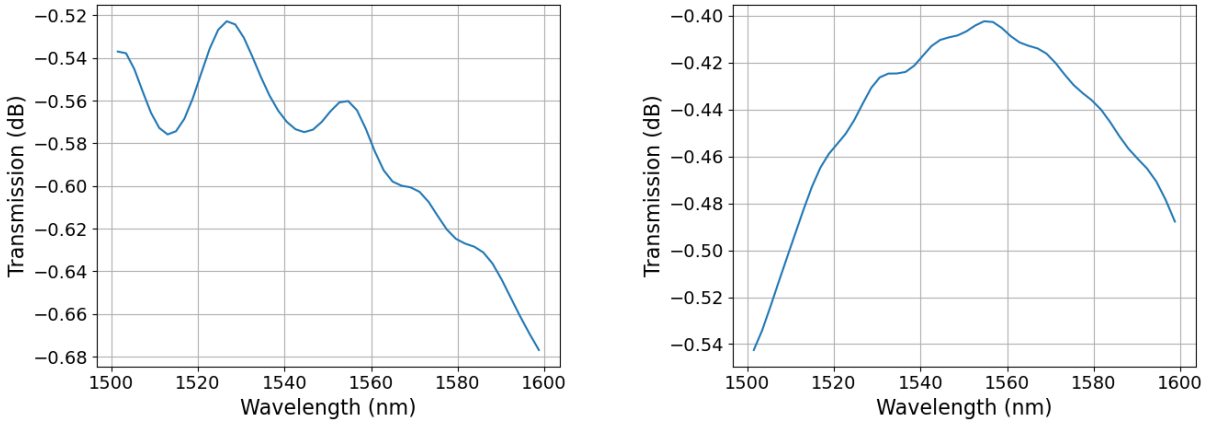

(a) TE-polarized transmission of the SWG edge coupler.

(b) TM-polarized transmission of the SWG edge coupler.

Figure 3.17: Simulated transmission spectrum of the subwavelength grating (SWG) edge coupler for (a) TE and (b) TM polarizations over the wavelength range $1500 - 1600$ nm.

Further improvements may be achieved by optimizing the tip geometry of the edge coupler to reduce end-face mode mismatch between the taper tip and the Gaussian field profile, as well as increasing alignment tolerance. Increased alignment tolerance can be achieved by incorporating other subwavelength designs such as trident couplers and multi-layer systems for increased size of supported mode, improving compatibility with standard SMF-28 optical fibres, which have a larger mode diameter of approximately 10.5 μm. Additionally, smaller minimum feature sizes below 60 nm in fabrication could allow for a smaller pitch and further reduction of the overall device length needed for adiabatic coupling. Overall, the subwavelength edge coupler presented here demonstrates advantages for creating compact, low-loss, and broadband I/O couplers well-suited for dense integration in the InGaAsP-on-insulator platform.

4

Chapter 4: Second Harmonic Generation in InGaAsP-on-insulator waveguides

4.1 Second Harmonic Generation

In this chapter, we present a design of an InGaAsP-on-insulator waveguide suitable for phase-matched second-harmonic generation (SHG) via modal phase-matching. Furthermore, we derive the second-harmonic generation conversion efficiency, which is then applied to dielectric waveguides for analytical efficiency calculations, in units of %/W, for a designed 2 mm-long InGaAsP-on-insulator waveguide. The purpose of developing components for second-harmonic generation is to enable on-chip wavelength conversion applicable for sensing and data transmission, as well as demonstrate a general modelling framework for second-order nonlinear processes. The methods proposed in this section can then be extended to processes such as sum-frequency generation (SFG), difference-frequency generation (DFG), and spontaneous parametric down conversion (SPDC) for applications in environmental sensing, quantum information processing, and more.

To begin, we derive the equations used to calculate SHG efficiency using the procedures for coupled wave equations in sum-frequency generation outlined in [75]. Recalling the nonlinear wave equation from Eq. (1.36), to determine the solution to a field generated in a nonlinear material, defined as

$$\tilde{E}_3(z,t) = A_3 e^{i(k_3 z - \omega_3 t)} + c.c, \tag{4.1}$$

where A_3 is the slowly varying complex amplitude of the generated field and $k_3 = (n_3\omega_3)/c$ is the wavenumber.

The derivation of this equation begins from the nonlinear polarization source term for the generated electric field, $\tilde{E}_3(z,t)$, described by:

$$\tilde{P}_3(z,t) = P_3 e^{-i\omega t} + c.c, \tag{4.2}$$

where P_3 is given by

$$P_3 = 4\epsilon_0 d_{\text{eff}} E_1 E_2. \tag{4.3}$$

Here, d_{eff} is the effective second-order nonlinear coefficient, related to the second-order susceptibility by $d_{il} = \chi^{(2)}/2$, and has units of pm/V. The permittivity of free space is ϵ_0, ($\epsilon_0 = 8.85 \times 10^{-12}$ F/m), and E_1 and E_2 are the applied electric fields, denoted by

$$\tilde{E}_i(z,t) = E_i e^{-i\omega_i t} + c.c, \tag{4.4}$$

where

$$E_i = A_i e^{ik_i z}. \tag{4.5}$$

Here, A_i is the slowly varying field envelope, and the exponential term with the complex phase factor, $e^{ik_i z}$, describing the propagation phase.

Combining Eqs. (4.2) $-$ (4.5) into the nonlinear wave, equation Eq. (1.36), gives the

expression for the generated field for sum-frequency generation, as described in [75]:

$$\frac{dA_3}{dz} = \frac{2id_{eff}\omega_3}{n_3 c} A_1 A_2 e^{i(k_1+k_2-k_3)}, \tag{4.6}$$

where n_3 is the effective refractive index at the frequency of the generated wave.

This derivation assumes the slowly varying envelope approximation,

$$\left| \frac{d^2 A_3}{dz^2} \ll k_3 \frac{dA_3}{dz} \right|, \tag{4.7}$$

where the second-order spatial derivatives of the envelope in Eq. (1.36) can be neglected.

The coupling between the waves in Eq. (4.6) is largely determined by the exponential phase term,

$$\Delta k = k_1 + k_2 - k_3, \tag{4.8}$$

known as the wavevector (phase) mismatch. For SHG, this reduces to $\Delta k = 2k_\omega - k_{2\omega}$, since the two input fields have the same frequency. Following a similar procedure, the coupled amplitude equations for the fundamental fields, A_1 and A_2, are found to be

$$\frac{dA_1}{dz} = \frac{2id_{\text{eff}}\omega_1}{n_1 c} A_3 A_2^* e^{-i\Delta k}, \tag{4.9}$$

$$\frac{dA_2}{dz} = \frac{2id_{\text{eff}}\omega_2}{n_2 c} A_3 A_1^* e^{-i\Delta k}. \tag{4.10}$$

To determine the efficiency of the nonlinear process, we integrate the field over a propaga-

tion length L,

$$A_3(L) = \frac{2id_{eff}\omega_3 A_1 A_2}{n_3 c}\int_0^L e^{-i\Delta k}dz = \frac{2id_{eff}\omega_3 A_1 A_2}{n_3 c}\left(\frac{e^{i\Delta kL}-1}{i\Delta k}\right). \tag{4.11}$$

The intensity of an electric field is described by

$$I_i = 2n_0\epsilon_0 c\left|A_i\right|^2, \tag{4.12}$$

where n_0 is the linear refractive index, and A_i is the amplitude of the given field. Incorporating Eq. (4.12) into Eq. (4.11), the intensity of the generated field in sum-frequency generation is described as

$$I_3 = \frac{2d_{\text{eff}}^2\omega_3^2 I_1 I_2}{n_1 n_2 n_3 \epsilon_0 c^3}L^2\text{sinc}^2\left(\frac{\Delta kL}{2}\right), \tag{4.13}$$

where simplifications are made for the modulus squared of the integrated complex phase factor. The effective indices of the respective fields are denoted by $n_1, n_2,$ and n_3, respectively. Applying this expression to second harmonic generation, where the input fields, A_1 and A_2 are identical, we obtain the expression

$$I(2\omega, L) = \frac{2\omega^2 d_{\text{eff}}^2 I_\omega^2 L^2}{n_{2\omega}n_\omega^2 c^3\epsilon_0}\text{sinc}^2\left(\frac{\Delta kL}{2}\right), \tag{4.14}$$

where $n(\omega)$ and $n(2\omega)$ are the effective refractive indices at the fundamental frequency and second-harmonic, and the intensity of the input field is given by I_ω.

The efficiency of the nonlinear process is strongly influenced by the effective nonlinear coefficient, d_{eff}. For InGaAsP, the d_{41} tensor component is used, under approximations from Kleinmann symmetry, valid for wavelength ranges far from material resonances. This effective nonlinear susceptibility is calculated using the linear electro-optic coefficient [76]:

$$d_{41}(\omega, \omega, 0) = -\frac{1}{4}\epsilon_1^2(\omega) r_{41}^s(\omega). \tag{4.15}$$

As illustrated in Fig. 4.1, the low-dispersion regime is used to estimate the effective nonlinear susceptibility value of 40 pm/V for $In_{0.14}Ga_{0.86}As_{0.3}P_{0.7}$,

$$d_{\text{eff}} = d_{41} = 40 \text{ pm/V}. \tag{4.16}$$

using Eqs. (4.14) and (4.15), the SHG efficiency for a dielectric waveguide can be expressed as

$$\Gamma = \frac{P_2}{P_1^2} = \frac{8\pi^2}{\epsilon_0 c n_1^2 n_2 \lambda^2} \frac{\zeta^2 d_{\text{eff}}^2}{A_{\text{eff}}} L^2 \text{sinc}^2\left(\frac{\Delta L}{2}\right). \tag{4.17}$$

Here, ζ is the nonlinear spatial modal overlap between the fundamental and second harmonic wavelengths, for the face of a waveguide in the x, z plane, described as

$$\zeta = \frac{\int_{\chi^{(2)}} (E_{1x}^*)^2 E_{2z} dx dz}{\left| \int_{\chi^{(2)}} \left|\vec{E_1}\right|^2 \vec{E_1} dx dz \right|^{\frac{2}{3}} \left| \int_{\chi^{(2)}} \left|\vec{E_2}\right|^2 \vec{E_1} dx dz \right|^{\frac{1}{3}}}, \tag{4.18}$$

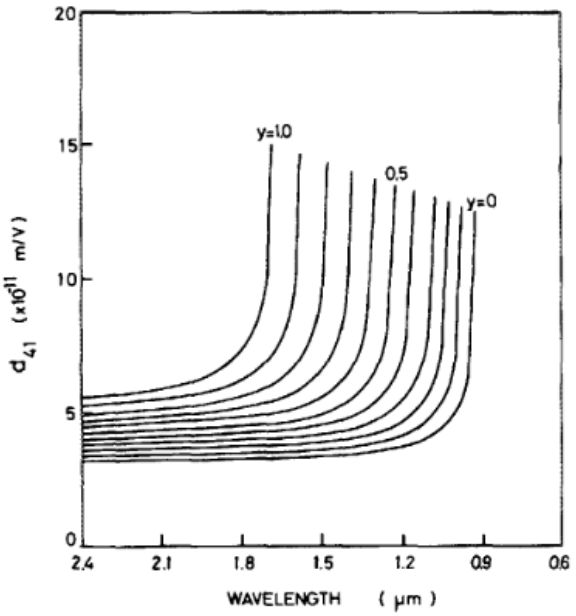

Figure 4.1: calculated optical rectification coefficients, $d_{41}(\omega, \omega, 0)$, of $In_{1-x}Ga_xAs_{1-y}P_y$ lattice matched to InP as a function of the y concentration. Figure taken from [76].

and A_{eff} is the effective mode area,

$$A_{\text{eff}} = \left(A_1^2 A_2\right)^{\frac{1}{3}}, \tag{4.19}$$

where A_i (i=1,2), is described by:

$$A_i = \frac{(\int_{all} \left|\vec{E_i}\right|^2 dxdz)^3}{\left|\int_{\chi^{(2)}} \left|\vec{E_i}\right|^2 \vec{E_i} dxdz\right|^2}, \tag{4.20}$$

and $\int_{all}$ calculates the field over all space, and $\int_{\chi^{(2)}}$ calculated the field within the area of

the nonlinear $\chi^{(2)}$ waveguide. This formulation creates a framework for calculating SHG efficiencies in dielectric waveguides.

Commonly, the process for modal phase-matching in waveguides utilizes the fundamental TE_{00} or TM_{00} mode and higher order modes such as TE_{02} or TM_{02} at the second-harmonic [231]. As illustrated in Fig. 4.2, modal phase-matching allows for matching the fundamental mode to higher-order modes which have lower effective indices. The benefit of this approach is that phase-matching becomes achievable at a wider range of waveguide geometries; however, the overall conversion efficiency is reduced due to the low modal overlap caused by the difference in mode shapes.

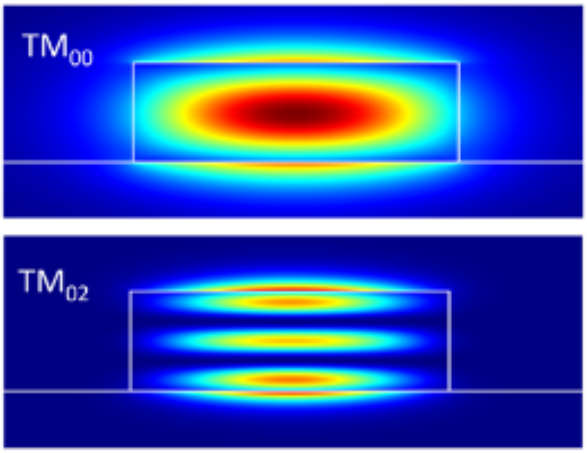

Figure 4.2: field profiles of a modal phase-matched silicon nitride waveguide for the TM_{00} and TM_{02} modes. Figure from [231].

To address this disadvantage, in this chapter, we design asymmetric InGaAsP-on-insulator waveguides to phase-match orthogonal polarizations of the fundamental TE_{00} mode to the second-harmonic TM_{00} mode, enhancing the modal overlap within the non-

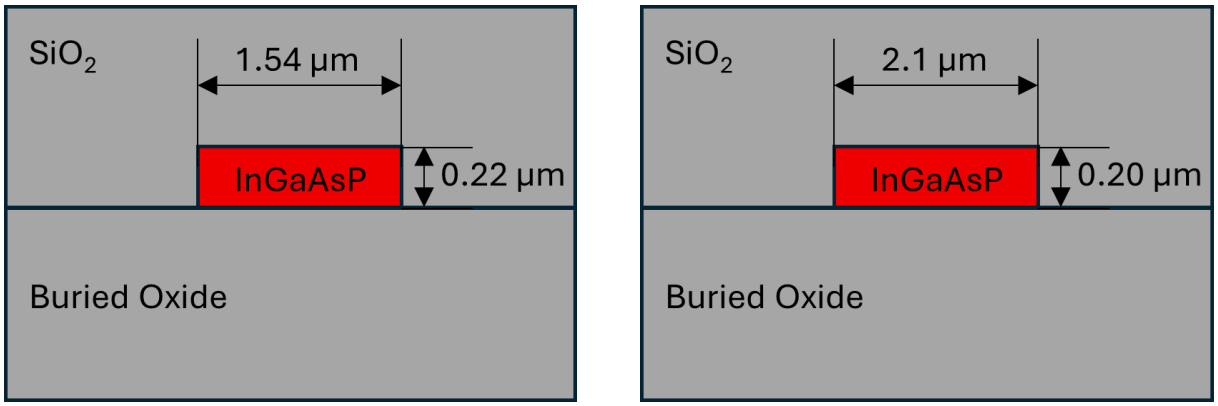

(a) 3.1 μm to 1.55 μm. (b) 2.62 μm to 1.31 μm.

Figure 4.3: Schematic layouts of InGaAsP-on-insulator waveguides designed for modal phase-matched second-harmonic generation at a) 3.1 μm to 1.55 μm, and b) 2.62 μm to 1.31 μm.

linear waveguide. Such methods have also been seen to efficiently produce the second-harmonic mode in AlGaAs-on-insulator [232]. The designed waveguides in this chapter are illustrated in Fig. 4.3a and 4.3b, with dimensions of 1.54 $\times$ 0.22 μm for conversion of 3.1 μm to 1.55 μm, and 2.1 $\times$ 0.2 μm for conversion of 2.62 μm to 1.31 μm.

4.1.1 Results and Discussion

The results of the SHG performance of InGaAsP-on-insulator waveguides are discussed in this section. Analytical efficiency calculations are performed using Eq. (4.17), and the resulting SHG efficiencies are illustrated in Figs. 4.9a and 4.9b. In this approach, the SHG efficiency is calculated in units of % / W for two wavelength ranges in 2 mm long InGaAsP-on-Insulator waveguides, neglecting loss, pump-depletion, and free-carrier effects. These assumptions correspond to the undepleted-pump, continuous-wave (CW) regime and serve as an upper bound on the achievable conversion efficiency.

The analytical approach used here follows similar coupled-mode derivations applied to dielectric waveguides consistent with methods presented in [75, 233, 234], and gives comparable efficiencies and mode confinements to those found in literature for similar waveguide geometries and effective nonlinear coefficients in Lithium Niobate and AlGaAs [233, 235, 236].

The SHG waveguides are designed to convert the fundamental infrared wavelengths of approximately 3.10 μm and 2.62 μm into telecom wavelengths of 1.55 μm and 1.31 μm, respectively. This wavelength conversion is beneficial for environmental sensing applications, as molecules such as sulphur dioxide (SO_2), ethanol (C_2H_5OH), and several chlorofluorocarbons exhibit strong absorption features in the mid-infrared spectral region [104, 237, 238]. Furthermore, demonstrating efficient second-order nonlinearity in InGaAsP-on-insulator waveguides highlights the potential for further study of nonlinear processes such as difference frequency generation for reaching the mid-infrared and THz frequencies, and

sum-frequency generation for efficient wavelength conversion.

The waveguides considered in this section are assumed to operate in the continuous-wave (CW) regime, and effects associated with optical pulse propagation, such as group velocity dispersion, are not considered in the efficiency calculations. To evaluate the phase-matching between the frequencies, the effective indices for the TE_00 and TM_00 modes are calculated across the fundamental wavelength ranges of $\lambda = 3.05 - 3.15$ μm and $\lambda = 2.60 - 2.65$ μm, as well as the corresponding second harmonic wavelength ranges $\lambda = 1.5 - 1.6$ μm and $\lambda = 1.3 - 1.325$ μm. These results are illustrated in Figs. 4.4a and 4.4b.

The effective indices are computed using an FDE solver with PML boundary conditions in a large simulation domain of 8 μm$\times$ 8 μm, and a spatial resolution of 10 nm. This large simulation domain ensures that the modal fields decay to approximately -10 dB at the simulation boundaries, minimizing numerical error and ensuring the entire mode is captured within the simulation domain. The calculated effective indices of the fundamental TE mode and second-harmonic TM mode intersect at the target wavelength pairs, indicating near-zero wavevector mismatch ($\Delta k = 0$). At these points, modal phase matching is achieved for a finite wavelength range, implying a limited phase-matching bandwidth, related to the spectral width of the SHG response shown in Figs. 4.9a and 4.9b.

Following the determination of the effective indices, the nonlinear spatial mode overlap, ζ, and effective mode area, A_{eff}, are calculated using the simulated mode profiles illustrated in Figs. 4.5 - 4.8. For SHG from 3.1 μm to 1.55 μm, the waveguide core dimensions are 1.54

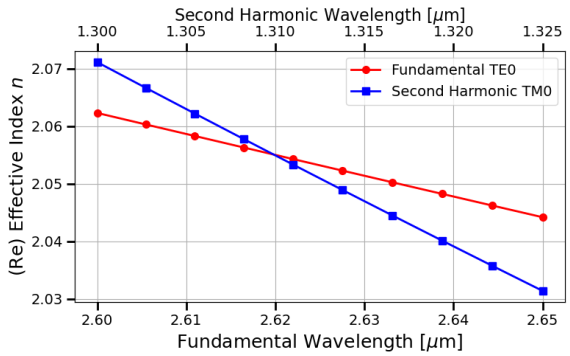

(a) 2620 – 1310 nm effective index plot.

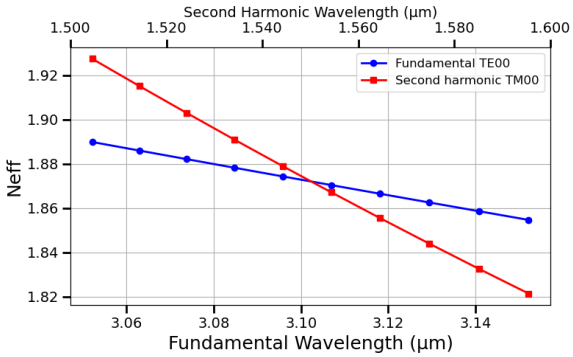

(b) 3100 – 1550 nm effective index plot.

Figure 4.4: Comparison of the effective indices for the fundamental and second-harmonic modes of two wavelength pairs.

μm width and 0.22 μm height, and for the conversion of 2.62 μm to 1.31 μm, the waveguide has a core dimension of 2.10 μm x 0.20 μm. These asymmetric waveguide geometries enhance the mode overlap between the fundamental and second-harmonic modes.

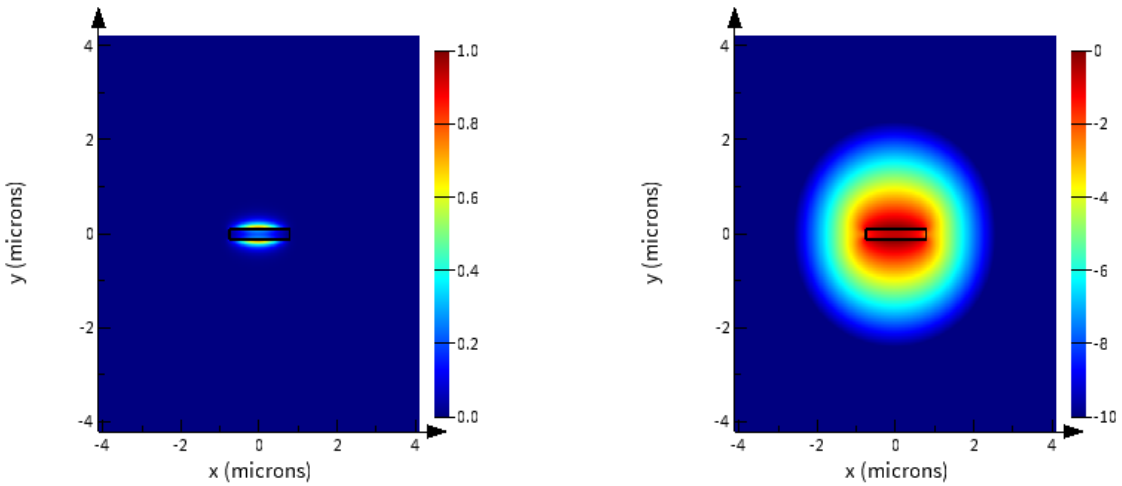

(a) $\lambda = 1.55$ μm linear scale.

(b) $\lambda = 1.55$ μm log scale.

Figure 4.5: Normalized electric field mode profiles on a linear and logarithmic scale for the TM_{00} mode at $\lambda = 1.55$ μm.

The calculated values of the effective mode area, A_{eff}, and nonlinear spatial mode overlap, ζ, are summarized in Table 4.1. The nonlinear spatial mode overlap has values between 0.63 and 0.68 for both wavelength ranges, indicating a strong spatial overlap within the waveguide core for wavelength conversion. The effective mode area is relatively small, with values of approximately 9.2 μm^2 and 4.7 μm^2, reflective of high optical confinement enhanced by the large refractive index contrast of the InGaAsP-on-insulator platform. Both of these factors are important for high conversion efficiency as the efficiency scales quadratically for ζ and inversely with A_{eff}.

Using the parameters listed in Table 4.1, and the effective indices in Fig. 4.4, the SHG efficiency is calculated for a fixed waveguide length of $L = 2$ mm. The resulting

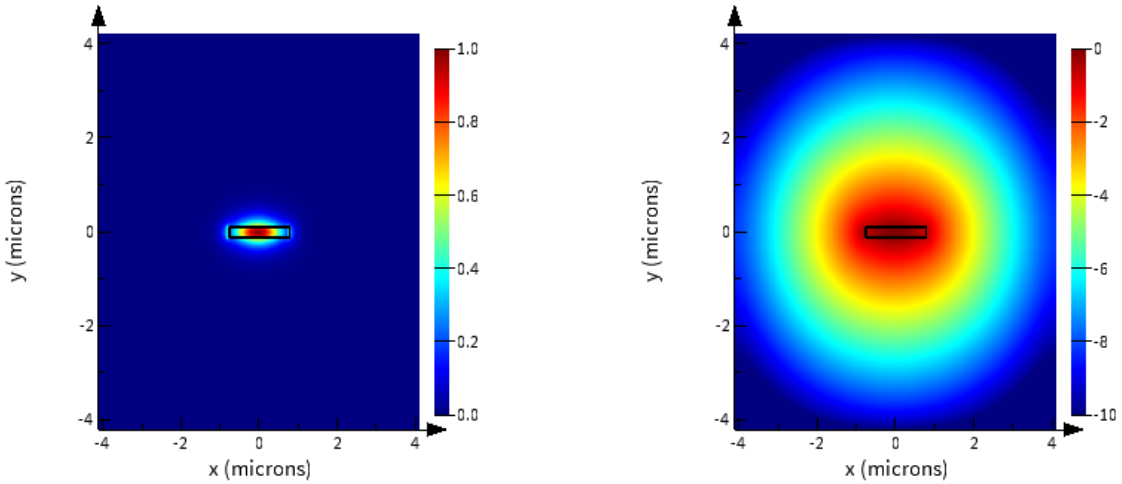

(a) $\lambda = 3.1$ μm linear scale.

(b) $\lambda = 3.1$ μm log scale.

Figure 4.6: Normalized electric field mode profiles on a linear and logarithmic scale for the TE_{00} mode at $\lambda = 3.1$ μm.

efficiencies, illustrated in Figs. 4.9a and 4.9b, achieve a conversion efficiency near 12.5%/W for conversion of 3.1 μm to 1.55 μm and 30.5%/W for conversion of 2.62 μm to 1.31 μm. The higher efficiency seen in the 2.62 μm to 1.31 μm wavelength conversion is due to the smaller effective mode area and slightly higher nonlinear spatial mode overlap. This aligns with the expectations of the smaller wavelength having stronger confinement to the waveguide. The comparison of the two waveguides further highlights the sensitivity of SHG

wavelength conversion	A_{eff} $(\mu m)^2$	ζ
3.1 μm $\rightarrow$ 1.55 μm	9.228	0.631876
2.62 μm $\rightarrow$ 1.31 μm	4.773	0.681604

Table 4.1: nonlinear spatial mode overlap and effective area for second harmonic generation from approximately 3.1 μm to 1.55 μm and 2.62 μm to 1.31 μm

.

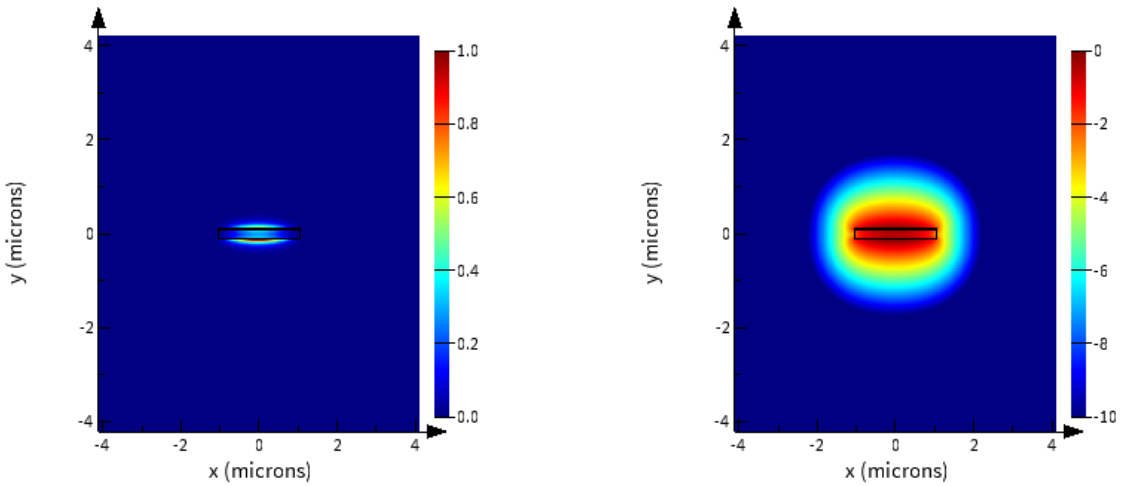

(a) $\lambda = 1.31$ μm linear scale.

(b) $\lambda = 1.31$ μm log scale.

Figure 4.7: Normalized electric field mode profiles on a linear and logarithmic scale for the TM_{00} mode at $\lambda = 1.31$ μm.

efficiency to waveguide geometry.

Although the losses due to scattering and absorption, and pump depletion are neglected in the analytical derivation of the SHG efficiency, the results provide valuable insight into the upper bound on the nonlinear performance of the InGaAsP-on-insulator platform. For practical devices, linear propagation loss, and absorption at the second-harmonic, as well as free-carrier effects at higher input powers are expected to reduce the conversion efficiency. Despite these factors, not taken into account here, the efficiencies compare well with the efficiencies for other materials with similar waveguide geometries and effective nonlinear coefficients, highlighting the promise of an InGaAsP-on-insulator material platform for compact, chip-scale wavelength conversion.

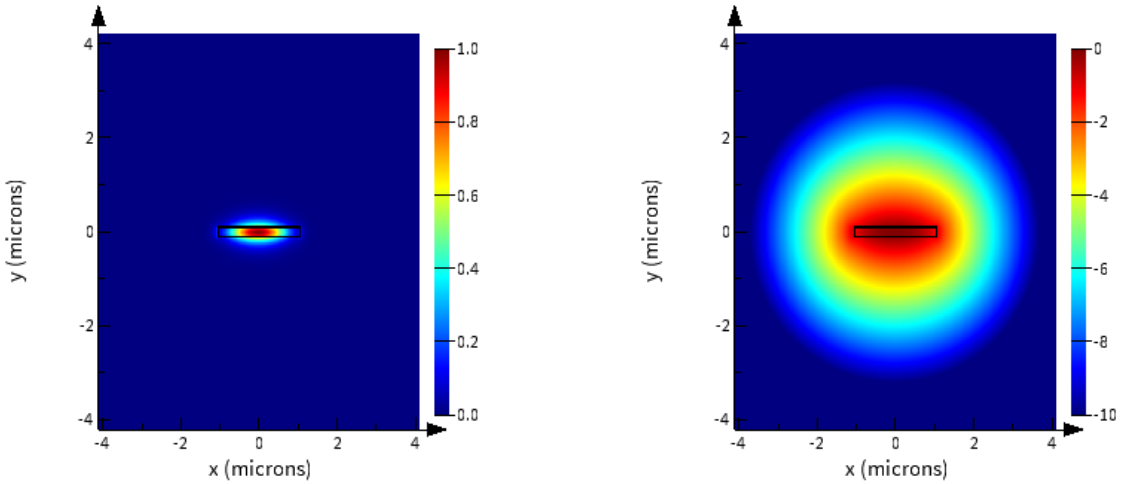

(a) $\lambda = 2.62$ μm linear scale.

(b) $\lambda = 2.62$ μm log scale.

Figure 4.8: Normalized electric field mode profiles on a linear and logarithmic scale for the TE_{00} mode at $\lambda = 2.62$ μm.

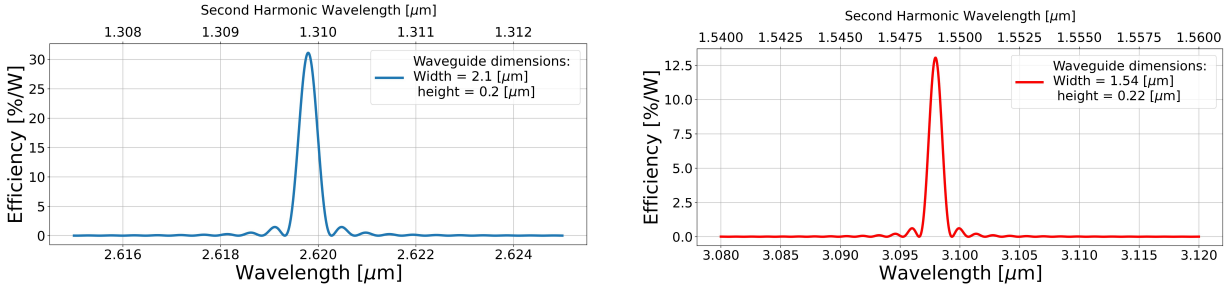

(a) SHG efficiency for approximately 2620 nm fundamental wavelength.

(b) SHG efficiency for approximately 3100 nm fundamental wavelength.

Figure 4.9: Comparison of simulated SHG efficiencies for 2 mm length InGaAsP-on-insulator waveguides at different fundamental wavelengths.

Further work in this area can extend the analysis by incorporating linear and nonlinear losses, and pump depletion, as well as phase-matching bandwidth and fabrication toler-

ance. In addition, studying other nonlinear effects such as four-wave mixing in InGaAsP waveguides could allow for optical frequency comb generation, which is especially useful for wavelength division multiplexing in data and communication applications. Investigating temporal soliton formation through the balance of group-velocity dispersion and self-phase modulation, as described in section 1.4, could expand the nonlinear capabilities supported by the platform. Finally, exploring other waveguide geometries with increased core height or engineered dispersion profiles could improve confinement of the TM mode in phase matching, reduce the effective mode area, and improve the nonlinear spatial mode overlap, thus increasing the efficiency of nonlinear processes further.

5

Conclusions

5.1 Conclusions

The growing need for integrated photonic technologies to support the increasing number of devices connected to the internet, for information processing, communications, and optical sensing, has highlighted the relevance of scalable integrated photonic platforms. Monolithic photonic platforms based on III-V semiconductors such as InGaAsP are well positioned to address this need, as they can integrate light generation, optical modulation, detection, and low-loss passive optical signal routing on a single chip. In Canada, the domestic capability for semiconductor and photonic research in this area remains limited due to a lack of standard design and fabrication pathways for III-V materials.

In this thesis, we present designs for high-index contrast InGaAsP-on-insulator passive photonic components operating in the telecommunication O and C bands. The main purpose of this work is to provide a streamlined design pathway for rapid fabrication of III-V photonic circuits by developing a passive component library that can be incorporated into a nonlinear optical process design kit. This addresses a major limitation in the current fabrication cycle of InP-based platforms, namely, the lack of a standardized component library that includes analytical models and simulated component performance.

In Chapter 1, the basics of optical properties of semiconductors, waveguide theory, numerical simulation methods, and the fundamentals of process design kit development are presented. This background provides the necessary context for the InGaAsP-on-insulator components presented in Chapters 2 through 4.

In Chapter 2, passive optical components developed in collaboration with Optiwave Systems Ltd. are presented. These include compact waveguide models, waveguide bends, linear tapers, waveguide splitters, and waveguide X-crossings. Minimum bend radii are determined based on propagation-loss criteria, yielding minimum values of 10 μm for the TE polarization at both $\lambda = 1.55$ and $\lambda = 1.31$ μm, and 30 and 20 μm for TM polarization at $\lambda = 1.55$ and $\lambda = 1.31$ μm, respectively.

Linear waveguide tapers are also presented in Chapter 2, for spot size conversion between a 500×220 nm single-mode waveguide and narrower or wider waveguides. Specifically, tapering to a 0.2×0.22 μm waveguide over a 40 μm length gives a simulated insertion loss of -0.01683 dB and -0.0036 dB for TE and TM polarizations, respectively. Similarly, tapering to a 1.0×0.22 μm waveguide over a 10 μm length gives a loss of -0.0003 dB and -0.0004 dB for TE and TM polarizations.

Next, in chapter 2, waveguide splitters including a Y-Branch, a 2×2 multi-mode interferometer (MMI), and a 2×2 directional coupler are discussed. These devices all achieve near-ideal 50/50 splitting ratios, with even power splitting achieved for the Y-Branch, wavelength-dependent response in the 2 x 2 directional coupler, and wavelength-dependent and near -3 dB splitting in the 2×2 MMI. Finally, in Chapter 2, a waveguide x-crossing based on a shape optimized cosine curves is presented, demonstrating minimal insertion losses of -0.17 dB and -0.32 dB for the TE and TM polarizations, respectively, at $\lambda = 1.55$ μm.

In Chapter 3, subwavelength photonic components, including a subwavelength grating

(SWG) waveguide and a subwavelength grating edge coupler, are presented, developed in collaboration with National Research Council Canada (NRC). The chapter introduces periodic waveguide theory, describing how the pitch and duty cycle of a periodic waveguide affect the effective refractive index of a Floquet-Bloch mode and can cause light to propagate as though it were a homogeneous waveguide in the subwavelength regime. In this section, the different regimes for propagation of light in periodic media are covered, including the radiative, Bragg reflection, and lossless regimes. The SWG waveguide is designed to propagate the TE-like Floquet Bloch mode in the lossless regime at $\lambda = 1.55$ μm and 1.31 μm, achieving simulated lossless propagation across a 20 μm SWG waveguide with a pitch of 0.2 and duty cycle of 0.6.

For the subwavelength edge coupler, simulated coupling from a tapered lensed fibre with an ideal beam diameter of 2.5 μm (MFD $1/e^2$) is presented for coupling the TE and TM modes to a single-mode waveguide. The compact edge coupler is 45 μm in length and achieves low simulated coupling loss for both TE and TM polarization of approximately -0.56 dB and -0.4 dB, respectively, with sub -1 dB loss maintained across the wavelength range of 1.5 - 1.6 μm, and lateral alignment tolerance of 0.7 μm for achieving coupling transmission less than -1 dB.

Finally, in Chapter 4, an InGaAsP-on-insulator second harmonic generation waveguide is designed and analyzed. The waveguide uses modal phase matching between the lowest-order fundamental TE_{00} and second-harmonic TM_{00} modes for the conversion from 3.1 μm to 1.55 μm and 2.62 μm to 1.31 μm. An analytical derivation of the second-harmonic generation efficiency is used, based on the relations of the linear electro-optic coefficients

derived from experimental measurements of binary III-V alloys, allowing estimation of the effective nonlinear coefficient, d_{eff}, associated with the d_{41} tensor element of the second-order susceptibility, $\chi^{(2)}$.

The resulting analytical SHG efficiencies for a proposed 2 mm long InGaAsP waveguide are approximately 12.5 %/W for the conversion from 3.1 μm to 1.55 μm, and approximately 30 %/W for the conversion from 2.62 μm to 1.31 μm. These efficiencies are produced from highly asymmetric waveguides to enhance the nonlinear spatial mode overlap, with waveguide dimensions of 1.54 $\times$ 0.22 μm and 2.1 $\times$ 0.2 μm for the respective wavelength pairs. These results highlight the potential of InGaAsP-on-insulator waveguides for infrared conversion to telecom wavelength conversion, applicable for integrated gas sensors, and wavelength conversion in nonlinear signal processing.

The components presented in this thesis present a benchmark for parameterizable III-V semiconductor photonic component libraries. Specifically, they can be adapted for multi-layer heterostructures and other III-V-on-insulator integrated photonics platforms. In further work, uncertainties in device performance can be obtained by incorporating fabrication tolerances and corner analysis. Throughout this thesis, the passive components developed are integrated into a component library for an InGaAsP-on-insulator PDK, creating a streamlined design-to-fabrication pathway for integrated photonic devices capable of nonlinear optical processes. Future improvements to the performance of the components may be realized using fabrication-aware optimization algorithms and experimental characterization of insertion loss, propagation loss, and nonlinear absorption to better refine associated compact models of components. The implications of the work presented here can enable

application-specific circuit design and are a foundation for a wide range of integrated photonic applications in optical, signal processing, and sensing technologies using monolithic semiconductor platforms.

APPENDICES

A

Appendix

A.1 System of units

quantity	unit	symbol	base dimension
length	meter	m	
mass	kilogram	kg	
time	second	s	
temperature	kelvin	K	
current	ampere	A	
frequency	hertz	Hz	
force	newton	N	kgm/s^2
pressure	pascal	pa	N/m^2
energy	joule	J	Nm
power	watt	W	Nm/s
charge	coulomb	C	As
electric potential	volt	V	Nm/As
conductance	siemens	S	A^2s/Nm
resistance	ohm	Ω	Nm/A^2s
capacitance	farad	F	A^2s^2/Nm
magnetic flux density	tesla	T	N/Am
inductance	henry	H	Nm/A^2

A.2 Physical constants

symbol	quantity	value	units
k_B	Boltzmann's constant	1.381×10^{-23}	J/K
		8.617×10^{-5}	eV/K
e	charge of the electron	-1.602×10^{-19}	C
m_e	mass of electron	9.109×10^{-31}	kg
m_p	mass of proton	1.673×10^{-27}	kg
ϵ_0	permeability of free space (magnetic constant)	$4\pi \times 10^{-7}$	H/m
μ_0	permittivity of free space (electric constant)	8.854×10^{-12}	F/m
h	Planck's constant	6.626×10^{-34}	Js
$\hbar$	Planck's reduced constant	1.055×10^{-34}	Js
n_0	refractive index in vacuum	1	-
c	speed of light in vacuum	2.998×10^8	m/s^2
R	universal gas constant	8.314	J/molK

References

1. *About* https://openai.com/about/ (2025).
2. *Company \ Anthropic* https://www.anthropic.com/company (2025).
3. Manyika, J. & Hsiao, S. *What is Gemini and how it works* Gemini. https://gemini.google/overview/ (2025).
4. Srivathsan, B. *et al. AI data center growth: Meeting the demand | McKinsey* AI power: Expanding data center capacity to meet growing demand. https://www.mckinsey.com/industries/technology-media-and-telecommunications/our-insights/ai-power-expanding-data-center-capacity-to-meet-growing-demand (2025).
5. Moore, S. K. *Nvidia Unveils Game-Changing Optical Network Switch - IEEE Spectrum* A Crucial Optical Technology Has Finally Arrived. https://spectrum.ieee.org/co-packaged-optics (2025).
6. *Integrated circuit (IC) | Types, Uses, & Function | Britannica* https://www.britannica.com/technology/integrated-circuit (2025).
7. Miller, S. E. Integrated optics: An introduction. *The Bell System Technical Journal* **48,** 2059–2069. ISSN: 0005-8580 (Sept. 1969).
8. Kawachi, M. Silica waveguides on silicon and their application to integrated-optic components. *Optical and Quantum Electronics* **22,** 391–416. ISSN: 0306-8919, 1572-817X (Sept. 1990).
9. Dragone, C., Edwards, C. & Kistler, R. Integrated optics N*N multiplexer on silicon. *IEEE Photonics Technology Letters* **3,** 896–899. ISSN: 1941-0174 (Oct. 1991).
10. Smit, M. & Van Dam, C. PHASAR-based WDM-devices: Principles, design and applications. *IEEE Journal of Selected Topics in Quantum Electronics* **2,** 236–250. ISSN: 1077260X (June 1996).
11. Takahashi, H. *Integrated Optics in Optical Communication Systems* in *Frontiers in Optics 2010/Laser Science XXVI* Frontiers in Optics (OSA, Rochester, New York, 2010), SWB3.
12. Coleman, J. J. The development of the semiconductor laser diode after the first demonstration in 1962. *Semiconductor Science and Technology* **27.** Publisher: IOP Publishing, 090207. ISSN: 0268-1242, 1361-6641 (Sept. 1, 2012).
13. Brinkman, W. F., Koch, T. L., Lang, D. V. & Wilt, D. P. The lasers behind the communications revolution. *Bell Labs Technical Journal* **5,** 150–167. ISSN: 1538-7305 (Jan. 2000).
14. Ishio, H., Minowa, J. & Nosu, K. Review and status of wavelength-division-multiplexing technology and its application. *Journal of Lightwave Technology* **2,** 448–463. ISSN: 0733-8724 (1984).

15. Agrawal, G. P. *Fiber-optic communication systems* 3. ed. ISBN: 9780471221142 9786610556304 (Wiley-Interscience, New York, NY, 2002).

16. *DWDM Channel Chart - ITU DWDM Channels Grid (nm, GHz)* EDGE Optical Solutions. `https://edgeoptic.com/kb_article/dwdm-channel-chart/` (2025).

17. Jørgensen, A. A. *et al.* Petabit-per-second data transmission using a chip-scale microcomb ring resonator source. *Nature Photonics* **16,** 798–802. ISSN: 1749-4885, 1749-4893 (Nov. 2022).

18. Yan, L. *et al.* All-Optical Signal Processing for UltraHigh Speed Optical Systems and Networks. *Journal of Lightwave Technology* **30,** 3760–3770. ISSN: 0733-8724, 1558-2213 (Dec. 2012).

19. Dokania, R. K. & Apsel, A. B. *Analysis of challenges for on-chip optical interconnects* in *Proceedings of the 19th ACM Great Lakes symposium on VLSI* GLSVLSI '09: Great Lakes Symposium on VLSI 2009 (ACM, Boston Area MA USA, May 10, 2009), 275–280. ISBN: 978-1-60558-522-2.

20. Daudlin, S. *et al.* Three-dimensional photonic integration for ultra-low-energy, high-bandwidth interchip data links. *Nature Photonics* **19,** 502–509. ISSN: 1749-4885, 1749-4893 (May 2025).

21. Ghiasi, A. 400GBase-LR8: A Proposal for 10 km Objective Using 50 Gb/s PAM4 Signaling.

22. Corzine, S. W. *et al.* Large-Scale InP Transmitter PICs for PM-DQPSK Fiber Transmission Systems. *IEEE Photonics Technology Letters* **22,** 1015–1017. ISSN: 1941-0174 (July 2010).

23. Evans, P. *et al. Multi-channel coherent PM-QPSK InP transmitter photonic integrated circuit (PIC) operating at 112 Gb/s per wavelength* in *2011 Optical Fiber Communication Conference and Exposition and the National Fiber Optic Engineers Conference* 2011 Optical Fiber Communication Conference and Exposition and the National Fiber Optic Engineers Conference (Mar. 2011), 1–3.

24. Debackere, P *et al.* Recent Trends in the Manufacturing of InP Photonic Integrated Circuits.

25. Dolgaleva, K., Ng, W. C., Qian, L. & Aitchison, J. S. Compact highly-nonlinear AlGaAs waveguides for efficient wavelength conversion. *Optics Express* **19.** TLDR: A broad-band self-phase modulation with a nonlinear phase shift up to 6, and four-wave mixing with a 20-nm tuning range and signal-to-idler conversion efficiency up to 10 dB are demonstrated., 12440. ISSN: 1094-4087 (June 20, 2011).

26. Bogaerts, W. & Chrostowski, L. Silicon Photonics Circuit Design: Methods, Tools and Challenges. *Laser & Photonics Reviews* **12.** _eprint: https://onlinelibrary.wiley.com/doi/pdf/10.1002/lpor.201700237, 1700237. ISSN: 1863-8899 (2018).

27. Zabelich, B., Lafforgue, C., Nitiss, E., Stroganov, A. & Brès, C.-S. Silicon nitride electric-field poled microresonator modulator. *APL Photonics* **9,** 016101. ISSN: 2378-0967 (Jan. 1, 2024).

28. Kotlyar, M. V., Iadanza, S. & O'Faolain, L. Lithium Niobate Fabry-Perot microcavity based on strip loaded waveguides. *Photonics and Nanostructures - Fundamentals and Applications* **43,** 100886. ISSN: 1569-4410 (Feb. 1, 2021).

29. Zhu, D. *et al.* Integrated photonics on thin-film lithium niobate. *Advances in Optics and Photonics* **13,** 242. ISSN: 1943-8206 (June 30, 2021).

30. Dai, D. & Bowers, J. E. Silicon-based on-chip multiplexing technologies and devices for Peta-bit optical interconnects. *Nanophotonics* **3.** Publisher: De Gruyter, 283–311. ISSN: 2192-8614 (Aug. 1, 2014).

31. Ciminelli, C., Dell'Olio, F., Conteduca, D. & Armenise, M. N. Silicon photonic biosensors. *IET Optoelectronics* **13,** 48–54. ISSN: 1751-8768, 1751-8776 (Apr. 2019).

32. Levy, J. S. *et al.* CMOS-compatible multiple-wavelength oscillator for on-chip optical interconnects. *Nature Photonics* **4,** 37–40. ISSN: 1749-4885, 1749-4893 (Jan. 2010).

33. Kemal, J. N. *et al.* Coherent WDM transmission using quantum-dash mode-locked laser diodes as multi-wavelength source and local oscillator. *Optics Express* **27,** 31164. ISSN: 1094-4087. arXiv: `1909.11174[physics]` (Oct. 28, 2019).

34. Wierzbowska, K., Bideux, L., Adamowicz, B. & Pauly, A. A novel III–V semiconductor material for NO2 detection and monitoring. *Sensors and Actuators A: Physical* **142,** 237–241. ISSN: 09244247 (Mar. 2008).

35. Sato, T., Mizohata, A. & Hashizume, T. Electrochemical Functionalization of InP Porous Nanostructures with a GOD Membrane for Amperometric Glucose Sensors. *Journal of The Electrochemical Society* **157,** H165. ISSN: 00134651 (2010).

36. Moreau, A. L. *et al.* Highly-sensitive and label-free indium phosphide biosensor for early phytopathogen diagnosis. *Biosensors and Bioelectronics* **36,** 62–68. ISSN: 09565663 (June 2012).

37. Vyas, K. *et al.* Group III-V semiconductors as promising nonlinear integrated photonic platforms. *Advances in Physics: X* **7,** 2097020. ISSN: 2374-6149 (Dec. 31, 2022).

38. Hall, R. N., Fenner, G. E., Kingsley, J. D., Soltys, T. J. & Carlson, R. O. Coherent Light Emission From GaAs Junctions. *Physical Review Letters* **9.** Publisher: American Physical Society (APS), 366–368. ISSN: 0031-9007 (Nov. 1, 1962).

39. Coldren, L. A. *et al.* High Performance InP-Based Photonic ICs—A Tutorial. *Journal of Lightwave Technology* **29,** 554–570. ISSN: 0733-8724, 1558-2213 (Feb. 2011).

40. Shih, M. H., Mock, A., Bagheri, M & Dapkus, P. D. Photonic crystal lasers in InGaAsP on a SiO2/Si substrate and its thermal impedance (2007).

41. Roelkens, G. *et al.* Integration of InP/InGaAsP photodetectors onto silicon-on-insulator waveguide circuits. *Optics Express* **13.** Publisher: Optica Publishing Group, 10102. ISSN: 1094-4087 (2005).

42. Roelkens, G. *et al.* Adhesive Bonding of InPInGaAsP Dies to Processed Silicon-On-Insulator Wafers using DVS-bis-Benzocyclobutene. *Journal of The Electrochemical Society* **153,** G1015. ISSN: 00134651 (2006).

43. *Geïntegreerde fotonica maakt de zorg toegankelijker en goedkoper* IO. `https://innovationorigins.com/nl/geintegreerde-fotonica-maakt-de-zorg-toegankelijker-en-goedkoper/` (2025).

44. Hakkel, K. D. *et al.* Integrated near-infrared spectral sensing. *Nature Communications* **13,** 103. ISSN: 2041-1723 (Jan. 10, 2022).

45. De Vries, C. Integrated Photonics for Automotive.

46. Smit, M., Williams, K. & van der Tol, J. Past, present, and future of InP-based photonic integration. *APL Photonics* **4,** 050901. ISSN: 2378-0967 (May 30, 2019).

47. Zheng, Y. *et al.* Integrated Gallium Nitride Nonlinear Photonics. *Laser & Photonics Reviews* **16,** 2100071. ISSN: 1863-8880, 1863-8899 (Jan. 2022).

48. Li, N. *et al.* Aluminium nitride integrated photonics: a review. *Nanophotonics* **10,** 2347–2387. ISSN: 2192-8614, 2192-8606 (July 8, 2021).

49. Wang, J. *et al.* InGaP/AlGaAs Near-UV and Visible Avalanche Photodiodes for Li-Fi Application. *IEEE Photonics Technology Letters* **36,** 293–296. ISSN: 1941-0174 (Mar. 2024).

50. Pearsall, T. Ga0.47In0.53As: A ternary semiconductor for photodetector applications. *IEEE Journal of Quantum Electronics* **16,** 709–720. ISSN: 1558-1713 (July 1980).

51. Fujii, T. *et al. InGaAsP/InP Buried Heterostruture on SiO2/Si Substrate Using Epitaxial Growth After Direct Bonding of Thin Active Layer* in *26th International Conference on Indium Phosphide and Related Materials (IPRM)* 2014 26th International Conference on Indium Phosphide and Related Materials (IPRM) (IEEE, Montpellier, May 2014), 1–2.

52. Hattasan, N. *et al. Heterogeneously integrated InGaAsSb detectors on SOI waveguide circuits for short-wave infrared applications* in *Advanced Photonics* Integrated Photonics Research, Silicon and Nanophotonics (OSA, Toronto, 2011), IWC5. ISBN: 978-1-55752-913-8.

53. Denton, A. R. & Ashcroft, N. W. Vegard's law. *Physical Review A* **43,** 3161–3164. ISSN: 1050-2947, 1094-1622 (Mar. 1, 1991).

54. Harris, J. S., O'sullivan, T, Sarmiento, T, Lee, M. M. & Vo, S. Emerging applications for vertical cavity surface emitting lasers. *Semiconductor Science and Technology* **26,** 014010. ISSN: 0268-1242, 1361-6641 (Jan. 1, 2011).

55. Adachi, S. *Properties of semiconductor alloys: group-IV, III-V and II-VI semiconductors* OCLC: ocn268957354. 400 pp. ISBN: 978-0-470-74369-0 (Wiley, Chichester, U.K, 2009).

56. Tsang, H. K. *et al.* Two-photon absorption and self-phase modulation in InGaAsP/InP multiquantum-well waveguides. *Journal of Applied Physics* **70,** 3992–3994. ISSN: 0021-8979, 1089-7550 (Oct. 1, 1991).

57. Saeidi, S. *et al.* Demonstration of optical nonlinearity in InGaAsP/InP passive waveguides. *Optical Materials* **84,** 524–530. ISSN: 09253467 (Oct. 2018).

58. Mercante, A. J. *et al.* Thin film lithium niobate electro-optic modulator with terahertz operating bandwidth. *Optics Express* **26,** 14810. ISSN: 1094-4087 (May 28, 2018).

59. Piprek, J., Abraham, P. & Bowers, J. Self-consistent analysis of high-temperature effects on strained-layer multiquantum-well InGaAsP-InP lasers. *IEEE Journal of Quantum Electronics* **36,** 366–374. ISSN: 1558-1713 (Mar. 2000).

60. Huang, Z. *et al. A 25Gbps low-voltage waveguide Si-Ge avalanche photodiode* in *2016 Conference on Lasers and Electro-Optics (CLEO)* 2016 Conference on Lasers and Electro-Optics (CLEO) (June 2016), 1–2.

61. Simon, S. H. *The Oxford solid state basics* 1st ed. OCLC: ocn853504907. 290 pp. ISBN: 978-0-19-968077-1 978-0-19-968076-4 (Oxford University Press, Oxford, 2013).

62. Mariotti, S. Hybrid and inorganic plumbo-halide perovskites for solar cells. Publisher: University of Liverpool Repository (2019).

63. Svelto, O. *Principles of Lasers* ISBN: 978-1-4419-1301-2 978-1-4419-1302-9 (Springer US, Boston, MA, 2010).

64. Yu, P. Y. & Cardona, M. *Fundamentals of Semiconductors: Physics and Materials Properties* ISSN: 1868-4513, 1868-4521. ISBN: 978-3-642-00709-5 978-3-642-00710-1 (Springer Berlin Heidelberg, Berlin, Heidelberg, 2010).

65. Kroemer, H. Heterostructure bipolar transistors and integrated circuits. *Proceedings of the IEEE* **70,** 13–25. ISSN: 1558-2256 (Jan. 1982).

66. Nathan, M. I. STIMULATED EMISSION OF RADIATION FROM GaAs p-n JUNCTIONS. **1.**

67. Holonyak, N. COHERENT (VISIBLE) LIGHT EMISSION FROM Ga(As1xPx) JUNCTIONS. *APPLIED PHYSICS LETTERS* **1** (1962).

68. Pollack, M. A., Nahory, R. E., DeWinter, J. C. & Ballman, A. A. Liquid phase epitaxial In1xGaxAsyP1y lattice matched to ⟨100⟩ InP over the complete wavelength range 0.921.65 m. *Applied Physics Letters* **33.** Publisher: AIP Publishing, 314–316. ISSN: 0003-6951, 1077-3118 (Aug. 15, 1978).

69. Cho, A. Y. Film Deposition by Molecular-Beam Techniques. *Journal of Vacuum Science and Technology* **8.** Publisher: American Vacuum Society, S31–S38. ISSN: 0022-5355 (Sept. 1, 1971).

70. Liu, H., Liu, X., Peng, L., Huang, Z. & Wu, Q. A comprehensive survey on optical modulation techniques for advanced photonics applications. *Optics and Lasers in Engineering* **186,** 108773. ISSN: 01438166 (Mar. 2025).

71. Zhong, H. *et al.* Ultra-low-power consumption silicon electro-optic switch based on photonic crystal nanobeam cavity. *npj Nanophotonics* **1,** 33. ISSN: 2948-216X (Aug. 30, 2024).

72. Yadav, A., Kumar, A. & Prakash, A. Design and analysis of optical switches using electro-optic effect based Mach-Zehnder interferometer structures. *Materials Today: Proceedings* **56,** 462–467. ISSN: 22147853 (2022).

73. Kim, Y., Han, J.-H., Ahn, D. & Kim, S. Heterogeneously-Integrated Optical Phase Shifters for Next-Generation Modulators and Switches on a Silicon Photonics Platform: A Review. *Micromachines* **12,** 625. ISSN: 2072-666X (May 28, 2021).

74. Li, Y., Sun, M., Miao, T. & Chen, J. Towards High-Performance Pockels Effect-Based Modulators: Review and Projections. *Micromachines* **15,** 865. ISSN: 2072-666X (June 30, 2024).

75. Boyd, R. W. *Nonlinear optics* Fourth edition. 609 pp. ISBN: 978-0-12-811002-7 (Elsevier, AP Academic Press, London, 2020).

76. Adachi, S. & Oe, K. Linear electro-optic effects in zincblende-type semiconductors: Key properties of InGaAsP relevant to device design. *Journal of Applied Physics* **56,** 74–80. ISSN: 0021-8979, 1089-7550 (July 1, 1984).

77. Bennett, B., Soref, R. & Del Alamo, J. Carrier-induced change in refractive index of InP, GaAs and InGaAsP. *IEEE Journal of Quantum Electronics* **26.** Publisher: Institute of Electrical and Electronics Engineers (IEEE), 113–122. ISSN: 0018-9197 (1990).

78. Henry, C. H., Logan, R. A. & Bertness, K. A. Spectral dependence of the change in refractive index due to carrier injection in GaAs lasers. *Journal of Applied Physics* **52,** 4457–4461. ISSN: 0021-8979, 1089-7550 (July 1, 1981).

79. Garmire, E. Semiconductor Components for Monolithic Applications.

80. Mahmudlu, H., May, S., Angulo, A., Sorel, M. & Kues, M. AlGaAs-on-insulator waveguide for highly efficient photon-pair generation via spontaneous four-wave mixing. *Optics Letters* **46.** Publisher: Optica Publishing Group, 1061–1064. ISSN: 1539-4794 (Mar. 1, 2021).

81. Ottaviano, L., Pu, M., Semenova, E. & Yvind, K. Low-loss high-confinement waveguides and microring resonators in AlGaAs-on-insulator. *Optics Letters* **41,** 3996. ISSN: 0146-9592, 1539-4794 (Sept. 1, 2016).

82. Saleh, B. E. A. & Teich, M. C. *FUNDAMENTALS OF PHOTONICS* 3rd (2019).

83. Okamoto, K. *Fundamentals of optical waveguides* 2nd ed. 561 pp. ISBN: 978-0-12-525096-2 (Elsevier, Amsterdam ; Boston, 2006).

84. *Integrated Optics* (ed Tamir, T.) (Springer Berlin Heidelberg, Berlin, Heidelberg, 1975). ISBN: 978-3-662-43210-5 978-3-662-43208-2.

85. *Canadian semiconductor industry* Last Modified: 2024-04-29 Publisher: Innovation, Science and Economic Development Canada. `https://ised-isde.canada.ca/site/digital-technologies-ict/en/canadian-semiconductor-industry` (2024).

86. Yee, K. Numerical solution of initial boundary value problems involving maxwell's equations in isotropic media. *IEEE Transactions on Antennas and Propagation* **14,** 302–307. ISSN: 1558-2221 (May 1966).

87. Vafaei, R. *What is Finite-Difference Time-Domain (FDTD)?* `https://www.ansys.com/blog/what-is-fdtd` (2025).

88. Sullivan, D. M. *Electromagnetic simulation using the FDTD method* Second edition. 182 pp. ISBN: 978-1-118-45939-3 (IEEE Press : John Wiley & Sons, Inc, Hoboken, New Jersey, 2013).

89. Courant, R., Friedrichs, K. & Lewy, H. On the Partial Difference Equations of Mathematical Physics. *IBM Journal of Research and Development* **11,** 215–234. ISSN: 0018-8646 (Mar. 1967).

90. *Finite Difference Time Domain (FDTD) solver introduction – Ansys Optics* `https://optics.ansys.com/hc/en-us/articles/360034914633-Finite-Difference-Time-Domain-FDTD-solver-introduction` (2025).

91. Silaeva, E., Saddier, L. & Colombier, J.-P. Drude-Lorentz Model for Optical Properties of Photoexcited Transition Metals under Electron-Phonon Nonequilibrium. *Applied Sciences* **11,** 9902. ISSN: 2076-3417 (Oct. 23, 2021).

92. Chu, S.-T. & Chaudhuri, S. A finite-difference time-domain method for the design and analysis of guided-wave optical structures. *Journal of Lightwave Technology* **7,** 2033–2038. ISSN: 1558-2213 (Dec. 1989).

93. Shea, J. D., Kosmas, P., Hagness, S. C. & Van Veen, B. D. Three-dimensional microwave imaging of realistic numerical breast phantoms via a multiple-frequency inverse scattering technique. *Medical Physics* **37,** 4210–4226. ISSN: 0094-2405, 2473-4209 (Aug. 2010).

94. Mor, G. K., Varghese, O. K., Paulose, M., Shankar, K. & Grimes, C. A. A review on highly ordered, vertically oriented TiO2 nanotube arrays: Fabrication, material properties, and solar energy applications. *Solar Energy Materials and Solar Cells* **90,** 2011–2075. ISSN: 09270248 (Sept. 2006).

95. Brasch, V. *et al.* Photonic chip–based optical frequency comb using soliton Cherenkov radiation. *Science* **351.** Publisher: American Association for the Advancement of Science, 357–360 (Jan. 22, 2016).

96. Wildi, T., Gaafar, M. A., Voumard, T., Ludwig, M. & Herr, T. Soliton Pulses in Photonic Crystal Fabry-Perot Microresonators. *Optica* **10,** 650. ISSN: 2334-2536. arXiv: `2206.10410[physics]` (June 20, 2023).

97. Wang, J., Sciarrino, F., Laing, A. & Thompson, M. G. Integrated photonic quantum technologies. *Nature Photonics* **14,** 273–284. ISSN: 1749-4885, 1749-4893 (May 2020).

98. Hayat, A., Nevet, A., Ginzburg, P. & Orenstein, M. Applications of two-photon processes in semiconductor photonic devices: invited review. *Semiconductor Science and Technology* **26,** 083001. ISSN: 0268-1242, 1361-6641 (Aug. 1, 2011).

99. Raimondi, M. T. *et al.* Two-Photon Laser Polymerization: From Fundamentals to Biomedical Application in Tissue Engineering and Regenerative Medicine. *Journal of Applied Biomaterials & Functional Materials* **10,** 56–66. ISSN: 2280-8000, 2280-8000 (Jan. 2012).

100. Baboux, F., Moody, G. & Ducci, S. Nonlinear integrated quantum photonics with AlGaAs. *Optica* **10.** Publisher: Optica Publishing Group, 917–931. ISSN: 2334-2536 (July 20, 2023).

101. Abolghasem, P., Han, J., Bijlani, B. J. & Helmy, A. S. Type-0 second order nonlinear interaction in monolithic waveguides of isotropic semiconductors. *Optics Express* **18,** 12681. ISSN: 1094-4087 (June 7, 2010).

102. Aghigh, A. *et al.* Second harmonic generation microscopy: a powerful tool for bio-imaging. *Biophysical Reviews* **15,** 43–70. ISSN: 1867-2450, 1867-2469 (Feb. 2023).

103. Sahin, E. *et al.* Difference-frequency generation in optically poled silicon nitride waveguides. *Nanophotonics* **10,** 1923–1930. ISSN: 2192-8614 (May 31, 2021).

104. Ulsig, E. Z. & Volet, N. *Second-order nonlinear effects in InGaAsP waveguides for efficient wavelength conversion to the mid-infrared* in *Nonlinear Frequency Generation and Conversion: Materials and Devices XX* Nonlinear Frequency Generation and Conversion: Materials and Devices XX (eds Schunemann, P. G. & Schepler, K. L.) (SPIE, Online Only, United States, Mar. 5, 2021), 28. ISBN: 978-1-5106-4175-4 978-1-5106-4176-1.

105. Ebrahim Jasim, K. in *Standards, Methods and Solutions of Metrology* (ed Cocco, L.) (IntechOpen, Oct. 2, 2019). ISBN: 978-1-78984-462-7 978-1-78984-463-4.

106. González-Andrade, D. *et al. Dispersion-engineered nanophotonic devices based on subwavelength metamaterial waveguides* in *2020 IEEE Photonics Conference (IPC)* 2020 IEEE Photonics Conference (IPC). ISSN: 2575-274X (Sept. 2020), 1–2.

107. Benedikovic, D. *et al.* Dispersion control of silicon nanophotonic waveguides using sub-wavelength grating metamaterials in near- and mid-IR wavelengths. *Optics Express* **25,** 19468. ISSN: 1094-4087 (Aug. 7, 2017).

108. Bock, P. J. *et al.* Subwavelength grating periodic structures in silicon-on-insulator: a new type of microphotonic waveguide. *Optics Express* **18,** 20251. ISSN: 1094-4087 (Sept. 13, 2010).

109. Jafari, Z. & Zarifkar, A. Dispersion flattened single etch-step waveguide based on subwavelength grating. *Optics Communications* **393.** Publisher: Elsevier BV, 219–223. ISSN: 0030-4018 (June 2017).

110. Halir, R. *et al.* Colorless directional coupler with dispersion engineered sub-wavelength structure. *Optics Express* **20,** 13470. ISSN: 1094-4087 (June 4, 2012).

111. Benedikovic, D. *et al.* Subwavelength index engineered surface grating coupler with sub-decibel efficiency for 220-nm silicon-on-insulator waveguides. *Optics Express* **23,** 22628. ISSN: 1094-4087 (Aug. 24, 2015).

112. Cheben, P. *et al.* Recent advances in metamaterial integrated photonics. *Advances in Optics and Photonics* **15,** 1033. ISSN: 1943-8206 (Dec. 31, 2023).

113. Wang, Y. *et al.* Design of broadband subwavelength grating couplers with low back reflection. *Optics Letters* **40,** 4647. ISSN: 0146-9592, 1539-4794 (Oct. 15, 2015).

114. Benedikovic, D. *et al.* Single-etch subwavelength engineered fiber-chip grating couplers for 13 µm datacom wavelength band. *Optics Express* **24,** 12893. ISSN: 1094-4087 (June 13, 2016).

115. Kamandar Dezfouli, M. *et al.* Perfectly vertical surface grating couplers using subwavelength engineering for increased feature sizes. *Optics Letters* **45,** 3701. ISSN: 0146-9592, 1539-4794 (July 1, 2020).

116. Cheben, P. *et al.* Refractive index engineering with subwavelength gratings for efficient microphotonic couplers and planar waveguide multiplexers. *Optics Letters* **35,** 2526. ISSN: 0146-9592, 1539-4794 (Aug. 1, 2010).

117. Cheben, P. *et al.* Broadband polarization independent nanophotonic coupler for silicon waveguides with ultra-high efficiency. *Optics Express* **23,** 22553. ISSN: 1094-4087 (Aug. 24, 2015).

118. Mu, X., Wu, S., Cheng, L. & Fu, H. Edge Couplers in Silicon Photonic Integrated Circuits: A Review. *Applied Sciences* **10,** 1538. ISSN: 2076-3417 (Feb. 24, 2020).

119. Dai, S., Wu, F., Gao, X. & Wu, P. *Design of high-performance silicon nitride edge coupler based on subwavelength grating* in *Twentieth National Conference on Laser Technology and Optoelectronics* Twentieth National Conference on Laser Technology and Optoelectronics (ed Liu, Q.) (SPIE, Shanghai, China, Aug. 26, 2025), 15. ISBN: 978-1-5106-9455-2 978-1-5106-9456-9.

120. Li, Y., Zhou, L., Wang, L., Li, K. & Zhang, F. Ultra-Compact Sub-Wavelength Grating Edge Coupler on a Thin-Film Lithium Niobate Platform. *IEEE Photonics Technology Letters* **37,** 889–892. ISSN: 1941-0174 (Aug. 2025).

121. Luan, E. *et al.* Label-free biosensing with a multi-box sub-wavelength phase-shifted Bragg grating waveguide. *Biomedical Optics Express* **10,** 4825–4838. ISSN: 2156-7085 (Aug. 26, 2019).

122. Cheng, W., Ye, S., Yuan, B., Marsh, J. H. & Hou, L. Subwavelength Grating Cascaded Microring Resonator Biochemical Sensors with Record-High Sensitivity. *ACS Photonics* **11,** 3343–3350. ISSN: 2330-4022, 2330-4022 (Aug. 21, 2024).

123. Zhang, Y. *et al.* Double-slot micro-ring resonators with trapezoidal subwavelength grating as ultra-sensitive biochemical sensors. *Optics Communications* **575,** 131256. ISSN: 00304018 (Jan. 2025).

124. Sahu, S., Mudgal, N., Agrawal, A. & Singh, G. Detection of Biomolecules and Glucose Concentration in Blood Using a Subwavelength Grating Optical Biosensor. *Journal of Sensors* **2023.** _eprint: https://onlinelibrary.wiley.com/doi/pdf/10.1155/2023/5533918, 5533918. ISSN: 1687-7268 (2023).

125. Luque-González, J. M. *et al.* A review of silicon subwavelength gratings: building break-through devices with anisotropic metamaterials. *Nanophotonics* **10,** 2765–2797. ISSN: 2192-8614 (Aug. 26, 2021).

126. Yablonovitch, E. Inhibited Spontaneous Emission in Solid-State Physics and Electronics. *Physical Review Letters* **58,** 2059–2062. ISSN: 0031-9007 (May 18, 1987).

127. John, S. Strong localization of photons in certain disordered dielectric superlattices. *Physical Review Letters* **58,** 2486–2489. ISSN: 0031-9007 (June 8, 1987).

128. *Photonic crystals: molding the flow of light* (ed Joannopoulos, J. D.) 2nd ed. OCLC: ocn180190957 (Princeton University Press, Princeton, 2008). 286 pp. ISBN: 978-0-691-12456-8.

129. Cheben, P., Halir, R., Schmid, J. H., Atwater, H. A. & Smith, D. R. Subwavelength integrated photonics. *Nature* **560,** 565–572. ISSN: 0028-0836, 1476-4687 (Aug. 2018).

130. *What is a Process Design Kit and How Does it Work? | Synopsys* `https://www.synopsys.com/glossary/what-is-a-process-design-kit.html` (2024).

131. Chrostowski, L. & Hochberg, M. E. *Silicon photonics design* ISBN: 978-1-107-08545-9 (Cambridge university press, Cambridge, 2015).

132. Shaker, L. M., Al-Amiery, A., Isahak, W. N. R. W. & Al-Azzawi, W. K. Integrated photonics: bridging the gap between optics and electronics for enhancing information processing. *Journal of Optics.* ISSN: 0974-6900 (July 27, 2023).

133. Melzer, J. E. & McLeod, E. 3D Nanophotonic device fabrication using discrete components. *Nanophotonics* **9.** Publisher: De Gruyter, 1373–1390. ISSN: 2192-8614 (June 1, 2020).

134. Canada, N. R. C. *Canadian Photonics Fabrication Centre* Last Modified: 2024-07-08. `https://nrc.canada.ca/en/research-development/nrc-facilities/canadian-photonics-fabrication-centre` (2024).

135. Brown, C. & Linden, G. *Chips and Change: How Crisis Reshapes the Semiconductor Industry* ISBN: 978-0-262-25865-4 (The MIT Press, Aug. 7, 2009).

136. Botsford, P. FABrIC Program Guide.

137. Mobini, E., Espinosa, D. H. G., Vyas, K. & Dolgaleva, K. AlGaAs Nonlinear Integrated Photonics. *Micromachines* **13,** 991. ISSN: 2072-666X (June 24, 2022).

138. Moghaddam, S. & O'Leary, S. K. A Sellmeier extended empirical model for the spectral dependence of the refractive index applied to the case of thin-film silicon and some of its more common alloys. *Journal of Materials Science: Materials in Electronics* **31,** 212–225. ISSN: 0957-4522, 1573-482X (Jan. 2020).

139. Heshmati, S., Taleb, H. & Rahmani, A. Complex Sellmeier equation for the refractive index of semiconductors in the opaque region. *Optik* **172,** 851–854. ISSN: 00304026 (Nov. 2018).

140. Ben Soltane, I., Dierick, F., Stout, B. & Bonod, N. Generalized Drude–Lorentz Model Complying with the Singularity Expansion Method. *Advanced Optical Materials* **12,** 2400093. ISSN: 2195-1071, 2195-1071 (Apr. 2024).

141. Guden, M & Piprek, J. Material parameters of quaternary III–V semiconductors for multilayer mirrors at 1.55 µm wavelength.

142. *Convergence testing process for FDTD simulations – Ansys Optics* `https://optics.ansys.com/hc/en-us/articles/360034915833-Convergence-testing-process-for-FDTD-simulations` (2025).

143. Liao, J. *et al.* Measurement of the effective refractive index of silicon-on-insulator waveguide using Mach–Zehnder interferometers. *Sensors and Actuators A: Physical* **379,** 115906. ISSN: 09244247 (Dec. 2024).

144. Zhang, E., Zhu, X. & Zhang, L. Effective and group refractive index extraction and cross-sectional dimension estimation for silicon-on-insulator rib waveguides. *Optics Express* **32,** 31375. ISSN: 1094-4087 (Aug. 26, 2024).

145. Dwivedi, S. *et al. Measurements of Effective Refractive Index of SOI Waveguides using Interferometers* in *Advanced Photonics 2015* Integrated Photonics Research, Silicon and Nanophotonics (OSA, Boston, Massachusetts, 2015), IM2A.6. ISBN: 978-1-55752-000-5.

146. Sharapova, P. R. *et al.* Toolbox for the design of $LiNbO_3$ -based passive and active integrated quantum circuits. *New Journal of Physics* **19,** 123009. ISSN: 1367-2630 (Dec. 5, 2017).

147. Liu, P., Wen, H., Ren, L., Shi, L. & Zhang, X. (2) nonlinear photonics in integrated microresonators. *Frontiers of Optoelectronics* **16,** 18. ISSN: 2095-2759 (July 17, 2023).

148. O'Brien, J., Patton, B., Sasaki, M. & Vučković, J. Focus on integrated quantum optics. *New Journal of Physics* **15,** 035016. ISSN: 1367-2630 (Mar. 12, 2013).

149. Tanzilli, S. *et al.* On the genesis and evolution of Integrated Quantum Optics. *Laser & Photonics Reviews* **6,** 115–143. ISSN: 1863-8880, 1863-8899 (Jan. 2, 2012).

150. Yang, Y. *et al.* Programmable quantum circuits in a large-scale photonic waveguide array. *npj Quantum Information* **11,** 19. ISSN: 2056-6387 (Feb. 3, 2025).

151. Butt, M. A., Imran Akca, B. & Mateos, X. Integrated Photonic Biosensors: Enabling Next-Generation Lab-on-a-Chip Platforms. *Nanomaterials* **15,** 731. ISSN: 2079-4991 (May 13, 2025).

152. Estevez, M., Alvarez, M. & Lechuga, L. Integrated optical devices for lab-on-a-chip biosensing applications. *Laser & Photonics Reviews* **6,** 463–487. ISSN: 1863-8880, 1863-8899 (July 16, 2012).

153. Yang, C.-J. *et al.* MediONN: an integrated photonic chip optical neural network for deep learning-based semantic segmentation in early detection of pancreatic cancer. *Biomedical Optics Express* **16,** 4312. ISSN: 2156-7085, 2156-7085 (Nov. 1, 2025).

154. Van Soest, G., Regar, E. & Van Der Steen, A. F. W. Photonics in cardiovascular medicine. *Nature Photonics* **9,** 626–629. ISSN: 1749-4885, 1749-4893 (Oct. 2015).

155. Sun, A. *et al.* Edge-guided inverse design of digital metamaterial-based mode multiplexers for high-capacity multi-dimensional optical interconnect. *Nature Communications* **16,** 2372. ISSN: 2041-1723 (Mar. 10, 2025).

156. González-Andrade, D. *et al.* Experimental demonstration of a broadband mode converter and multiplexer based on subwavelength grating waveguides. *Optics & Laser Technology* **129,** 106297. ISSN: 00303992 (Sept. 2020).

157. Li, H., Gao, W., Li, E. & Tang, C. Investigation of Ultrasmall 1\times N AWG for SOI-Based AWG Demodulation Integration Microsystem. *IEEE Photonics Journal* **7,** 1–7. ISSN: 1943-0655 (Dec. 2015).

158. Bogaerts, W. *et al.* Compact Wavelength-Selective Functions in Silicon-on-Insulator Photonic Wires. *IEEE Journal of Selected Topics in Quantum Electronics* **12,** 1394–1401. ISSN: 1558-4542 (Nov. 2006).

159. Vlasov, Y. A. & McNab, S. J. Losses in single-mode silicon-on-insulator strip waveguides and bends. *Optics Express* **12,** 1622. ISSN: 1094-4087 (2004).

160. Fujisawa, T., Makino, S., Sato, T. & Saitoh, K. Low-loss, compact, and fabrication-tolerant Si-wire 90° waveguide bend using clothoid and normal curves for large scale photonic integrated circuits. *Optics Express* **25,** 9150. ISSN: 1094-4087 (Apr. 17, 2017).

161. Zhou, Y. *et al.* A low loss silicon waveguide bend based on width and curvature variations. *Optics Communications* **565,** 130679. ISSN: 00304018 (Aug. 2024).

162. Bazargani, H. P., Flueckiger, J., Chrostowski, L. & Azaña, J. *Microring resonator design with improved quality factors using quarter Bezier curves* in *2015 Conference on Lasers and Electro-Optics (CLEO)* 2015 Conference on Lasers and Electro-Optics (CLEO). ISSN: 2160-8989 (May 2015), 1–2.

163. Phien, H. N. & Dejdumrong, N. Efficient algorithms for Bézier curves. *Computer Aided Geometric Design* **17,** 247–250. ISSN: 01678396 (Mar. 2000).

164. Dai, D. & Shi, Y. Deeply Etched \hboxSiO_2 Ridge Waveguide for Sharp Bends. *Journal of Lightwave Technology* **24,** 5019–5024. ISSN: 1558-2213 (Dec. 2006).

165. Jeong Hwan Song *et al. Advanced waveguide bends for photonic integrated circuits* in *45th European Conference on Optical Communication (ECOC 2019)* 45th European Conference on Optical Communication (ECOC 2019) (Institution of Engineering and Technology, Dublin, Ireland, 2019), 353 (3 pp.)–353 (3 pp.) ISBN: 978-1-83953-185-9.

166. Bahadori, M., Nikdast, M., Cheng, Q. & Bergman, K. Universal Design of Waveguide Bends in Silicon-on-Insulator Photonics Platform. *Journal of Lightwave Technology* **37,** 3044–3054. ISSN: 1558-2213 (July 2019).

167. Irfan, S., Kim, J.-Y. & Kurt, H. Ultra-compact and efficient photonic waveguide bends with different configurations designed by topology optimization. *Scientific Reports* **14,** 6453. ISSN: 2045-2322 (Mar. 18, 2024).

168. *NanoSOI Design Center | Applied Nanotools Inc.* `https://www.appliednt.com/nanosoi/sys/resources/specs/` (2025).

169. Dumon, P. *et al. Low-loss photonic wires and compact ring resonators in silicon-on-insulator* in. Photonics Europe (eds De La Rue, R. M., Viktorovitch, P., Sotomayor Torres, C. M. & Midrio, M.) (Strasbourg, France, Sept. 15, 2004), 360.

170. Lei, Z. *et al.* Efficient Broadband Wavelength Conversion in AlGaAsOI Nonlinear Nanowaveguides Using Low-Power Continuous-Wave Pump. *ACS Photonics* **12,** 1619–1627. ISSN: 2330-4022, 2330-4022 (Mar. 19, 2025).

171. Ikku, Y *et al.* Propagation-Loss Reduction in InGaAsP Photonic- wire Waveguides by InP and Al2O3 Passivation Layers.

172. Chen, T. *[Example Library] [WaveguideSizeConverter] Waveguide Size Converter Modeling in Tidy3D Flexcompute* `https://www.flexcompute.com/tidy3d/examples/notebooks/WaveguideSizeConverter/` (2025).

173. Dolores-Calzadilla, V & Millan-Mejia, A. Diffraction-suppressed adiabatic tapers for photonic circuits (2014).

174. Hettrick, S. J., Wang, J, Li, C, Wilkinson, J. S. & Shepherd, D. P. An Experimental Comparison of Linear and Parabolic Tapered Waveguide Lasers.

175. Milton, A. & Burns, W. Mode coupling in optical waveguide horns. *IEEE Journal of Quantum Electronics* **13,** 828–835. ISSN: 1558-1713 (Oct. 1977).

176. Smit, M. Tapers and Spot-Size Converters.

177. Hettrick, S., Wang, J., Li, C., Wilkinson, J. & Shepherd, D. An experimental comparison of linear and parabolic tapered waveguide lasers and a demonstration of broad-stripe diode pumping. *Journal of Lightwave Technology* **22,** 845–849. ISSN: 1558-2213 (Mar. 2004).

178. Reimer, C. *et al.* Generation of multiphoton entangled quantum states by means of integrated frequency combs. *Science* **351,** 1176–1180. ISSN: 0036-8075, 1095-9203 (Mar. 11, 2016).

179. Clementi, M. *et al.* Programmable frequency-bin quantum states in a nano-engineered silicon device. *Nature Communications* **14,** 176. ISSN: 2041-1723 (Jan. 12, 2023).

180. Poot, M., Schuck, C., Ma, X.-s., Guo, X. & Tang, H. X. Design and characterization of integrated components for SiN photonic quantum circuits. *Optics Express* **24,** 6843. ISSN: 1094-4087 (Apr. 4, 2016).

181. Liu, F. *et al.* Design of polarization-independent 1×2 optical power splitter based on silicon nitride slot waveguide structure. *Scientific Reports* **15,** 25288. ISSN: 2045-2322 (July 13, 2025).

182. Luo, Y., Yu, Y., Ye, M., Sun, C. & Zhang, X. Integrated dual-mode 3 dB power coupler based on tapered directional coupler. *Scientific Reports* **6,** 23516. ISSN: 2045-2322 (Mar. 22, 2016).

183. Geerthana, S. & Syedakbar, S. Design and optimization of Y-Junction and T-Junction splitters using photonic crystal. *Materials Today: Proceedings* **45,** 1722–1725. ISSN: 22147853 (2021).

184. Xu, Y., Tian, Z., Meng, X. & Chai, Z. Methods and applications of on-chip beam splitting: A review. *Frontiers in Physics* **10,** 985208. ISSN: 2296-424X (Sept. 6, 2022).

185. Ye, C. & Dai, D. Ultra-Compact Broadband 2 × 2 3 dB Power Splitter Using a Subwavelength-Grating-Assisted Asymmetric Directional Coupler. *Journal of Lightwave Technology* **38,** 2370–2375. ISSN: 1558-2213 (Apr. 2020).

186. Xu, Q. *et al.* Broadband Polarization-Independent Directional Coupler Using Asymmetric-Waveguides. *IEEE Photonics Journal* **11,** 1–6. ISSN: 1943-0655 (Dec. 2019).

187. Lu, Z. *et al.* Broadband silicon photonic directional coupler using asymmetric-waveguide based phase control. *Optics Express* **23,** 3795. ISSN: 1094-4087 (Feb. 9, 2015).

188. Wang, Y. *et al.* Compact Broadband Directional Couplers Using Subwavelength Gratings. *IEEE Photonics Journal* **8,** 1–8. ISSN: 1943-0655 (June 2016).

189. Chen, Y. & Xiao, J. Ultracompact and broadband silicon-based polarization-independent 1 × 2 power splitter using a shallowly etched multimode interference coupler. *Journal of the Optical Society of America B* **38,** 3064. ISSN: 0740-3224, 1520-8540 (Oct. 1, 2021).

190. Zhong, W. & Xiao, J. Ultracompact polarization-insensitive power splitter using subwavelength-grating-based MMI couplers on an SOI platform. *Applied Optics* **59,** 1991. ISSN: 1559-128X, 2155-3165 (Mar. 1, 2020).

191. Sun, C., Zhao, J., Wang, Z., Du, L. & Huang, W. Broadband and high uniformity Y junction optical beam splitter with multimode tapered branch. *Optik* **180,** 866–872. ISSN: 00304026 (Feb. 2019).

192. Zhang, Y. *et al. Ultra-broadband, Low Loss and Ultra-Compact 3dB Power Splitter Based On Y-Branch With Step Waveguide* in *2019 24th OptoElectronics and Communications Conference (OECC) and 2019 International Conference on Photonics in Switching and Computing (PSC)* 2019 24th OptoElectronics and Communications Conference (OECC) and 2019 International Conference on Photonics in Switching and Computing (PSC) (July 2019), 1–3.

193. Kim, H. & Shin, H. Tailorable and Broadband On-Chip Optical Power Splitter. *Applied Sciences* **9,** 4239. ISSN: 2076-3417 (Oct. 10, 2019).

194. Ponomarev, R. S., Zhuravlev, A. A. & Kichanov, A. V. *Relaxation processes of mobile charges in integrated optics Mach-Zehnder interferometer* in *2011 International Conference and Seminar on Micro/Nanotechnologies and Electron Devices Proceedings* 2011 International Conference and Seminar on Micro/Nanotechnologies and Electron Devices. ISSN: 1815-3712 (June 2011), 336–338.

195. *LIGO (Laser Interferometer Gravitational-wave Observatory)* Institution: McGraw-Hill Education.

196. Dwivedi, S., De Heyn, P., Absil, P., Van Campenhout, J. & Bogaerts, W. *Coarse wavelength division multiplexer on silicon-on-insulator for 100 GbE* in *2015 IEEE 12th International Conference on Group IV Photonics (GFP)* 2015 IEEE 12th International Conference on Group IV Photonics (GFP) (IEEE, Vancouver, BC, Canada, Aug. 2015), 9–10. ISBN: 978-1-4799-8255-4.

197. Chevalerias, R., Latron, Y. & Veret, C. Methods of Interferometry Applied to the Visualization of Flows in Wind Tunnels. *Journal of the Optical Society of America* **47,** 703. ISSN: 0030-3941 (Aug. 1, 1957).

198. *How to use the automatic nonuniform meshing? What steps per wavelength will be sufficient? — Tidy3D Electromagnetic Solver* `https://docs.flexcompute.com/projects/tidy3d/en/latest/faq/docs/faq/how-to-use-the-automatic-nonuniform-meshing-what-steps-per-wavelength-will-be-sufficient.html` (2025).

199. Ulrich, R. & Ankele, G. Self-imaging in homogeneous planar optical waveguides. *Applied Physics Letters* **27,** 337–339. ISSN: 0003-6951, 1077-3118 (Sept. 15, 1975).

200. Talbot, H. LXXVI. *Facts relating to optical science. No. IV. The London, Edinburgh, and Dublin Philosophical Magazine and Journal of Science* **9,** 401–407. ISSN: 1941-5966, 1941-5974 (Dec. 1836).

201. Cooney, K. & Peters, F. H. Analysis of multimode interferometers. *Optics Express* **24,** 22481. ISSN: 1094-4087 (Oct. 3, 2016).

202. Nelan, S. P. *et al.* Ultra-High Extinction Dual-Output Thin-Film Lithium Niobate Intensity Modulator. *IEEE Access* **10.** Conference Name: IEEE Access, 100300–100311. ISSN: 2169-3536 (2022).

203. Kamran, M. & Abedi, K. Conceptual design of multimode interference-based photonic crystal Mach-Zehnder interferometer (de)interleavers. *Optical and Quantum Electronics* **57,** 162. ISSN: 1572-817X (Feb. 14, 2025).

204. Zhang, Y. *et al.* An Integrated Few-Mode Power Splitter Based on Multimode Interference. *Journal of Lightwave Technology* **37,** 3000–3008. ISSN: 1558-2213 (July 2019).

205. Isayama, Y. H. & Hernández-Figueroa, H. E. High-Order Multimode Waveguide Interferometer for Optical Biosensing Applications. *Sensors (Basel, Switzerland)* **21,** 3254. ISSN: 1424-8220 (May 8, 2021).

206. Kumar, M., Kumar, A. & Dwivedi, R. Ultra high sensitive integrated optical waveguide refractive index sensor based on multimode interference. *Sensors and Actuators B: Chemical* **222,** 556–561. ISSN: 09254005 (Jan. 2016).

207. Kumar, G. & Chack, D. $1 \times N$ ($N = 2, 4$) dual-mode optical switch based on multimode interference coupler. *Optical and Quantum Electronics* **57,** 236. ISSN: 1572-817X (Apr. 1, 2025).

208. Soldano, L. & Pennings, E. Optical multi-mode interference devices based on self-imaging: principles and applications. *Journal of Lightwave Technology* **13,** 615–627. ISSN: 1558-2213 (Apr. 1995).

209. Ai, X., Zhang, Y., Hsu, W.-L., Veilleux, S. & Dagenais, M. Broadband 2x2 multimode-interference coupler on a silicon-nitride platform.

210. Liñares, J., Montero-Orille, C., Prieto-Blanco, X., Varela-Carballo, J. & Balado, D. Photonic quantum circuits with only synchronous directional couplers in ion-exchanged glass. *Journal of Physics: Photonics* **8,** 015003. ISSN: 2515-7647 (Mar. 1, 2026).

211. Venediktov, I. *et al.* Study of Directional Couplers for Optical Qubit Quantum Operations. *Technical Physics* **69,** 1450–1455. ISSN: 1063-7842, 1090-6525 (May 2024).

212. Yang, Y., Weiss, T., Arianfard, H., Youssry, A. & Peruzzo, A. A fixed phase tunable directional coupler based on coupling tuning. *Scientific Reports* **14,** 24291. ISSN: 2045-2322 (Oct. 16, 2024).

213. Gupta, R. K., Chandran, S. & Krishna, B. *Integrated silicon photonics directional couplers for WDM applications* in *2018 3rd International Conference on Microwave and Photonics (ICMAP)* 2018 3rd International Conference on Microwave and Photonics (ICMAP) (Feb. 2018), 1–2.

214. Yun, H. *et al.* Broadband 2 × 2 adiabatic 3 dB coupler using silicon-on-insulator sub-wavelength grating waveguides. *Optics Letters* **41,** 3041. ISSN: 0146-9592, 1539-4794 (July 1, 2016).

215. Halir, R. *et al.* Ultra-broadband nanophotonic beamsplitter using an anisotropic sub-wavelength metamaterial. *Laser & Photonics Reviews* **10.** _eprint: https://onlinelibrary.wiley.com/doi/pdf/10.1002/lpor.201600213, 1039–1046. ISSN: 1863-8899 (2016).

216. Zhang, X., Xie, W., Leong, C. & Gao, F. Compact inverse-designed tilted waveguide crossing. *Optics Letters* **50,** 1889. ISSN: 0146-9592, 1539-4794 (Mar. 15, 2025).

217. Wu, S., Mu, X., Cheng, L., Mao, S. & Fu, H. State-of-the-Art and Perspectives on Silicon Waveguide Crossings: A Review. *Micromachines* **11,** 326. ISSN: 2072-666X (Mar. 20, 2020).

218. Chandran, S. *et al.* Beam shaping for ultra-compact waveguide crossings on monolithic silicon photonics platform. *Optics Letters* **45,** 6230. ISSN: 0146-9592, 1539-4794 (Nov. 15, 2020).

219. Gilarlue, M., Nourinia, J., Ghobadi, C., Badri, S. H. & Rasooli Saghai, H. Multilayered Maxwell's fisheye lens as waveguide crossing. *Optics Communications* **435,** 385–393. ISSN: 00304018 (Mar. 2019).

220. Chang, W. & Zhang, M. Silicon-based multimode waveguide crossings. *Journal of Physics: Photonics* **2,** 022002. ISSN: 2515-7647 (Apr. 1, 2020).

221. Dong, Z. *et al.* Ultra-compact X-shaped waveguide crossings with flexible angles based on inverse design. *Optics Express* **29,** 19715. ISSN: 1094-4087 (June 21, 2021).

222. Schmid, J. H. *et al.* Refractive Index Engineering With Subwavelength Gratings in Silicon Microphotonic Waveguides. *IEEE Photonics Journal* **3.** Conference Name: IEEE Photonics Journal, 597–607. ISSN: 1943-0655 (June 2011).

223. *Bloch mode profile - Photonic crystal* Ansys Optics. `https://optics.ansys.com/hc/en-us/articles/360042038933-Bloch-mode-profile-Photonic-crystal` (2025).

224. *Understanding time apodization in frequency domain monitors – Ansys Optics* `https://optics.ansys.com/hc/en-us/articles/360034902473-Understanding-time-apodization-in-frequency-domain-monitors` (2025).

225. Almeida, V. R., Panepucci, R. R. & Lipson, M. Nanotaper for compact mode conversion. *Optics Letters* **28,** 1302. ISSN: 0146-9592, 1539-4794 (Aug. 1, 2003).

226. Galan, J. V. *et al. CMOS compatible silicon etched V-grooves integrated with a SOI fiber coupling technique for enhancing fiber-to-chip alignment* in *2009 6th IEEE International Conference on Group IV Photonics* 2009 6th IEEE International Conference on Group IV Photonics (GFP) (IEEE, San Francisco, CA, USA, Sept. 2009), 148–150. ISBN: 978-1-4244-4402-1.

227. Mangal, N., Snyder, B., Van Campenhout, J., Van Steenberge, G. & Missinne, J. Expanded-Beam Backside Coupling Interface for Alignment-Tolerant Packaging of Silicon Photonics. *IEEE Journal of Selected Topics in Quantum Electronics* **26,** 1–7. ISSN: 1558-4542 (Mar. 2020).

228. Liu, W., Zhang, J., Liu, L., Dai, D. & Shi, Y. High Efficiency Silicon Edge Coupler Based On Uniform Arrayed Waveguides With Un-Patterned Cladding. *IEEE Photonics Technology Letters* **32,** 1077–1080. ISSN: 1941-0174 (Sept. 2020).

229. *Overlap analysis - Modal Analysis Tab – Ansys Optics* `https://optics.ansys.com/hc/en-us/articles/360034917453-Overlap-analysis-Modal-Analysis-Tab` (2026).

230. Li, Y. *et al.* Polarization Insensitive Edge Coupler Assisted by Subwavelength Grating and Suspended Structure. *IEEE Photonics Technology Letters* **34,** 765–768. ISSN: 1941-0174 (July 2022).

231. Vijayakumar, S. *et al.* Phase-matched third-harmonic generation in silicon nitride waveguides. *Nanophotonics* **13,** 3385–3393. ISSN: 2192-8614 (Aug. 20, 2024).

232. Rao, A. & Fathpour, S. Second-Harmonic Generation in Integrated Photonics on Silicon. *physica status solidi (a)* **215.** _eprint: https://onlinelibrary.wiley.com/doi/pdf/10.1002/pssa.201700684, 1700684. ISSN: 1862-6319 (2018).

233. Luo, R., He, Y., Liang, H., Li, M. & Lin, Q. Highly tunable efficient second-harmonic generation in a lithium niobate nanophotonic waveguide. *Optica* **5.** Publisher: Optica Publishing Group, 1006–1011. ISSN: 2334-2536 (Aug. 20, 2018).

234. Stanton, E. J. *et al. Efficient second harmonic generation in nanophotonic GaAs-on-insulator waveguides* Feb. 14, 2020. arXiv: `1912.12346`.

235. Wang, C. *et al.* Broadband Second Harmonic Generation in a z-Cut Lithium Niobate on Insulator Waveguide Based on Type-I Modal Phase Matching. *Photonics* **10,** 80. ISSN: 2304-6732 (Jan. 10, 2023).

236. May, S., Kues, M., Clerici, M. & Sorel, M. Second-harmonic generation in AlGaAs-on-insulator waveguides. *Optics Letters* **44.** Publisher: Optica Publishing Group TLDR: Second-harmonic generation is demonstrated in AlGaAs-on-insulator waveguides at telecom wavelengths and this finding is important towards enabling new chip-scale devices for sensing, metrology, and quantum optics., 1339–1342. ISSN: 1539-4794 (Mar. 15, 2019).

237. Butt, M. A. & Piramidowicz, R. Integrated Photonic Sensors for the Detection of Toxic Gasses—A Review. *Chemosensors* **12.** Number: 7 Publisher: Multidisciplinary Digital Publishing Institute, 143. ISSN: 2227-9040 (July 2024).

238. Davis, M. E., Bernard, F., McGillen, M. R., Fleming, E. L. & Burkholder, J. B. UV and infrared absorption spectra, atmospheric lifetimes, and ozone depletion and global warming potentials for CCl2FCCl2F (CFC-112), CCl3CClF2 (CFC-112a), CCl3CF3 (CFC-113a), and CCl2FCF3 (CFC-114a).